ULTRASONIC ARRAY IMAGING FOR MULTI-LAYER MATERIALS IN NON-DESTRUCTIVE TESTING APPLICATIONS

By

Nasim Moallemi

SUBMITTED IN PARTIAL FULFILLMENT OF THE
REQUIREMENTS FOR THE DEGREE OF
DOCTOR OF PHILOSOPHY
AT
UNIVERSITY OF ONTARIO INSTITUTE OF TECHNOLOGY
OSHAWA, ONTARIO
DECEMBER 2014

To my family

who is a constant source of love and support

Table of Contents

List of Figures

Acronyms

CD	coherently distributed
DAS	delay and sum beamforming
DISPARE	dispersed signal parametric estimation
FMC	full matrix capture
ID	incoherently distributed
MAP	maximum a posteriori
MIMO	multiple input multiple output
MLE	maximum likelihood estimation
MMSE	minimum mean square error
MULOK	multi-layer omega-k
MUSIC	multiple signal classification
NDT	Non-destructive testing
PSM	phase shift migration
RMS	root-mean-squared
RMSE	root mean square error
ROI	region of interest
SAFT	synthetic aperture focusing technique
SNR	signal-to-noise-ratio
TFM	total focusing method
ULA	uniform linear array

Abstract

Ultrasonic imaging for a multi-layer medium is a common challenge in seismology, medical diagnosis, and non-destructive testing. One application for multi-layer imaging is ultrasonic immersion test where the material under test and transducer array are immersed in water. The main imaging challenge in immersion test (or in any multi-layer medium) is that since the sound wave propagates with different speeds in different layers, the homogeneity assumption is not valid. Thereby calculating the sound travel time for the backscattered received signal is complicated. In this dissertation, we propose a new approach to model the array received signals in order to image the material under test.

In the first approach, we propose a distributed reflector modeling approach to characterize the interface between water and the solid as well as any crack inside the solid test sample. This approach relies on incoherently distributed reflector modeling. A distributed reflector can be modeled as infinitely many point sources located close to each other. We use distributed reflector modeling in order to estimate the shape of the reflectors. To do so, we present our data model in a two-dimensional coordinate system, and then develop a covariance fitting based approach to parametric estimation of the shape of the interface between the two media and that of a crack inside the test material. Numerical computer simulations show the accuracy of the proposed approach. However the proposed approach is a parametric localization method which needs the repetition of the ultrasonic test.

In the second approach we present a data model to use for image reconstruction of a multi-layer medium without need to repeat the ultrasonic experiment. In this

approach, we also use the spatially distributed source to model the interfaces between the layers of a multi-layer medium. Then, based on the Huygens principle, we develop a new array spatial signature for all the points inside a multi-layer medium. This new array spatial signature can be used in existing imaging techniques including the conventional beamforming technique, the MUSIC method, and the Capon algorithm in order to image a multi-layer medium. These aforementioned three algorithms are traditionally applied for a homogeneous medium where the sound velocity is constant in the material under test. Numerical simulations as well as experimental data show that the distributed reflector modeling outperforms other approaches such as rooted mean square velocity.

In the third approach, to reduce the execution time for the imaging process, we develop a Fourier-based imaging technique to estimate the scattering coefficient of the points inside the second layer of a two-layer medium in order to obtain an image of the region of interest. First, we use an approximation of the proposed data model for the array backscattered signals due to the scattering of the point scatterers inside the second layer of the material under test. Seeking the similarity with the definition of Fourier transform, we propose a Fourier-based imaging algorithm, for imaging the second layer of the material under test. In this proposed algorithm, the execution time is considerably reduced compared to the three aforementioned imaging algorithms. This proposed algorithm can be used in an online imaging process.

Acknowledgements

I would like to express my gratitude to my supervisor Dr. Shahram Shahbazpanahi for all his support, help, and motivation. He helped me in establishing the research skills and I hope I will carry his inspiration in my future studies and throughout my career. I would also like to express my deepest thank to the members of my examining committee: Dr. Ali Grami and Dr. Min Dong for their encouragement and insightful comments and advice for the improvement of this dissertation. I also would like to thank all my colleagues and friends whose reviews, insights and company will always be remembered.

A special thanks to my family. Words cannot express how grateful I am to my mother-in-law for her love and support; to my mother and father who supported me every step of my life with patience and love; to my sisters-in-law and brothers-in-law for their encouragement and advice; and to my sisters and brothers who always have been by my side whenever I needed them. At the end, I would like to express my appreciation to my love Bijan, who was always my support in the moments when there was no one to answer my queries. Without them this work would never have come into existence.

Oshawa, Ontario — Nasim Moallemi
December, 2014

Chapter 1

Introduction

1.1 Overview

Non-destructive testing (NDT) is a quality control method which includes a wide range of non-invasive techniques to inspect the integrity of materials, components, and structures without causing any damage to them. Examination of industrial materials assures safety and reliability, helps the troubleshooting process, and prevents early replacement of components or shutting down systems. Extending the useful lifetime of components in industry and preventing unnecessary and expensive exchanges increase the revenue by saving time and reducing the maintenance costs. By extending the useful lifetime of the materials, NDT also helps protecting the environment which is one of the main challenges of the world in the 21th century. Therefore, non-destructive tests are used in a variety of industrial applications such as power plants, automotive, pipelines, airplanes, and constructions.

Non-destructive testing methods include a wide range of techniques such as electromagnetic tests, laser tests, radiographic tests, and ultrasonic tests. In this dissertation, we focus on ultrasonic testing. Ultrasonic imaging is a common method to inspect materials for flaw detection and thickness measurement in both industry and

in medical diagnosis. Ultrasonic imaging uses high-frequency sound waves to detect any discontinuity inside the material under test. Ultrasonic inspection is attractive for NDT because it only needs to access one side of materials for conducting the ultrasonic test. Moreover, it is highly accurate in localizing the scatterers and estimating the size and the shape of the flaws inside metallic materials.

Sensor array processing and multiple input multiple output (MIMO) utilizes multiple sensors or antennas to facilitate the localization process by providing spatial diversity. MIMO signal processing has widely been applied in the area of wireless communication to increase the reliability and data rate, compared to the traditional single transmitter receiver techniques [1, 2]. MIMO has also been recently used in radar imaging, materializing the concept of MIMO radar. In MIMO radar, multiple antennas are used to transmit high-frequency electromagnetic waves towards targets and to receive the signal backscattered from the targets. These received signals are recorded and processed to obtain an image of the targets. Moreover, MIMO has applications in sonar imaging to localize ships and submarines or to extract the information regarding the sea bed. More recently, multiple ultrasonic sensors are used to obtain more accurate image of the material under test for NDT applications. There are a significant volume of literature on the array signal processing techniques for applications in radar, sonar, biomedical engineering, and wireless communication. These techniques include robust adaptive beamforming [3,4], distributed source modeling [5–7], MIMO signal processing for imaging [8], vector sensor processing [9–12], wide-band array processing [13–15], and cross-polarization imaging [16]. Compared to the other applications, array signal processing in NDT has gained less attention in the literature. There are certain array processing techniques and modeling which

appear to be a better fit in NDT applications. One of these techniques is distributed source modeling which is investigated in this dissertation.

1.2 Motivation

Since 1980s, ultrasonic phased arrays have been drastically used for non-destructive testing in industry and medical diagnosis [17–24]. The diversity provided by different positions of transmitters and receivers in an array of transducers facilitates localizing scatterers inside the material under test. Traditionally, ultrasonic arrays are used to emulate a monolithic transducer with a larg aperture. Independent transmission circuits for each transducer of the array enable different transducers to fire with different time delays. Therefore, the probing sound wave can be focused on each point in the region of interest (ROI) to generate a real time image [17]. However, in many NDT applications, the targets are static and we can take advantage of off-line post-processing methods. To do so, the data corresponding to all combinations of transmitter and receiver transducers are collected in a matrix and are used in off-line post-processing [19]. There are several efficient post-processing algorithms, which are widely used in NDT, in case of ultrasonic contact test for a homogenous medium. In a homogenous medium, the sound wave propagates with a constant speed inside the entire medium [18, 20]. However, these algorithms can not be used for non-homogenous materials since the sound speed is not constant during the entire propagation path. One example of non-homogenous materials is a multi-layer medium consisting of parallel layers with different sound speeds. One application for multi-layer imaging is ultrasonic immersion test where the material under test and the transducer array are

immersed in water. Immersion test provides a consistent coupling between the material under test and the transducer array, while moving the transducers. Therefore, the immersion test is often used in NDT, when the surface of the material under test is rough and providing a consistent and uniform couplant between the transducer array and the test sample in a contact test is not possible. However, the main challenge in immersion test (or any multi-layer medium) is that the assumption of constant speed is not valid, thereby calculating the sound travel time for the backscattered received signal is complicated. This motivates us to develop a new model for multi-layer imaging.

1.3 Objective and Methodology

In traditional array signal modeling, it is usually assumed that sources (or reflectors) are point sources (or point reflectors) located at the far field of the sensors. However, in applications, such as radar, sonar, wireless communications, and non-destructive testing, reflectors are distributed in space. One example of these distributed reflectors in NDT is the interfaces between layers in a multi-layer medium. Assuming these interfaces as point reflectors could cause a major error in localizing a target inside the material under test. Therefore, the distributed reflector modeling is more appropriate than point reflector modeling for multi-layer imaging. In order to provide superior imaging capabilities, we aim to investigate and properly develop this distributed source modeling for multi-layer imaging which immersion ultrasonic test is one example of it. Using this model, we aim to obtain a higher quality image of a multi-layer medium.

A distributed reflector can be modeled as multiple point reflectors located close to

each other. Distributed reflectors can be modeled either as incoherently distributed (ID) reflectors or as coherently distributed (CD) reflectors. The backscattered signals arriving from different points of a CD reflector are fully correlated, while backscattered signals arriving from different points of an ID reflector are uncorrelated. For example, radio waves reflected by the layers of troposphere or a signal reflected from different points of a rough surface are uncorrelated [5]. In most aforementioned literature on distributed source localization, the main goal is to estimate the parameters of reflector spatial distribution including central direction of arrival and angular spread of the reflected signal. However, the spatial distribution of these signals may not provide much information about the shape of the reflector. However in this dissertation, we use distributed reflector modeling in order to estimate the shape of the reflectors.

In the first approach, we focus on the immersion ultrasonic test when the material under test has a rough surface and rough crack shape. Then, we model the upper surface of the test material and any crack inside the test sample as ID reflectors. We then take advantage of repeating the ultrasonic test and aim to propose a covariance fitting based approach to localize and characterize a crack inside the test sample. This is a parametric localization approach, and based on a known shape for the reflector, estimates the parameters of the shape of the reflector. However, applying the covariance fitting approach needs the repetition of the ultrasonic test.

In the second approach, we aim to image a multi-layer medium based on the distributed source model for the interfaces between the layers without need to repeat the ultrasonic test. There are some imaging algorithms including phase shift migration (PSM) and multi-layer omega-k (MULOK) which have been applied for imaging multi-layer materials in NDT; however, other frequency domain approaches, such as

the conventional beamforming technique, the multiple signal classification (MUSIC) method, and the Capon algorithm, are not applicable when the sound velocity is not constant in the material under test [25, 26]. Moreover, the PSM and MULOK algorithms have been proposed for synthetic aperture focusing scenarios and to the best of our knowledge, they have not been applied for the case when an array of transducers is used. Then, we aim to propose a model that is applicable for frequency-domain imaging algorithms in a multi-layer medium when a transducer array is utilized. To do so, we model the interfaces between layers of a multi-layer medium as spatially distributed sources consisting of infinite number of point sources. Then, we use this model to develop a new array spatial signature for all the points inside a multi-layer medium. This new array spatial signature can be used in existing imaging techniques including the conventional beamforming technique, the MUSIC method, and the Capon algorithm in order to image multi-layer materials. These algorithms traditionally are applied for a homogeneous medium where the sound velocity is constant in the medium [27–30]. To the best of our knowledge, these algorithms have not been used for imaging a multi-layer medium.

In the third approach, we aim to reduce the execution time of the imaging process. To do so, first, we use an approximation of the proposed data model for the array backscattered signals due to the scattering of the point scatterers inside the second layer of the material under test. Then, we propose a Fourier-based imaging algorithm, for imaging the second layer of the material under test. Note that the approach of [20] is proposed only for imaging a homogeneous materials and our proposed algorithm is not a simple extension of the wavenumber algorithm of [20]. In this proposed algorithm, the execution time is considerably reduced compared to the

three aforementioned imaging algorithms and it can be used in an online imaging process.

1.4 Summary of Contributions

The contribution of our work can be summarized as follows

- We developed a data model for reflector localization for a scenario where the reflectors are located in an environment which is different from the environment where the array is located. To the best of our knowledge, this is the first attempt to consider such a scenario and to model the array signal in this case.
- We estimate the *shape* of the reflectors as apposed to estimate their center angle and angular spread which is the trend in the available literature. To do so, we apply a covariance fitting method to the scenario explained above.
- We develop a new array spatial signature, based on the distributed source modeling, for all the points inside a multi-layer medium. This new array spatial signature can be used in existing imaging techniques, which are traditionally applied for a homogeneous medium, in order to image multi-layer materials.
- We develop a new Fourier-based imaging algorithm to estimate the scattering coefficient of all the points in the ROI in order to obtain an image of a multi-layer medium. This algorithm can be used in an online imaging process.

1.5 List of Publications

Below is the list of publications corresponding to this dissertation:

- N. Moallemi and S. ShahbazPanahi, "New Algorithm for second layer ultrasonic array imaging," to be submitted to *IEEE Trans. Signal Process.*

- N. Moallemi and S. ShahbazPanahi, "A New Model for Array Spatial Signature with Applications in Non-destructive Ultrasonic Multi-layer Array Imaging," submitted to *IEEE Trans. Signal Process.*, received major revision recommendation, revised and resubmitted on Sep. 2014.

- N. Moallemi and S. ShahbazPanahi, "A distributed reflector localization approach to ultrasonic array imaging for non-destructive testing application," *IEEE Trans. Signal Process.*, vol. 62, pp. 3863-3873, Aug. 2014.

- N. Moallemi, S. ShahbazPanahi, "Immersion Ultrasonic Array Imaging Using a New Array Spatial Signature in Different Imaging Algorithms" *in proceedings of IEEE Asilomar Conference on Signals, Systems, and Computers,* Nov. 2014.

- N. Moallemi, S. ShahbazPanahi, "Multi-layer Ultrasonic Imaging for Non-destructive Testing Applications" *in proceedings of International Ultrasonics Symposium, Chicago, Illinois, USA,* pp. 53-56, Sep. 2014.

- N. Moallemi, S. ShahbazPanahi, "Ultrasonic Array Imaging for Immersion Non-Destructive Testing," *in proceedings of Sensor Array and Multichannel Signal Processing Workshop, Coruna, Spain,* pp. 185-188, Jun. 2014.

1.6 Outline of Dissertation

In this dissertation we focus on imaging a multi-layer medium for NDT applications using distributed source modeling. Based on this model, we develop a new array

spatial signature to image a multi-layer medium. The remainder of this dissertation is organized as follows: In Chapter 2, we present a review on recent studies on imaging techniques for ultrasonic NDT. We also provide a literature review on distributed source localization methods. In Chapter 3, we provide the result of covariance fitting approach for localizing a crack under the weld for an immersion ultrasonic test. In Chapter 4, we develop an array spatial signature for a multi-layer medium based on Huygens principle. To show the accuracy of this model, we conduct an immersion ultrasonic test and image the material under test (which is the second layer in a two-layer medim) with different existing imaging techniques using our new array spatial signature. In Chapter 5, we have discussed the details of our proposed Fourier-based imaging algorithm which can be used in an online imaging process. The conclusions and future works are provided in Chapter 6.

Chapter 2

Background and Literature Review

In this chapter, the recent studies in related area to this dissertation are discussed and their advantages and disadvantages are reviewed. In section 2.1, a breif introduction on ultrasonic test in NDT application is explained. In section 2.2, we review the recent literature on ultrasonic NDT methods and challenges. In section , a brief survey on the array processing techniques for localizing distributed sources is presented. Although distributed source model in practise is more appropriate than the point source model, distributed source localization is a new research area and the papers in this field is mostly have been published in this decade.

2.1 Ultrasonic Test Overview

The objective of an ultrasonic test including industrial inspection and medical diagnosis is to obtain an image of the material under test in order to localize or characterize any discontinuity inside the material under test. To conduct an ultrasonic test, an ultrasonic transducer is used to convert an electric pulse into a high-frequency acoustic wave. Propagating wave in solid material scatters by any discontinuity inside the

material including any flaws, defects and side walls. Another transducer or the same one is used to convert the backscattered sound wave into electrical signal. Common ultrasonic testing configurations are depicted in Fig. 2.1. In pulse-echo configuration, one single transducer is used to transmit and receive the ultrasound wave while in pitch-catch configuration, different transducer is used for receiving backscattered signal. Therefore, the pitch catch configuration is suitable for localizing angled cracks. Through-transmission configuration needs two sides of the material under test and detects cracks when it does not receive any signal.

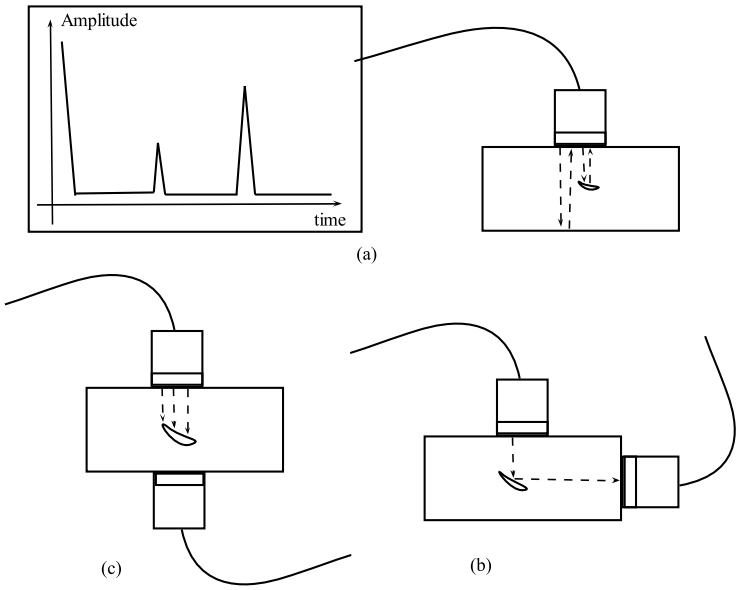

Figure 2.1: Ultrasonic test configuration. (a) Pulse-echo. (b) Pitch-catch (c) Through-transmission.

The received signal is sampled and quantized and stored in a digital computer. This received signal contains information about the location, shape and the strength

of the scatterers. Digital signal processing has a key role in extracting information from the received signal such as range, direction of arrival, and speed of propagation.

2.2 Ultrasonic Array Imaging

Array processing is a branch of signal processing which deploys an array of sensors to detect the presence and/or to estimate the parameters of signals propagating in a medium. Array processing has variety of applications in radar, sonar, wireless communication, seismology, and biomedical diagnosis. One of the the applications of advanced array processing is NDT, where an array of ultrasonic transducers is used for flaw detection and imaging inside solid structures. Larger coverage area without need for reconfiguration, improving sensitivity, and reducing the time for conducting the test, are some of the advantages of using transducer array compared to a conventional single-element transducer. The ultrasonic arrays in NDT have different array geometries which are designed for different industrial applications. In this dissertation, we focus on uniform linear array; however, the proposed model can be extended to other array geometries. The maximum array size, which is currently used in NDT, is limited to 256 elements based on today's computer computing power and electronic size. Traditionally, ultrasonic arrays are used to emulate a monolithic transducer with a larger aperture. Independent transmission circuits for each transducer of the array enable different transducers to fire with different time delays. Therefore, the probing sound wave can be focused on each point in the ROI to generate a real time image [17]. Some popular algorithms for real time imaging include plane B-scan, focused B-scan and sector B-scan [18]. In each of these methods, a group of the transducers is used

to fire simultaneously in order to generate the desired focused wave.

In many NDT applications, the targets are static and we can take advantage of off-line post-processing methods. To do so, the data corresponding to all combinations of transmitter and receiver transducers are collected in a matrix (see Fig. 2.2) which is used in off-line post-processing [19]. This method of storing data is known as full matrix capture (FMC).

When the material under ultrasonic test is homogenous, the sound wave propagates with a constant speed in the medium. However, in some applications, the material under test is non-homogenous i.e., the sound speed is not constant during the entire medium. This non-uniform motion of sound in the material under test is a main challenge in imaging a non-homogenous medium.

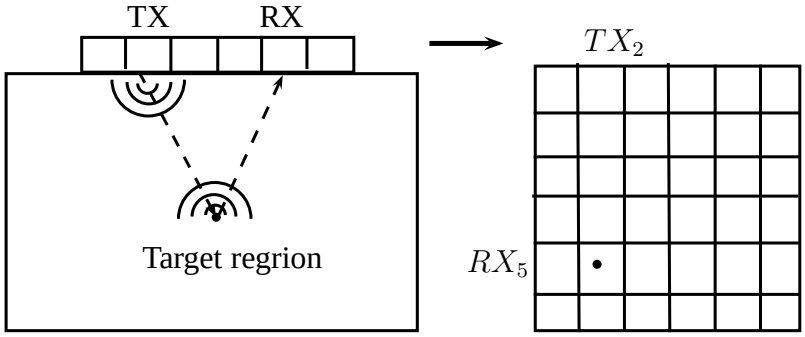

Figure 2.2: Full matrix capture.

2.2.1 Ultrasonic Imaging for a Homogenous Medium

The data, which is collected by the FMC method, can be used to emulate the focused wave on each point in the ROI by applying delay and sum beamforming (DAS). In [18], a time-domain post-processing algorithm, known as total focusing method (TFM), is

proposed for a uniform linear array based on delay and sum beamforming. To image the ROI, we need to assign a relative intensity to each pixel point in the ROI. For this purpose, the ROI is covered with a sufficiently fine grid. The relative intensity of each point in the ROI, based on TFM algorithm can be written as summation of all delayed received signals using the sound travel times corresponding to the backscattered sound wave from that point to each transducer. the summation is carried over all combinations of transmitter-receiver pair in the array of transducers. Therefore, TFM uses maximum of the available information. The TFM method can be effectively implemented. The only limitation is execution time. In [19], a vectorized version of TFM has been proposed. This algorithm is more accurate to obtain the information about the orientation of angled cracks compared to TFM.

In [20], a frequency-domain algorithm is proposed as a wavenumber algorithm. Wavenumber algorithm is based on DAS beamforming in frequency domain, however, this algorithm uses Stolt mapping method to reduce the computational complexity of the implementation. In [21], two methods have been proposed. These methods performs compensation in both spatial and temporal space based on minimum mean square error(MMSE) criterion and maximum a posteriori(MAP) estimation approach. The performance of the linear MMSE and non-linear MAP estimators shows higher temporal and lateral resolution compared to DAS beamforming method. They effectively suppress the effect of side lobes and grating lobes. In all these algorithms, the sound speed is assumed to be constant in the material under test. In the next subsection, a brief review on ultrasonic imaging algorithms for multi-layer medium is provided.

2.2.2 Ultrasonic Imaging for a Multi-layer Medium

There are several efficient post-processing algorithms, which are widely used in NDT, in case of ultrasonic contact test for a homogenous medium [18, 20]. However, these algorithms can not be used for non-homogenous materials since the sound speed is not constant during the entire propagation path. One example of non-homogenous materials is a multi-layer medium consisting of parallel layers with different sound speeds. One application for multi-layer imaging is ultrasonic immersion test where the material under test and the transducer array are immersed in water. The immersion test is often used in NDT, when the surface of the material under test is rough and providing a consistent and uniform couplant, between the transducer array and the test sample in contact test, is not possible. However, the main imaging challenge in immersion test (or any multi-layer medium) is that the assumption of constant speed is not valid, thereby calculating the sound travel times for the backscattered received signals is complicated.

Despite all challenges of imaging a multi-layer medium, several algorithms have been proposed in seismology, biomedical and NDT [25, 26, 31–36]. In [31], a method is proposed for imaging material under immersion test (two-layer medium). In this method, it is needed to use a transducer which can be focused on the surface of the material under immersion test. The focal point of the transducer plays the role of a virtual source for the material under test (second layer); then, the immersion test can be treated as a contact test. However, in this method, the size of the transducer, which determines the transducer focal point, depends on the depth of the first layer.

In [32] and [33], an approximate solution for determining sound travel time in a

multi-layer medium is proposed using Taylor series based on the concept of root-mean-squared (RMS) velocity. The RMS velocity is calculated by averaging the velocities in all layers using a normal incident beam. This method is used in seismology where the sound velocity between seismic layers are small [33]. This technique has also been used in medical ultrasound test since the sound velocity differences between tissue layers are not high [34]. In [35], an RMS velocity based approach is used for calculating sound travel time in synthetic aperture focusing technique (SAFT) for an immersion ultrasonic test. However, this approach has not been used in immersion NDT applications, since the sound travels with two significant different velocities in water and the solid material under immersion test.

Another algorithm, which is applicable for imaging a multi-layer medium with parallel interfaces, is phase shift migration (PSM), which has been originally proposed for seismic waves in [36]. In the PSM algorithm, the sound wave at each depth in the material under test is extrapolated to different depth by multiplying with a complex exponential factor , $e^{(jk_z(c)\Delta z)}$ in frequency domain. Here, Δz is the difference between two depth, and $k_z(c)$ is wavenumber which is a function of the sound speed, c. Since the sound speed is a function of depth in a multi-layer medium, $k_z(c)$ can be recalculated when the wave extrapolated for a different layer with different sound speed. In [25], the PSM algorithm has been investigated for an immersion ultrasonic test in a synthetic aperture focusing scenario, i.e., when a single transducer is used to emulate an array by repeating the test in different positions. The results shows that the PSM algorithm can be implemented in a computationally effective way to obtain a high resolution image of a multi-layer medium or objects immersed in water.

In [26], an imaging algorithm, known as multi-layer Omega-k (MULOK), is proposed, which is a combination of PSM and the wavenumber (ω-k) algorithm to image a multi-layer medium for synthetic aperture focusing scenario. As it is mentioned in the previous subsection, wavenumber algorithm, which is based on Stolt migration algorithm, is effectively applicable for imaging a homogenous or single-layer medium. However, the sound speed is assumed to be constant in Stolt algorithm. In MULOK algorithm, the Stolt algorithm is used for imaging each layer of a multi-layer medium, and the PSM algorithm is used to extrapolate from each layer to another one. This algorithm has less computational complexity comparing to PSM in terms of execution time. These two algorithms (PSM and MULOK) have been applied for imaging multi-layer materials in NDT; however, othetr frequency domain approaches, such as the conventional beamforming technique, the MUSIC method, and the Capon algorithm, are not applicable when the sound velocity is not constant in the material under test. Moreover, the PSM and MULOK algorithms have been proposed for synthetic aperture focusing scenarios and to the best of our knowledge, they have not been applied for the case when an array of transducers is utilized.

2.3 Distributed Source Localization

In most literature on signal processing localization, it is frequently assumed that sources or reflectors are point objects located at far-field of the sensors' location. Based on this mathematical assumption several localization techniques has been proposed including conventional beamforming, MUSIC, ESPRIT and Capon [27–29]. However, in most application such as radar, sonar, wireless communication, medical

diagnosis and non-destructive testing, sources or reflectors are distributed in space. For example in sonar application, the backscattered received signal by seabed is a superposition of plane waves reflected from continuum of directions. Such situation is also can be observed in the radio receivers when the transmitted signal propagates in tropospheric or ionospheric layers. Multi path signals in indoor wireless communication are also been reflected by spatially distributed reflectors [5]. In non destructive testing, cracks to be localized are distributed is space and we need to find the size and the shape of them. In addition, in a multi-layer medium, the interfaces between layers compared to the size of the transducer cannot be considered as a point reflector. One example for multi-layer medium in NDT is immersion ultrasonic test where the interface between water and material under test has the shape of the upper surface of the test sample.

A distributed reflector can be modeled as multiple point sources located close to each other. Distributed reflectors can be modeled either as incoherently distributed (ID) reflectors or as coherently distributed (CD) reflectors. The backscattered signals arriving from different points of a CD reflector are fully correlated, while backscattered signals arriving from different points of an ID reflector are uncorrelated. For example, radio waves reflected by the layers of troposphere or a signal reflected from different points of a rough surface are uncorrelated [5]. One of the first results on distributed source localization was published in [37], where a distributed source is modeled as a collection of finite number of point sources, and then MUSIC and ESPRIT algorithms are used to localize these point sources. However, the number of these point sources are limited by the number of sensors. In [38], dispersed signal

parametric estimation (DISPARE) algorithm has been proposed to estimate the direction of arrival of multiple spatially distributed sources when the number of sources are known. This algorithm is based on weighted projection of eigenvectors of the array signal covariance matrix onto the quasi-noise subspace. This method is more effective than MUSIC if the sources are highly spread. Another early methods for distributed source localization is called distributed source parameter estimator, which is an extended version of MUSIC algorithm and is applicable to both CD and ID sources [5]. In [6], the ESPRIT algorithm has been used to estimate the source parameters including their central angle and angular extension of the sources. The method of [6] can be applied to both CD and ID sources. In [7], a covariance fitting approach has been developed to estimate the parameters of several distributed sources. Taylor series based approximation of the array covariance matrix is used to express this matrix in terms of the central and noncentral moments of the source angular power densities. This algorithm can be applied to multiple ID sources and it has low computational complexity because it does not need an exhaustive search unlike other parametric localization algorithms. In [39], a generalized Capon estimator has been developed for localization of multiple ID sources. This parametric technique estimates the central angle and angular spread of the sources using a 2-dimensional search. It is shown that the performance of this method outperforms the root-MUSIC based method of [40] and the DISPARE method of [38]. In [41], certain properties of the covariance matrix of array signal in case of ID sources and the properties of generalized array steering vector in case of CD sources are used to improve the generalized MUSIC algorithm presented in [5] and generalized Capon algorithm presented in [39]. In [42], a maximum likelihood estimation (MLE) algorithm has been proposed for parametric

estimation of distributed sources. Among parametric estimation methods proposed for distributed source localization, MLE shows a good performance, however, the computational cost for the method is prohibitively high.

In most algorithms for distributed source localization, the main goal is to estimate the parameters of reflector spatial distribution including central direction of arrival and angular spread of the reflected signal. However, the spatial distribution of these signals may not provide much information about the shape of the reflector. however in this dissertation, we use distributed reflector modeling in order to estimate the shape of the reflectors.

Chapter 3

Distributed Reflector Localization for Immersion Test

One of the applications of advanced array processing is in immersion ultrasonic test. Due to large acoustic impedance mismatch between air and solids, a couplant liquid between transducers and the test sample is needed. The couplant could be a thin layer of oil or glycerin, in the case of contact ultrasonic test, or water, in the case of immersion ultrasonic test, where both transducers and the test sample are immersed in water. Immersion test provides a consistent coupling while moving the transducers, especially for test samples with uneven surfaces. However, the sound travels with two different speeds in water and solid material under test. Moreover, the interface between water and the solid material under test, i.e., the upper surface of the test sample, is distributed in space. Therefore, assuming this surface as a point reflector could cause a major error in localizing a crack inside the material under test. In this chapter, we propose a new approach to model the interface between water and solid as well as any crack inside the solid test sample. This approach relies on incoherently distributed reflectors modeling. In this chapter, we assume the case where the material under test has a rough surface and rough crack shape. Then, we model the upper

surface of the test material and any crack inside the test sample as ID reflectors.

In most aforementioned literature on distributed source localization, the main goal is to estimate the parameters of reflector spatial distribution including central direction of arrival and angular spread of the reflected signal. However, the spatial distribution of these signals may not provide much information about the shape of the reflector. In this chapter, we aim to use distributed reflector modeling in order to estimate the shape of the reflectors. To do so, we develop a fitting based approach for parametric estimation of the shape of the interface between two media and that of a crack inside the test material.

The remainder of this chapter is organized as follows. In Section 3.1, we present our data model for the received signal due to the reflection from the upper surface of the test sample. Then, we propose a covariance fitting-based approach to estimate the parameters of the shape of this surface. In Section 3.2, we present a data model for the received signal corresponding to a spatially distributed crack inside the test sample. Then, we use the same approach to localize and estimate the parameters of the shape of the crack. In Section 5.5, we use computer simulation to examine the accuracy of the proposed approach.

3.1 Upper Surface Reflection

3.1.1 Data Model

We consider a uniform linear array (ULA) of k ultrasonic transducers, which are used to obtain an ultrasonic image of a solid test sample immersed in water. To simplify

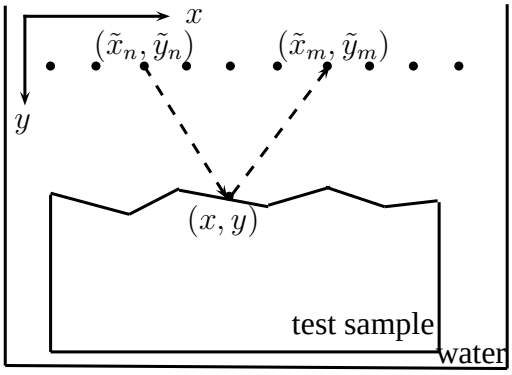

Figure 3.1: Upper surface reflection.

the problem of interest, it is a common practice to assume that the length of the transducers is much larger than the depth of the sample [18,19]. Indeed, the basic idea in 2-dimensional imaging using a 1-dimensional linear array relies on the assumption that in a 2-dimensional model, all quantities are invariant in the third dimension. Our results can be extended in a straightforward manner to a 3-dimensional setup, when a 2-dimensional array is utilized for 3-dimensional volumetric imaging. Each transducer can serve either as a transmitter or as a receiver of ultrasonic waves; however, at each time instance, each transducer can either transmit or receive signal. The immersed sample is assumed to be located in the near field of the array. We model the upper surface of the test sample and any crack inside the sample as distributed reflectors consisting of an infinite number of point reflectors. At each time slot, one of the transducers transmits a probing signal, while other transducers receive the signal reflected from the test sample. One application for this model is in localization of a crack under a weld on a metallic sample which is immersed in water. The system setup and the upper surface reflection of the test sample is depicted in Fig. 3.1. We assume that the reflection coefficients of the reflecting points on the upper surface of

the test sample and those of the points on any crack inside the test sample are random variables. We repeat the ultrasonic test N times. In each test, each transducer fires a probing signal and all transducers receive and record the signals reflected from the sample. Thus, we have k^2 received signals in each test. In the ith experiment, when the nth transducer, located at $(\tilde{x}_n, \tilde{y}_n)$, is transmitting the probing signal $\varphi(t)$, the received signal at the mth transducer, located at $(\tilde{x}_m, \tilde{y}_m)$, due to the reflection from the upper surface of the test sample, is given by

$$\hat{p}_{nm}^{(i)}(t) = \int_{y=C(x)} h(t; \tilde{x}_n, \tilde{y}_n, x, y) \star \varphi(t) \star h(t; \tilde{x}_m, \tilde{y}_m, x, y)\ s_i(x, y)\ dx \tag{3.1.1}$$

where $h(t; \tilde{x}_n, \tilde{y}_n, x, y)$ is the temporal impulse response corresponding to the signal propagation from/to the nth transducer located at $(\tilde{x}_n, \tilde{y}_n)$ to/from a hypothetical point reflector located at (x, y) which resides on the upper surface of the test sample, described as $y = C(x)$, $s_i(x, y)$ is the random reflection coefficient of this point reflector in the ith experiment, and $\star$ represents the continuous-time convolution integral. We model $s_i(x, y)$ as a zero-mean real uniform random variable. We assume that the upper surface consists of infinitely many hypothetical point reflectors and all of them reflect the probing signal back to the array. The integral notation $\int_{y=C(x)}$ in (3.1.1) means that the integration is taken over the length of the upper surface of the test sample in the x direction along the curve $y = C(x)$. Note that $y = C(x)$ describes the upper surface of the test sample. We assume that the temporal impulse response $h(t; \tilde{x}_n, \tilde{y}_n, x, y)$ can be represented as

$$h(t; \tilde{x}_n, \tilde{y}_n, x, y) = a(\tilde{x}_n, \tilde{y}_n, x, y)\ \delta(t - \tau(\tilde{x}_n, \tilde{y}_n, x, y)) \tag{3.1.2}$$

where $a(\tilde{x}_n, \tilde{y}_n, x, y)$ is the amplitude attenuation factor when the signal travels from/to the nth transducer located at $(\tilde{x}_n, \tilde{y}_n)$ to/from a hypothetical point reflector located

at (x, y) on the upper surface of the sample, $\tau(\tilde{x}_n, \tilde{y}_n, x, y)$ is the delay of propagation between the nth transducer located at $(\tilde{x}_n, \tilde{y}_n)$ and a hypothetical point reflector located at (x, y), and $\delta(\cdot)$ is the Dirac delta function. More specifically, we can write $a(\tilde{x}_n, \tilde{y}_n, x, y)$ and $\tau(\tilde{x}_n, \tilde{y}_n, x, y)$ as

$$a(\tilde{x}_n, \tilde{y}_n, x, y) \triangleq \frac{1}{\sqrt{(x-\tilde{x}_n)^2 + (y-\tilde{y}_n)^2}} \tag{3.1.3}$$

$$\tau(\tilde{x}_n, \tilde{y}_n, x, y) \triangleq \frac{\sqrt{(x-\tilde{x}_n)^2 + (y-\tilde{y}_n)^2}}{c} \tag{3.1.4}$$

where c is the velocity of the ultrasonic wave in the medium (water in this case). The frequency representation of (3.1.1) is written as

$$p_{nm}^{(i)}(\omega) = \int_{y=C(x)} g_{\mathrm{w}}(\omega; \tilde{x}_n, \tilde{y}_n, x, y)\ \phi(\omega)\ g_{\mathrm{w}}(\omega; \tilde{x}_m, \tilde{y}_m, x, y)\ s_i(x, y)\ dx \tag{3.1.5}$$

where $p_{nm}^{(i)}(\omega)$ is the frequency-domain representation of the received signal at the mth transducer, when the nth transducer is transmitting the probing signal $\varphi(t)$ (with frequency-domain representation of $\phi(\omega)$) and $g_{\mathrm{w}}(\omega; \tilde{x}_n, \tilde{y}_n, x, y)$ is the frequency response of the propagation in water between the nth transducer, located at $(\tilde{x}_n, \tilde{y}_n)$, and a hypothetical point reflector, located at (x, y). Note that $g_{\mathrm{w}}(\omega; \tilde{x}_n, \tilde{y}_n, x, y)$ can be found by taking the Fourier transform of (3.1.2). Thus, we can write

$$g_{\mathrm{w}}(\omega; \tilde{x}_n, \tilde{y}_n, x, y) = a(\tilde{x}_n, \tilde{y}_n, x, y)\ e^{-j\omega\tau(\tilde{x}_n, \tilde{y}_n, x, y)}. \tag{3.1.6}$$

Using (3.1.6), we can express (3.1.5) as

$$P_{nm}^{(i)}(\omega) = \int_{y=C(x)} a(\tilde{x}_n, \tilde{y}_n, x, y)\ e^{-j\omega\tau(\tilde{x}_n, \tilde{y}_n, x, y)}\ \phi(\omega)\ a(\tilde{x}_m, \tilde{y}_m, x, y)\ e^{-j\omega\tau(\tilde{x}_m, \tilde{y}_m, x, y)}\ s_i(x, y)\ dx. \tag{3.1.7}$$

Using matrix notation, we can express (3.1.7) as

$$\mathbf{P}^{(i)}(\omega) = \int_{y=C(x)} \phi(\omega)\ \mathbf{G}_{\mathrm{w}}(\omega; x, y)\ s_i(x, y)\ dx. \tag{3.1.8}$$

Here, $\mathbf{P}^{(i)}(\omega)$ is a $k \times k$ matrix whose (n,m)th element is $P_{nm}^{(i)}(\omega)$ and $\mathbf{G}_{\mathrm{w}}(\omega; x, y)$ is a $k \times k$ matrix which is defined as

$$\mathbf{G}_{\mathrm{w}}(\omega; x, y) \triangleq \mathbf{g}_{\mathrm{w}}(\omega; x, y)\, \mathbf{g}_{\mathrm{w}}^{T}(\omega; x, y) \tag{3.1.9}$$

where we have used the following definition:

$$\mathbf{g}_{\mathrm{w}}(\omega; x, y) \triangleq [g_{\mathrm{w}}(\omega; \tilde{x}_1, \tilde{y}_1, x, y) \;\; g_{\mathrm{w}}(\omega; \tilde{x}_2, \tilde{y}_2, x, y) \;\; \ldots \;\; g_{\mathrm{w}}(\omega; \tilde{x}_k, \tilde{y}_k, x, y)]^{T}. \tag{3.1.10}$$

Vectorizing both sides of (3.1.8) and taking the measurement noises into account yields

$$\mathbf{p}^{(i)}(\omega) = \mathrm{vec}(\mathbf{P}^{(i)}(\omega)) = \int_{y=C(x)} \phi(\omega)\, \mathbf{v}(\omega; x, y)\, s_i(x, y)\, dx + \boldsymbol{\nu}^{(i)}(\omega) \tag{3.1.11}$$

where $\mathrm{vec}(\cdot)$ is the vectorization operator, $\boldsymbol{\nu}^{(i)}(\omega)$ is a $k^2 \times 1$ complex vector representing all the corresponding measurement noises at the receivers at frequency ω, and $\mathbf{v}(\omega; x, y)$ is a $k^2 \times 1$ complex vector, which is defined as

$$\mathbf{v}(\omega; x, y) \triangleq \mathrm{vec}\left(\mathbf{G}_{\mathrm{w}}(\omega; x, y)\right). \tag{3.1.12}$$

Assuming that the noise and the reflection coefficients of the reflector points are statistically independent random variables and that the noise is zero-mean, we show in the appendix, that the covariance matrix of $\mathbf{p}^{(i)}(\omega)$ can be written as

$$\begin{aligned} \mathbf{R}(\omega) &\triangleq E\{\mathbf{p}^{(i)}(\omega)(\mathbf{p}^{(i)}(\omega))^{H}\} = \sigma_{\nu}^{2}\mathbf{I} + \\ &= \iint\limits_{\substack{y=C(x) \\ y'=C(x')}} |\phi(\omega)|^2 \mathbf{v}(\omega; x, y)\, \mathbf{v}^{H}(\omega; x', y')\, \varrho(x, y, x', y')\, dx\, dx' \end{aligned} \tag{3.1.13}$$

where we have used (3.1.11) in the second equality, σ_{ν}^{2} is the variance of the received noises, $E\{\cdot\}$ stands for the statistical expectation, and

$$\varrho(x, y, x', y') \triangleq E\{s_i(x, y)\, s_i^{*}(x', y')\}. \tag{3.1.14}$$

We model the upper surface as an incoherently distributed (ID) reflector, meaning that the signals reflected by different points of this surface are uncorrelated. Therefore, we can write

$$\varrho(x, y, x', y') = \rho(x, y)\ \delta(x - x')\ \delta(y - y') \tag{3.1.15}$$

where $\rho(x, y)$ is the *reflection correlation density* for a point reflector located at (x, y) on the upper surface and it is only defined for $y = C(x)$. Using (3.1.15), the covariance matrix $\mathbf{R}(\omega)$ in (3.1.13) can be expressed as

$$\mathbf{R}(\omega) = \int\limits_{y=C(x)} \mathbf{V}(\omega; x, y)\ \rho(x, y)\ dx + \sigma_\nu^2 \mathbf{I} \tag{3.1.16}$$

where

$$\mathbf{V}(\omega; x, y) \triangleq |\phi(\omega)|^2\ \mathbf{v}(\omega; x, y)\ \mathbf{v}^H(\omega; x, y). \tag{3.1.17}$$

In the next section, we use this model to develop a covariance fitting based method to estimate the parameters that describe the shape of the upper surface of the test sample.

3.1.2 Estimating the Shape of the Upper Surface

The upper surface of the test sample has two effects: i) it produces a strong interference signal in the backscattered received signal, and ii) its shape determines the array spatial signature of every point inside the material under test. Therefore, to localize a crack inside the test sample, we need to know the shape of the upper surface of the test sample. In this section, using the proposed data model, we aim to find the shape of the upper surface of the test sample. To do so, we approximate the upper

surface with a parametric function and estimate the parameters of this function. For example, in a simple case, if the upper surface is a flat plane, the parameter which has to be estimated is the y coordinate of this plane. In a more complicated scenario, we can approximate the upper surface of the test sample as L piece-wise continuous functions, where the lth piece is described by $y = C_l(x)$, for $(l-1)\Delta x \leq x \leq l\Delta x$, where Δx is the length of each segment on the x axis. Therefore, we can write the covariance matrix expressed in (3.1.16) as

$$\mathbf{R}(\omega) = \sum_{l=1}^{L} \int_{(l-1)\Delta x}^{l\Delta x} \mathbf{V}(\omega; x, C_l(x))\rho(x, C_l(x))dx + \sigma_\nu^2 \mathbf{I}. \tag{3.1.18}$$

We assume that $C_l(x)$ can be described using a parameter vector $\boldsymbol{\vartheta}_l$. For example, if we consider a linear parametrization for each segment, the parameters, to be estimated, are the slope and the y coordinate of the center of each line segment. Let us define the parameter vector $\boldsymbol{\vartheta}$ as

$$\boldsymbol{\vartheta} \triangleq [\boldsymbol{\vartheta}_1 \;\; \boldsymbol{\vartheta}_2 \;\; \ldots, \;\; \boldsymbol{\vartheta}_L]^T \tag{3.1.19}$$

where $\boldsymbol{\vartheta}_l$ is a vector containing the parameters which describe $C_l(x)$. The main idea here is to estimate all parameter vectors $\{\boldsymbol{\vartheta}_l\}_{l=1}^{L}$ using a covariance fitting approach. That is, we estimate the parameters of the shape of the upper surface of the test sample by fitting the analytical covariance matrix with the sample covariance matrix provided by the measurement data. This leads us to solving the following optimization problem:

$$\min_{\boldsymbol{\vartheta}} \quad \sum_{\omega \in \Omega} \|\hat{\mathbf{R}}(\omega) - \mathbf{R}(\omega)\|^2. \tag{3.1.20}$$

Here, Ω is the bandwidth of the probing signal and $\hat{\mathbf{R}}(\omega)$ is the sample covariance matrix of the received signals at frequency ω and it is obtained as

$$\hat{\mathbf{R}}(\omega) = 1/N \sum_{i=1}^{N} \mathbf{p}^{(i)}(\omega)\, \mathbf{p}^{(i)}(\omega)^H \tag{3.1.21}$$

where N is the number of experiments and $\mathbf{p}^{(i)}(\omega)$ is the received signal vector measured in the ith experiment.

In order to solve (3.1.20), we need to calculate $\mathbf{R}(\omega)$, as in (3.1.16), for different parameters of the presumed shape of the upper surface. To do so, we assume a known distribution for $s(x, C_l(x))$, for example, a uniform distribution where its variance can be obtained from $\rho(x, y)$. Therefore, assuming a known distribution for the random reflection coefficients of the points on the upper surface of the test sample, and a parametric function for the shape of the upper surface, the aim is to solve (3.1.20) to estimate the unknown parameters of this function.

To solve (3.1.20), we resort to exhaustive search. Indeed, this problem is highly non-convex and does not seem to be amenable to computationally effective algorithms. However, in most NDT applications, the processing is carried out in an off-line manner. In the next section, we assume that the shape of the upper surface has already been estimated using the algorithm presented in this section, and we aim to localize a crack inside the test sample.

3.2 Reflection from a Crack inside the Sample

3.2.1 Data Model

In this section, we aim to localize a crack inside the test sample. To do so, we model both the upper surface of the sample and a crack inside the sample as spatially distributed reflectors consisting of infinite point reflectors. The model is depicted in Fig. 3.2. We assume that the nth transducer located at $(\tilde{x}_n, \tilde{y}_n)$ is transmitting the probing signal $\varphi(t)$ and the mth transducer located at $(\tilde{x}_m, \tilde{y}_m)$ is receiving the corresponding backscattered signal. In this case, every point on the upper surface reflects a portion of the signal back to the transducer array, while refracting another portion of the probing signal into the test sample. As described in the previous section, we repeat the experiment N times. In the ith experiment, the frequency-domain received signal at an arbitrary point located at (x_2, y_2) on the crack inside the sample, due to the signals refracted by all the points on the upper surface, is given by

$$z_2^{(i)}(\omega; x_2, y_2) = \int_{y_1 = C(x_1)} g_{\mathrm{w}}(\omega; \tilde{x}_n, \tilde{y}_n, x_1, y_1)\phi(\omega) f_{12}^{(i)}(x_1, y_1)\; g_{\mathrm{s}}(\omega; x_1, y_1, x_2, y_2) dx_1 \quad (3.2.1)$$

where $g_{\mathrm{w}}(\omega; \tilde{x}_n, \tilde{y}_n, x_1, y_1)$, as defined earlier, is the frequency response corresponding to signal propagation in water from/to the nth transducer located at $(\tilde{x}_n, \tilde{y}_n)$ to/from a hypothetical point reflector located at (x_1, y_1) that resides on the upper surface of the test sample, described as $y_1 = C(x_1)$, $g_{\mathrm{s}}(\omega; x_1, y_1, x_2, y_2)$ is the frequency response corresponding to signal propagation in solid from/to the point (x_1, y_1) on the upper surface of the sample to/from the point (x_2, y_2) on the crack, and $f_{12}^{(i)}(x_1, y_1)$ is the

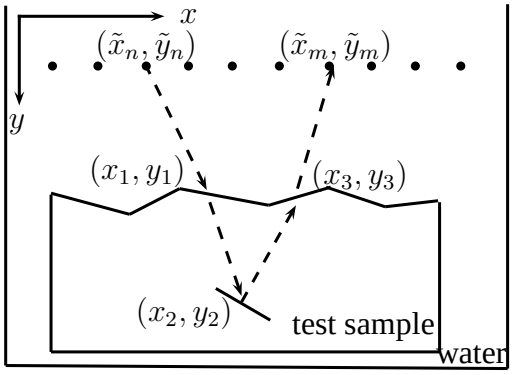

Figure 3.2: Crack reflection.

random refraction coefficient of the point (x_1, y_1) for refraction from water (Medium 1) into the solid (Medium 2) in the ith experiment. In (3.2.1), the integration is taken over $y_1 = C(x_1)$ which is the function describing the upper surface of the test sample.

The received signal $z_2^{(i)}(\omega; x_2, y_2)$ is reflected back by all the point reflectors on the crack towards the upper surface of the sample. At a hypothetical point (x_3, y_3) on the upper surface of the sample, the received signal, which is a superposition of all the signals reflected by point the point reflectors on the crack, can be written as

$$z_3^{(i)}(\omega; x_3, y_3) = \iint\limits_{\substack{y_2=T(x_2)\\ y_1=C(x_1)}} g_{\mathrm{w}}(\omega; \tilde{x}_n, \tilde{y}_n, x_1, y_1)\phi(\omega) f_{12}^{(i)}(x_1, y_1) g_{\mathrm{s}}(\omega; x_1, y_1, x_2, y_2)$$
$$s_i(x_2, y_2) g_{\mathrm{s}}(\omega; x_2, y_2, x_3, y_3) dx_1 dx_2 \tag{3.2.2}$$

where $y_2 = T(x_2)$ is the function describing the crack inside the sample and $s_i(x_2, y_2)$ is the reflection coefficient of a hypothetical point reflector, located at (x_2, y_2) on the crack, in the ith experiment. At any point (x_3, y_3) on the upper surface of the

test sample, the signal $z_3^{(i)}(\omega; x_3, y_3)$ is refracted back to the array. We can write the received signal at the mth receiving transducer as

$$\tilde{P}_{nm}^{(i)}(\omega) = \iiint\limits_{\substack{y_3=C(x_3)\\ y_2=T(x_2)\\ y_1=C(x_1)}} g_{\mathrm{w}}(\omega; \tilde{x}_n, \tilde{y}_n, x_1, y_1)\phi(\omega) f_{12}^{(i)}(x_1, y_1) g_{\mathrm{s}}(\omega; x_1, y_1, x_2, y_2) \times$$
$$s_i(x_2, y_2) g_{\mathrm{s}}(\omega; x_2, y_2, x_3, y_3) f_{21}^{(i)}(x_3, y_3)\, g_{\mathrm{w}}(\omega; \tilde{x}_m, \tilde{y}_m, x_3, y_3) dx_1 dx_2 dx_3. \quad (3.2.3)$$

where $f_{21}^{(i)}(x_3, y_3)$ is the random refraction coefficient of the point (x_3, y_3) for the refraction from the solid (Medium 2) into water (Medium 1) in the ith experiment.

We can write (4.1.1) in the matrix form as

$$\tilde{\mathbf{P}}^{(i)}(\omega) = \iiint\limits_{\substack{y_3=C(x_3)\\ y_2=T(x_2)\\ y_1=C(x_1)}} \phi(\omega)\mathbf{B}(\omega; x_1, y_1, x_2, y_2, x_3, y_3)\gamma_i(x_1, y_1, x_2, y_2, x_3, y_3) dx_1 dx_2 dx_3 \quad (3.2.4)$$

where $\tilde{\mathbf{P}}^{(i)}(\omega)$ is a $k \times k$ matrix whose (n, m)th element is $\tilde{P}_{nm}^{(i)}(\omega)$ and

$$\gamma_i(x_1, y_1, x_2, y_2, x_3, y_3) \triangleq f_{12}^{(i)}(x_1, y_1) s_i(x_2, y_2) f_{21}^{(i)}(x_3, y_3) \quad (3.2.5)$$

$$\mathbf{B}(\omega; x_1, y_1, x_2, y_2, x_3, y_3) \triangleq \mathbf{b}(\omega; x_1, y_1, x_2, y_2)\mathbf{b}^T(\omega; x_3, y_3, x_2, y_2) \quad (3.2.6)$$

$$\mathbf{b}(x_1, y_1, x_2, y_2) \triangleq [g_{\mathrm{w}}(\omega; \tilde{x}_1, \tilde{y}_1, x_1, y_1) g_{\mathrm{s}}(\omega; x_1, y_1, x_2, y_2) \quad (3.2.7)$$
$$g_{\mathrm{w}}(\omega; \tilde{x}_2, \tilde{y}_2, x_1, y_1) g_{\mathrm{s}}(\omega; x_1, y_1, x_2, y_2) \ \ldots\ g_{\mathrm{w}}(\omega; \tilde{x}_k, \tilde{y}_k, x_1, y_1) g_{\mathrm{s}}(\omega; x_1, y_1, x_2, y_2)]^T.$$

Vectorizing both sides of (3.2.4) and taking received noises into account, we can write the vector of frequency-domain signals received by all transducers as

$$\tilde{\mathbf{p}}^{(i)}(\omega) = \mathrm{vec}(\tilde{\mathbf{P}}^{(i)}(\omega)) = \boldsymbol{\nu}^{(i)}(\omega) + \quad (3.2.8)$$
$$\iiint\limits_{\substack{y_3=C(x_3)\\ y_2=T(x_2)\\ y_1=C(x_1)}} \phi(\omega)\mathbf{u}(\omega; x_1, y_1, x_2, y_2, x_3, y_3)\gamma_i(x_1, y_1, x_2, y_2, x_3, y_3) dx_1 dx_2 dx_3$$

where $\boldsymbol{\nu}^{(i)}(\omega)$ is a $k^2 \times 1$ vector collecting all the corresponding measurement noises and

$$\mathbf{u}(\omega; x_1, y_1, x_2, y_2, x_3, y_3) \triangleq \mathrm{vec}(\mathbf{B}(\omega; x_1, y_1, x_2, y_2, x_3, y_3)). \tag{3.2.9}$$

Then, as shown in the appendix, the covariance matrix of $\tilde{\mathbf{P}}^{(i)}(\omega)$ can be written as

$$\begin{aligned}\tilde{\mathbf{R}}(\omega) &= E\{\tilde{\mathbf{p}}^{(i)}(\omega)(\tilde{\mathbf{p}}^{(i)}(\omega))^H\} = \sigma^2\mathbf{I} + \\ &\iiint_{\substack{y_3=C(x_3)\\ y_2=T(x_2)\\ y_1=C(x_1)}} \iiint_{y_3'=C(x_3')\ y_2'=T(x_2')\ y_1'=C(x_1')} |\phi(\omega)|^2 \mathbf{u}(\omega; x_1, y_1, x_2, y_2, x_3, y_3)\mathbf{u}^H(\omega; x_1', y_1', x_2', y_2', x_3', y_3') \times \\ &E(\gamma_i(x_1, y_1, x_2, y_2, x_3, y_3)\gamma_i^*(x_1, y_1, x_2, y_2, x_3, y_3))dx_1'dx_2'dx_3'dx_1dx_2dx_3\end{aligned} \tag{3.2.10}$$

where σ_ν^2 is the noise variance. We further assume that three random variables $f_{12}^{(i)}(x_1, y_1)$, $f_{21}^{(i)}(x_3, y_3)$, and $s_i(x_2, y_2)$ are mutually independent random variables for any (x_1, y_1), (x_2, y_2), and (x_3, y_3). We can then simplify $\tilde{\mathbf{R}}(\omega)$ as

$$\begin{aligned}\tilde{\mathbf{R}}(\omega) = &\iiint_{\substack{y_3=C(x_3)\\ y_2=T(x_2)\\ y_1=C(x_1)}} \iiint_{y_3'=C(x_3')\ y_2'=T(x_2')\ y_1'=C(x_1')} |\phi(\omega)|^2 \mathbf{u}(\omega; x_1, y_1, x_2, y_2, x_3, y_3)\mathbf{u}^H(\omega; x_1, y_1, x_2, y_2, x_3, y_3) \times \\ &\varrho_{12}(x_1, y_1, x_1', y_1')\varrho_c(x_2, y_2, x_2', y_2')\varrho_{21}(x_3, y_3, x_3', y_3')dx_1'dx_2'dx_3'dx_1dx_2dx_3 + \sigma^2\mathbf{I}\end{aligned} \tag{3.2.11}$$

where

$$\varrho_{12}(x_1, y_1, x_1', y_1') \triangleq E(f_{12}^{(i)}(x_1, y_1)f_{12}^{(i)*}(x_1', y_1')) \tag{3.2.12}$$

$$\varrho_{21}(x_3, y_3, x_3', y_3') \triangleq E(f_{21}^{(i)}(x_3, y_3)f_{21}^{(i)*}(x_3', y_3')) \tag{3.2.13}$$

$$\varrho_c(x_2, y_2, x_2', y_2') \triangleq E(s_i(x_2, y_2)s_i^*(x_2', y_2')). \tag{3.2.14}$$

Assuming that the reflectors are incoherently distributed reflectors [5], we can write

$$\varrho_{12}(x_1, y_1, x_1', y_1') = \rho_{12}(x_1, y_1)\delta(x_1 - x_1')\delta(y_1 - y_1') \tag{3.2.15}$$

$$\varrho_c(x_2, y_2, x_2', y_2') = \rho_c(x_2, y_2)\delta(x_2 - x_2')\delta(y_2 - y_2') \tag{3.2.16}$$

$$\varrho_{21}(x_3, y_3, x_3', y_3') = \rho_{21}(x_3, y_3)\delta(x_3 - x_3')\delta(y_3 - y_3'). \tag{3.2.17}$$

where $\rho_c(x_2, y_2)$ is the *reflection correlation density* for a hypothetical point reflector located at (x_2, y_2) on the crack, $\rho_{12}(x_1, y_1)$ is the *refraction correlation density* for a hypothetical refracting point located at (x_1, y_1) on the upper surface of the sample and $\rho_{21}(x_3, y_3)$ is the refraction correlation density for a hypothetical refracting point located at (x_3, y_3) on the upper surface of the sample. Using (3.2.15), (3.2.16), and (3.2.17), we can write (3.2.11) as

$$\tilde{\mathbf{R}}(\omega) = \iiint\limits_{\substack{y_3=C(x_3)\\ y_2=T(x_2)\\ y_1=C(x_1)}} |\phi(\omega)|^2 \mathbf{U}(\omega; x_1, y_1, x_2, y_2, x_3, y_3)\beta(x_1, y_1, x_2, y_2, x_3, y_3)dx_1dx_2dx_3 + \sigma^2\mathbf{I} \tag{3.2.18}$$

where

$$\beta(x_1, y_1, x_2, y_2, x_3, y_3) \triangleq \rho_{12}(x_1, y_1)\rho_c(x_2, y_2)\rho_{21}(x_3, y_3) \tag{3.2.19}$$

$$\mathbf{U}(x_1, y_1, x_2, y_2, x_3, y_3) \triangleq \mathbf{u}(x_1, y_1, x_2, y_2, x_3, y_3)\mathbf{u}^H(x_1, y_1, x_2, y_2, x_3, y_3). \tag{3.2.20}$$

In the next subsection, we use this data model to localize a crack inside the test sample.

3.2.2 Localizing a Crack inside the Sample

In this subsection, assuming that we have estimated the shape of the upper surface of the test sample, we aim to use a covariance fitting based method to find the location and the shape of a crack inside the test sample. To localize the crack inside the sample, we need to find the parameters describing the function $y_2 = T(x_2)$. To do so,

we assume a parametric function for the shape of the crack (such as a line or a hole) and estimate the parameters of this shape (such as slope and the y coordinate of the center of the line or the center and radius of the hole). Let us define $\boldsymbol{\xi} \triangleq (\xi_1, \xi_2, ...\xi_l)$ as the parameter vector for the crack[1]. We assume a known distribution for the variables $f_{12}^{(i)}(x,y)$, $f_{21}^{(i)}(x,y)$ and $s_i(x,y)$. Then, the variances of the random variables $f_{12}(x_2,y_2)$, $f_{21}(x_1,y_1)$, and $s(x_3,y_3)$ are determined by reflection/refraction correlation densities $\rho_c(x_2,y_2)$, $\rho_{12}(x_1,y_1)$, and $\rho_{21}(x_3,y_3)$, respectively. Therefore, the covariance fitting problem can be written as

$$\min_{\boldsymbol{\xi}} \quad \sum_{\omega\in\Omega} \|\hat{\tilde{\mathbf{R}}}(\omega) - \tilde{\mathbf{R}}(\omega)\|^2, \tag{3.2.21}$$

where $\hat{\tilde{\mathbf{R}}}(\omega)$ is the sample covariance matrix obtained from the received signals due to the reflection of the crack inside the test sample which is defined as

$$\tilde{\hat{\mathbf{R}}}(\omega) = 1/N \sum_{i=1}^{N} \tilde{\mathbf{p}}^{(i)}(\omega)\ (\tilde{\mathbf{p}}^{(i)}(\omega))^H. \tag{3.2.22}$$

Here, N is the number of experiments and $\tilde{\mathbf{p}}^{(i)}(\omega)$ is the received signal vector measured in the ith experiment. Note that the array received signals includes the backscattered signal from the upper surface and the backscattered signal reflected by the crack inside the test sample. While solving (3.2.21), we assume that we have already eliminated the signal backscattered from the upper surface of the test sample. Note that to solve (3.2.21), we need to use the knowledge of the shape of the upper surface which we have already estimated in Subsection 3.1.2.

Remark: The algorithm we use in this work is exhaustive search and the degrees of freedom is equal to the number of unknown parameters used to characterize the

[1]It appears that an appropriate model for a crack inside a test sample is a piece-wise linear function [19].

surfaces of interest. In particular, in the covariance fitting problem (3.1.20), which is used to estimate the shape of the upper surface, the number of the degrees of freedom is equal to the length of parameter vector $\boldsymbol{\vartheta}$. In the covariance fitting problem (3.2.21), which is used to estimate the shape of the crack, the number of the degrees of freedom is equal to the length of the parameter vector $\boldsymbol{\xi}$. Note that the computational complexity of covariance fitting is high in this particular application. However, this approach is amenable to parallel processing which significantly reduces the processing time. Indeed, signal processing for NDT applications is often done off-line using parallel processors and/or grid computing. Hence, the computational complexity of covariance fitting is indeed affordable in NDT industries.

3.3 Simulation Results

In this section, we present the results of our numerical simulations to examine the accuracy of the proposed approach for reflector localization in an ultrasonic immersion non-destructive test. It is worth mentioning that in our simulation results, we assume that the measurements contain reflection from both the upper surface and from the crack. Then, we use time gating to separate the upper surface reflection form the crack reflection. Note that the reflection from the crack depends not only on the crack geometry but also on the shape of the upper surface. However, the upper surface reflection does not depend on the crack geometry, and hence, time gating the upper surface reflections will provide us with a set of signals which do not depend on the crack geometry, and thus, these signals can be used to determine the shape of this surface. In other words, we are estimating the shape of the upper surface in

the presence of the crack and use the so-obtained estimate to extract the shape of the crack. Note that alternating between estimating the shape of the upper surface and estimating the shape of the crack does not help to improve the quality of the estimates as the time-gated signals corresponding to the upper surface reflection do not depend on the shape of the crack. Processing the measurements as they are, i.e., without time gating, with the aim to simultaneously estimate the parameters of the upper surface and those of the crack, is another approach. However, such an approach would result in a higher dimensional search space as compared to the search space for each set of the upper surface or the crack parameters. Moreover, in such an approach, the computational complexity associated with computing the covariance matrix for each value of the concatenated parameter vector is prohibitively high. We assume that a uniform linear array of $k = 16$ omnidirectional ultrasonic transducers is used for testing a welded steel sample, as depicted in Fig. 3.3. The aim is to localize a crack under the weld inside the solid material. To do so, the first step is to estimate the knowledge of the shape of the upper surface of the test sample because we need this shape to find the array spatial signature for any point inside the test sample. In the second step, we use the estimated shape of the upper surface in our data model, to find the location and the parameters of the shape of a crack inside the test sample. We assume that the array has an element pitch (the distance between the center of two adjacent transducers) of $e = 0.63$ mm. The array and the sample are parallel to the x axis, and the array is located on the x axis with the first transducer being located at $x = 0$ mm and $y = 0$ mm. The sample and the array probe are immersed in water. In order to simulate the data for the model proposed, we use an exponential sinusoidal function $\phi(t) = e^{t^2}\cos(2\pi f t)$ as the probing signal with the

center frequency of 3.5 MHz [43]. The frequency bins are chosen symmetrical with respect to the center frequency 3.5 MHz. The distance between adjacent frequencies is chosen 45 KHz, regardless of the size or type of the defect.

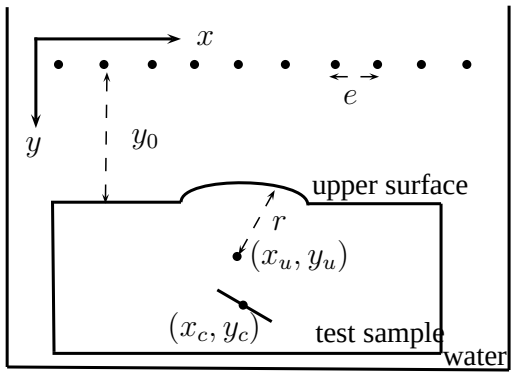

Figure 3.3: A weld on a solid test sample.

We model the shape of the upper surface of the test sample as a piece-wise continuous function consisting of the line segment, described as $y = 30$ mm for $0 \leq x \leq 1$ mm; a circular arch (for the weld cap) with its center located at $(x_u, y_u) = (5, 27)$ mm and a radius of$r = 5$ mm for 1 mm $\leq x \leq$ 9 mm; and another line segment, $y = 30$ mm for 9 mm $\leq x \leq 10$ mm. The parameters which have to be estimated are the center and the radius of the circle and the y-coordinate of the interface which are shown as x_u, y_u, r and y_0, respectively. Here, the parameter vector is given by $\boldsymbol{\vartheta} = [x_u \;\; y_u \;\; r \;\; y_0]^T$, and thus, the number of the degrees of freedom is 4. In Fig. 3.4, we have plotted the root mean square error (RMSE) of the parameter estimates in millimeters versus the number of snapshots, where signal-to-noise-ratio (SNR) is 10 dB. The SNR is defined the ratio of the array received signal power to the noise power at the receiver. In this figure, we have used 20 frequency bins in the optimization problem (3.1.20). This figure shows that using only 150 snapshots results in very small

value of RMSE for the case of SNR = 10 dB. The RMSE curve reaches 0.05 mm (our search grid size) for the number of snapshots more than 150 because the RMSE of the parameter estimates cannot get smaller than our grid size. In Fig. 3.5, we observe the effect of the number of frequency bins used in the optimization problem. This figure shows the RMSE of the parameter estimates versus SNR for different numbers of frequency bins. In order to obtain the sample covariance matrix for this figure, 150 statistically independent snapshots are produced. As shown in this figure, using more frequency bins results in smaller values for detection SNR threshold. We can observe that for estimating the parameters of the shape of the upper surface, using only one frequency bin yields very small error around 0.22 mm in the case of SNR = 4 dB.

In the second step of this simulation, after estimating the parameters of the upper surface, we use the estimated upper surface parameters to localize a crack under the weld. To do so, we assume that the crack is a line whose center point and slope have to be estimated. The length of the crack is chosen to be 0.5 mm which is, according to the guideline and the model recommended in [44], is an appropriate value for the minimum crack size. Longer cracks can then be modeled using a piece-wise linear function with minimum length of each piece being equal to 0.5 mm. The crack is a line segment with a length of 0.5 mm and a slope of $\alpha = 1$, and its center point is located at $x_c = 2$ mm and $y_c = 0.25$ mm. Here, the parameter vector for parameterizing the shape of the crack is given by $\boldsymbol{\xi} = [x_c \;\; y_c \;\; \alpha]^T$ and thus the number of the degrees of freedom is 3. In Fig. 3.6, we show the RMSE of the estimated parameters of the crack inside the test sample versus number of snapshots for SNR = 10 dB. The plot shows that 2000 snapshots are needed in order to have a minimum possible value for RMSE. This minimum RMSE depends on the search grid size and the

RMSE of the upper surface parameters estimation. In Fig. 3.7, we observe the effect of the number of frequency bins, which have been used in the optimization problem in (3.2.21), for localizing the crack. In order to obtain the sample covariance matrix for this figure, $N = 2000$ statistically independent snapshots are produced. This figure shows the RMSE of the estimated parameters versus SNR for different number of frequency bins. We observe that only one frequency bin results in a good RMSE value comparing to the case of using 20 frequency bins in the optimization problem which has more computational complexity.

In Fig. 3.8, we compare the performance of our proposed method with that of the root mean squared (RMS) velocity based method of [32]. The latter method approximates the array measurements with a data model which corresponds to a single-layer homogenous medium, where the sound propagation velocity is approximated as the weighted average of the squared value of the sound propagation velocities in the two layers. In this averaging, the weight of the squared value of the velocity in each layer is the ratio of normal incidence one-way travel time in that layer to total normal incidence one-way travel time. Using the so-called RMS velocity, the travel time corresponding to each potential point reflector in the second layer is calculated as the ratio of the distance traveled by the wave to the RMS velocity. As can be seen from Fig. 3.8, our method significantly outperforms the RMS velocity based method.

In Fig. 3.9, assuming the same array configuration and the same test setup as the previous example, we show an example where the true shape of the crack is an arch, while we approximate it with a piece-wise function consisting of two line segments. This figure shows clearly that even with a discrepancy between the true and the presumed crack shape, our proposed algorithm is capable of obtaining a good

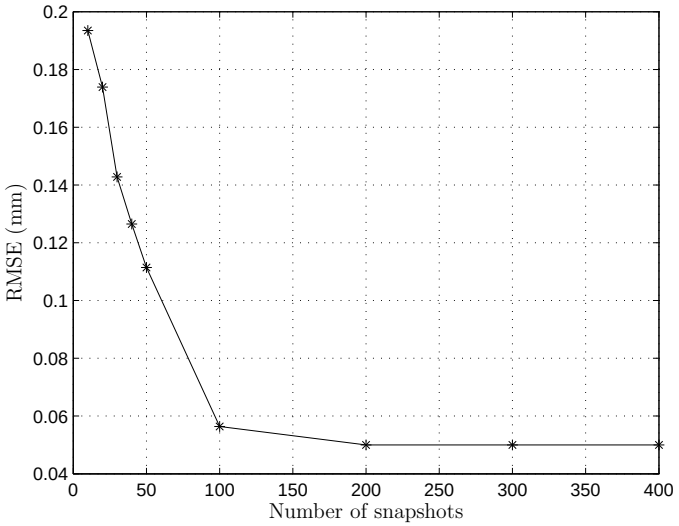

Figure 3.4: The RMSE of the estimated parameters of the shape of the upper surface of the test sample versus the number of snapshots for SNR=10 dB.

approximation for the crack shape.

3.4 Conclusions

In this chapter, we proposed a covariance fitting approach to localize reflectors in a water immersion non-destructive test, where an ultrasonic array is used. To do so, we modeled the sound reflectors inside the material under test as incoherently distributed reflectors consisting of an infinite number of point reflectors. These reflectors include the interface between water and a solid material under ultrasonic test and any crack inside the test sample. In order to localize a crack inside the test sample in this immersion test, the knowledge of the shape of the upper surface of the test sample is required as this shape determines the array spatial signature of the points inside

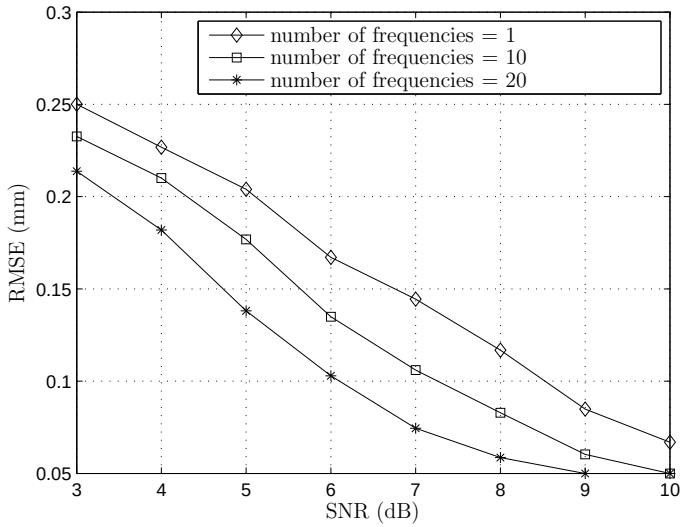

Figure 3.5: The RMSE of the estimated parameters of the shape of the upper surface of the test sample versus SNR for different number of frequency bins.

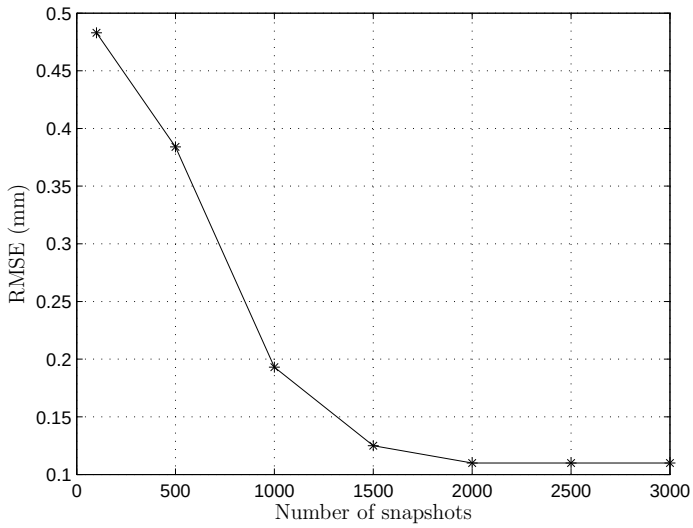

Figure 3.6: The RMSE of the estimated parameters of the crack inside the test sample versus the number of snapshots for SNR = 10 dB.

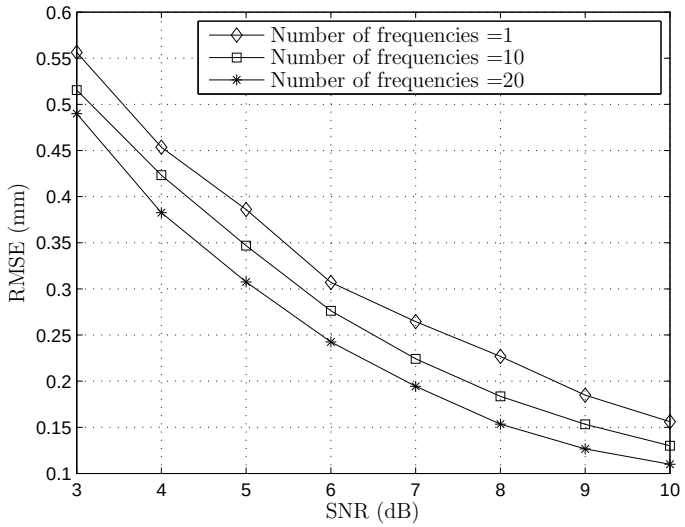

Figure 3.7: The RMSE of the estimated parameters of the crack inside the test sample versus SNR for different number of frequency bins.

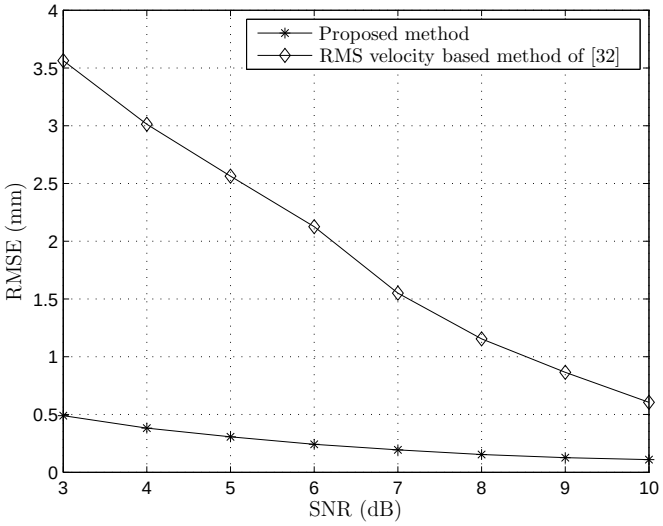

Figure 3.8: The RMSE of the estimated parameters of the crack inside the test sample versus SNR.

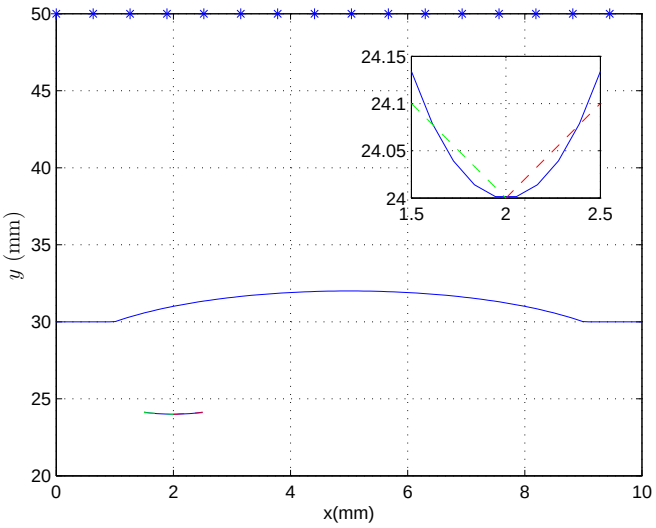

Figure 3.9: Estimation of a curved crack by approximating it with two piece-wise linear segments; SNR=10 dB.

the test sample. Therefore, we proposed a distributed reflector modeling approach to characterize the interface between water and a solid test sample as well as any crack inside the solid test sample. Our approach relies on the so-called incoherently distributed reflector modeling, where a distributed reflector can be modeled as infinitely many point sources located close to each other. Using such a modeling, we presented our data model in a two-dimensional coordinate system, and then developed a covariance fitting based approach to estimate the parameters of the shape of the interface between the two media and those of the shape of a crack inside the test material. Our numerical experiments show that our proposed approach yields a lower root mean squared error for the parameter estimates, compared to a state-of-the-art method, called root mean squared velocity technique.

The approach provided in this chapter relies on the repetition of the ultrasonic

experiment. In the next chapter, we use the distributed source modeling for the interfaces between the layers of a multi-layer medium in order to develop a new array spatial signature. Then we explain how this new array spatial signature can be used in the existing imaging algorithms.

Chapter 4

A New Array Spatial Signature Model

In this chapter, we aim to image a multi-layer medium. To do so, we model the interfaces between layers of a multi-layer medium as spatially distributed sources consisting of infinite number of point sources [5–7, 37–39]. Then, we use this model to develop a new array spatial signature for all the points inside a multi-layer medium. This new array spatial signature can be used in existing imaging techniques including beamforming, MUSIC, and Capon in order to image multi-layer materials. These algorithms traditionally are applied for a homogeneous medium where the sound velocity is constant in the medium [27–30].

The remainder of this chapter is organized as follows. In Section4.1, we present our data model for the array received signal using the concept of spatially distributed source modeling. First, in Subsection4.1.1, we model the array received signal corresponding to the reflection of the points located in the second layer of a two-layer material under ultrasonic test. In Subsection4.1.2, we extend the proposed model for the backscattered signal corresponding to the point reflectors located in the l-th layer of a multi-layer material under ultrasonic test. In Section4.2, we use the array

spatial signature model, developed in Subsection4.1.1, in some existing imaging algorithms including beamforming, MUSIC, and Capon in order to image the second layer of the material under test. In Section5.4, we use computer simulation as well as experimental data, to examine the accuracy of the proposed model.

4.1 Data Model

4.1.1 Two-layer Medium

We consider a uniform linear array of k ultrasonic transducers which are used to image a two-layer test sample with the aim to detect flaws (such as cracks) inside the second layer. The sound propagation speed in each layer is different from that in the other layer. Each transducer can transmit and receive ultrasonic waves. To conduct an ultrasonic test, all transducers transmit a sound wave, one after another. When one transducer transmits the sound wave, all transducers, including the one transmitting, receive the signal backscattered from the test sample. We assume that there is enough time delay between firing different transducers in order to avoid any undesired interference. Fig. 4.1 shows the configuration of the ultrasonic test setup and a typical wave propagation path corresponding to the reflection from a point scatterer located in the second layer of the test sample. Assuming such a test setup, we derive a frequency-domain model for transducer measurements. Further, we assume that the probing signal is a narrow-band signal with center frequency ω. In practice, the ultrasonic probing signal is a wide-band signal with center frequency around $2-10$MHz. In Section 4.2.4, we will discuss how this model can be used in a wide-band scenario.

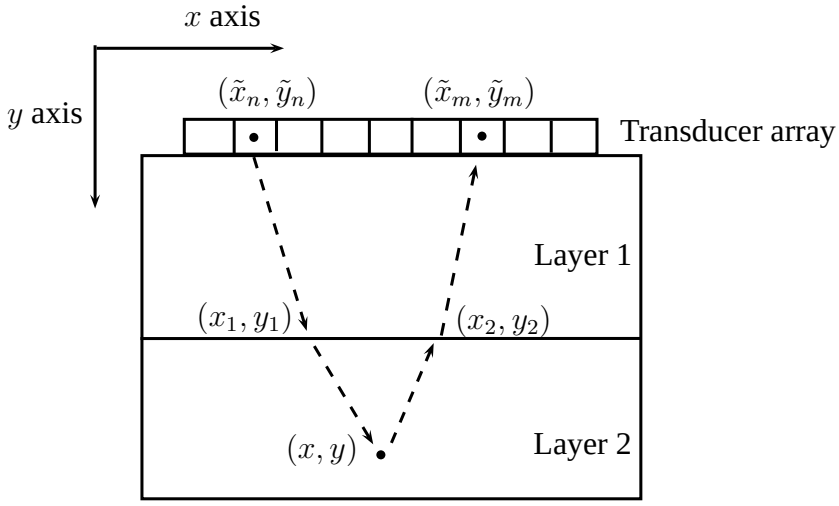

Figure 4.1: A typical propagation path for the signal backscattered from a point scatterer inside the second layer of a two-layer test sample.

We assume that the material under test consists of two layers with two different sound velocities. In case of a contact test, the transducer array is placed on the surface of the first layer of a two-layer solid test sample and a thin layer of gel is used as a couplant between the array and the first layer of the test sample. In an immersion ultrasonic test, the ultrasonic array and a solid test sample are immersed in a liquid such as water. In this case, the first layer of the material under test is the liquid and the second layer is the solid test sample. We note that in both cases, the first discontinuity in the wave propagation path occurs at the interface between the two layers. This interface reflects part of the propagating sound wave back to the transducer array and refracts the other portion of the sound wave into the second layer, thereby playing the role of a (distributed) source, which emits ultrasonic waves towards the points inside the second layer. Indeed, this interface is a continuous surface spread in space, and thus, we model it as a spatially distributed source consisting of infinite number of

point sources [5–7,37–39]. We also assume that the length of the transducers is much larger than the depth of the test sample and derive our data model in a 2-dimensional coordinate system. The idea of 2-dimensional imaging using a 1-dimensional linear array is a common practice in ultrasonic NDT, where all quantities are assumed to be invariant in the third dimension [18, 19]. Our data model can be expressed for 3-dimensional volumetric imaging, when a 2-dimensional array is utilized. In this section, our goal is to derive a data model for the array signal measurements corresponding to backscattering from the point scatterers inside the second layer of the test sample. To develop such a model, we assume that a hypothetical point scatterer is located at the coordinate (x, y) inside the second layer of the material under test. Fig. 4.1 shows the sound path corresponding to this point scatterer and two arbitrary refracting points on the interface between the two layers. We assume that the n-th transducer located at $(\tilde{x}_n, \tilde{y}_n)$ is transmitting the sound wave. The transmitted sound wave is the response of the transmitting transducer to the probing signal $\psi(t)$ (with frequency domain representation $\Psi(\omega)$). This transmitted sound wave is refracted into the second layer of the test sample, by all the points on the inter-layer interface. Then, this wave is scattered by the point scatterer located at (x, y) inside the second layer of the material under test back towards the interface. At the interface, the sound wave is refracted, back towards the transducer array. This backscattered sound wave is received by all transducers. The received signal at the receiving transducer is the response of the receiving transducer to the received sound wave from all the points on the interface.

It is worth noting that there are two equivalent approaches to tackle the problem of refraction of a non-planar (for example spherical or cylindrical) wave at the interface

between two media with two different velocities. The first approach is the Weyl's decomposition which leads to the Weyl's integral. The main idea in the Weyl approach is to represent the incident wave as a superposition of infinite number of plane waves. To do so, the incident wave is expressed, using inverse (spatial) Fourier transform, as a Fourier integral of infinite number of plane waves. Then, Snell's law can be used to model the refraction of each of these plane waves. That is, each plane wave is refracted according to Snell's law. Also, each of these plane waves in the Weyl's integral is required to be multiplied by a transmission coefficient described by Snell's law when traveling from one medium to another one [45]. It is worth mentioning that when using Weyl's approach, spcial attention has to be paid to the concept of critical angle.

The second approach relies on Huygens-Fresnel principle. According to this principle, a wave field on a surface can determine the wave field off that surface. More specifically, each point on the surface can be viewed as a source of a secondary wave. The superposition of these secondary sources on the surface determines the strength of the wave at any point off that surface. This formulation leads to the Rayleigh-Sommerfeld integral. In this work we use the Huygen's principle to write the Rayleigh-Sommerfeld integral over the interface between the two media in our test setup.

Therefore, the received signal at the m-th transducer, located at $(\tilde{x}_m, \tilde{y}_m)$, corresponding to the backscattering from the point scatterer located at (x, y) inside the

second layer, can be written as

$$P_{nm}(\omega;x,y)=\iint_{-\infty}^{+\infty}\phi(\omega)B_n(\omega;x_1,y_1)g_1(\omega;\tilde{x}_n,\tilde{y}_n,x_1,y_1)\ f_{12}(\omega,x_1,y_1,x,y)\ g_2(\omega;x_1,y_1,x,y)$$
$$s(x,y)\ g_2(\omega;x_2,y_2,x,y)\ f_{21}(\omega,x_2,y_2,\tilde{x}_m,\tilde{y}_m)\ g_1(\omega;\tilde{x}_m,\tilde{y}_m,x_2,y_2)B_m(\omega;x_2,y_2)dx_1dx_2 \tag{4.1.1}$$

where $B_n(\omega;x_1,y_1)$ is the beam-pattern gain of the n-th transducer element towards a point located at (x_1,y_1) on the interface. Note that $B_n(\omega;x_1,y_1)$ depends on the type and the shape of the transducer. Also, $g_1(\omega;\tilde{x}_n,\tilde{y}_n,x_1,y_1)$ is the frequency response of the linear time invariant (LTI) system which models the signal propagation in the first layer from/to the n-th transducer located at $(\tilde{x}_n,\tilde{y}_n)$ to/from a hypothetical point located at (x_1,y_1) which resides on the interface between the two-layers, $g_2(\omega;x_1,y_1,x,y)$ is the frequency response of the LTI system which models the signal propagation in the second layer of the test sample from/to the point (x_1,y_1) on this interface to/from the point scatterer located at (x,y) inside the second layer, and $s(x,y)$ is the scattering coefficient of the hypothetical point scatterer located at (x,y) inside the second layer. Also, $f_{12}(\omega,x_1,y_1,x,y)$ is the transmission coefficient from Layer 1 into Layer 2 from point (x_1,y_1) on the interface toward the point located at (x,y) inside the second layer, and $f_{21}(\omega,x_2,y_2,\tilde{x}_m,\tilde{y}_m)$ is the transmission coefficient from Layer 2 into Layer 1, from the point located at (x_2,y_2) on the interface toward the m-th transducer located at $(\tilde{x}_m,\tilde{y}_m)$. Based on Huygens-Fresnel principle, $f_{12}(\omega,x_1,y_1,x,y)$ and $f_{21}(\omega,x_2,y_2,\tilde{x}_m,\tilde{y}_m)$ can be written as [46]

$$f_{12}(\omega,x_1,y_1,x,y)=\frac{j\omega|y-y_1|}{4\pi c_2 d(x_1,y_1,x,y)} \tag{4.1.2}$$

$$f_{21}(\omega,x_2,y_2,\tilde{x}_m,\tilde{y}_m)=\frac{j\omega|y_2-\tilde{y}_m|}{4\pi c_1 d(\tilde{x}_m,\tilde{y}_m,x_2,y_2)} \tag{4.1.3}$$

where $d(x_1, y_1, x, y)$ is the distance between a hypothetical point located at (x_1, y_1) on the interface between the two-layers, and a hypothetical point scatterer located at (x, y) inside the second layer. Also $d(\tilde{x}_m, \tilde{y}_m, x_2, y_2)$ is the distance between the m-th transducer, located at $(\tilde{x}_m, \tilde{y}_m)$, and a point located at (x_2, y_2), on the interface between the two-layers.

We also need to emphasize that, assuming that all the transducers are identical, we define $\phi(\omega)$ as

$$\phi(\omega) = \Psi(\omega) H_T(\omega) H_R(\omega) \tag{4.1.4}$$

where $\Psi(\omega)$ is the narrow-band probing signal at frequency ω, $H_T(\omega)$ is the frequency response of the transmitting transducer , and $H_R(\omega)$ is the frequency response of the receiving transducer. We can write (4.1.1) as

$$P_{nm}(\omega; x, y) = s(x, y)\phi(\omega)\ u_n(\omega; x, y) v_m(\omega; x, y) \tag{4.1.5}$$

where $u_n(\omega; x, y)$ and $v_m(\omega; x, y)$ are the frequency responses of the LTI systems which model the propagation of the sound wave along the transmission path (the path from the transmitting transducer to a hypothetical scatterer located at (x, y)) and the reception path (the path from a hypothetical scatterer located at (x, y) to the receiving transducer), respectively, i.e.,

$$u_n(\omega; x, y) \triangleq \int_{-\infty}^{+\infty} B_n(\omega; x_1, y_1) g_1(\omega; \tilde{x}_n, \tilde{y}_n, x_1, y_1) f_{12}(\omega, x_1, y_1, x, y) g_2(\omega; x_1, y_1, x, y) dx_1 \tag{4.1.6}$$

$$v_m(\omega; x, y) \triangleq \int_{-\infty}^{+\infty} B_m(\omega; x_2, y_2) g_1(\omega; \tilde{x}_m, \tilde{y}_m, x_2, y_2) f_{21}(\omega, x_2, y_2, \tilde{x}_m, \tilde{y}_m) g_2(\omega; x_2, y_2, x, y) dx_2. \tag{4.1.7}$$

In our data model, we assume that the material under test is a lossless and non-dispersive material. We also assume that the transducers and the defects inside the material under test are long in the third dimension. Hence, we model the frequency responses $g_1(\omega;\tilde{x}_n,\tilde{y}_n,x,y)$ and $g_2(\omega;x_1,y_1,x,y)$ as

$$g_1(\omega;\tilde{x}_n,\tilde{y}_n,x_1,y_1) = a_1(\tilde{x}_n,\tilde{y}_n,x_1,y_1)\; e^{-j\omega\tau_1(\tilde{x}_n,\tilde{y}_n,x_1,y_1)} \tag{4.1.8}$$

$$g_2(\omega;x_1,y_1,x,y) = a_2(x_1,y_1,x,y)\; e^{-j\omega\tau_2(x_1,y_1,x,y)}. \tag{4.1.9}$$

where

$$a_1(\tilde{x}_n,\tilde{y}_n,x,y) \triangleq \frac{1}{\sqrt{d(\tilde{x}_n,\tilde{y}_n,x_1,y_1)}} \tag{4.1.10}$$

$$\tau_1(\tilde{x}_n,\tilde{y}_n,x,y) \triangleq \frac{d(\tilde{x}_n,\tilde{y}_n,x_1,y_1)}{c_1} \tag{4.1.11}$$

$$a_2(x_1,y_1,x,y) \triangleq \frac{1}{\sqrt{d(x_1,y_1,x,y)}} \tag{4.1.12}$$

$$\tau_2(x_1,y_1,x,y) \triangleq \frac{d(x_1,y_1,x,y)}{c_2}. \tag{4.1.13}$$

Here, $d(\tilde{x}_n,\tilde{y}_n,x_1,y_1)$ is the distance between the n-th transducer, located at $(\tilde{x}_n,\tilde{y}_n)$, and a point located at (x_1,y_1), on the interface between the two-layers, $d(x_1,y_1,x,y)$ is the distance between the point located at (x_1,y_1), on the inter-layer interface, and the point scatterer located at (x,y), inside the second layer, c_1 is the speed of sound in the first layer, and c_2 is the speed of sound in the second layer. Note that in (4.1.10) and (4.1.12), we ignore a constant factor which ensures that $a_1(\tilde{x}_n,\tilde{y}_n,x,y)$ and $a_2(x_1,y_1,x,y)$ are dimensionless. Indeed such a constant will not affect the performance of the forthcoming imaging schemes. We can write (4.1.5) as

$$P_{nm}(\omega;x,y) = s(x,y)\;\phi(\omega)U_{nm}(\omega;x,y) \tag{4.1.14}$$

where $U_{nm}(\omega;x,y)$ is the (n,m)-th element of the $k\times k$ matrix $\mathbf{U}$ which is defined as

$$\mathbf{U}(\omega; x, y) \triangleq \mathbf{u}(\omega; x, y)\ \mathbf{v}^T(\omega; x, y) \tag{4.1.15}$$

$$\mathbf{u}(\omega; x, y) \triangleq [u_1(\omega; x, y)\ \ u_2(\omega; x, y)\ \ ...\ \ u_k(\omega; x, y)]^T. \tag{4.1.16}$$

$$\mathbf{v}(\omega; x, y) \triangleq [v_1(\omega; x, y)\ \ v_2(\omega; x, y)\ \ ...\ \ v_k(\omega; x, y)]^T. \tag{4.1.17}$$

Here, $\mathbf{u}(\omega; x, y)$ is a $k \times 1$ vector of array spatial signature, at frequency ω, corresponding to the transmitting transducers at the hypothetical point scatterer located at (x, y), inside the second layer, and $\mathbf{v}(\omega; x, y)$ is a $k \times 1$ vector of array spatial signature, at frequency ω, corresponding to the receiving transducers at the hypothetical point scatterer located at (x, y), inside the second layer. The new array spatial signatures $\mathbf{u}(\omega; x, y)$ and $\mathbf{v}(\omega; x, y)$, can be used in different algorithms to image the second layer of the material under test. Note that $P_{nm}(\omega; x, y)$ in (4.1.14) is the received signal corresponding to the backscattering from only one scatterer point located at (x, y) in the second layer. The received signal due to the backscattering of all point scatterers inside the second layer of the test sample can be written as

$$P_{nm}(\omega) = \phi(\omega) \sum_{i=1}^{n_2} U_{nm}(\omega; \hat{x}_i, \hat{y}_i)\ s(\hat{x}_i, \hat{y}_i) \tag{4.1.18}$$

where n_2 is the number of scatterer points inside the second layer and $(\hat{x}_i, \hat{y}_i)$ is the location of the i-th scatterer point inside the second layer. To consider all k^2 received signals in the presence of noise, we can collect all the received signals in a matrix form as

$$\mathbf{P}(\omega) = \phi(\omega) \sum_{i=1}^{n_2} \mathbf{U}(\omega; \hat{x}_i, \hat{y}_i)\ s(\hat{x}_i, \hat{y}_i) + \boldsymbol{\nu}(\omega) \tag{4.1.19}$$

where $\mathbf{P}(\omega)$ is a $k \times k$ matrix whose (n, m)-th element is $P_{nm}(\omega)$, and $\boldsymbol{\nu}(\omega)$ is a $k \times k$ matrix whose (n, m)-th element is the received noise at the m-th transducer, when the n-th transducer is transmitting the the sound wave.

4.1.2 Multi-layer Medium

In this section, we aim to extend our data model presented in Section 4.1.1, for the a multi-layer test sample. We consider a test sample consisting of l layers under ultrasonic test. Each layer has a different sound velocity. The goal is to derive a data model for the reflection of the point reflectors located at the l-th layer of the material under teat. Assuming a uniform linear array of k ultrasonic transducers. The test is conducted as it is explained in Section 4.1.1. We consider the interfaces between the layers as spatially distributed sources refracting the probing signals into the lower layers. We model these interfaces as infinitely many point sources. We assume that there is a point reflector located at (x, y) inside the l-th layer of the test sample. A typical sound path for the reflection of this point reflector is depicted in Fig. 4.2. We assume that the nth transducer located at $(\tilde{x}_n, \tilde{y}_n)$ is transmitting the probing signal $\phi(\omega)$, and the mth transducer located at $(\tilde{x}_m, \tilde{y}_m)$ is receiving the signal back-scattered by the test sample. The signal received at the mth transducer corresponding to the point reflector at (x, y) inside the l-th layer, can be written as

$$P_{nm}^{(l)}(\omega; x, y) = \gamma(x, y)\ \phi(\omega) u_n^{(l)}(\omega; x, y) u_m^{(l)}(\omega; x, y) \tag{4.1.20}$$

where $\gamma(x, y)$ is defined as

$$\gamma(x, y) \triangleq f_{12} f_{21} f_{23} f_{32}\ ... f_{(l-1)l} f_{l(l-1)}\ s(x, y). \tag{4.1.21}$$

Here, f_{ij} is the refraction coefficient from Layer i into Layer j, $s(x, y)$ is the reflection coefficient of the point reflector located at (x, y), and $u_n^{(l)}(\omega; x, y)$ and $u_n^{(l)}(\omega; x, y)$ are the frequency responses, corresponding to the transmission and reception paths and

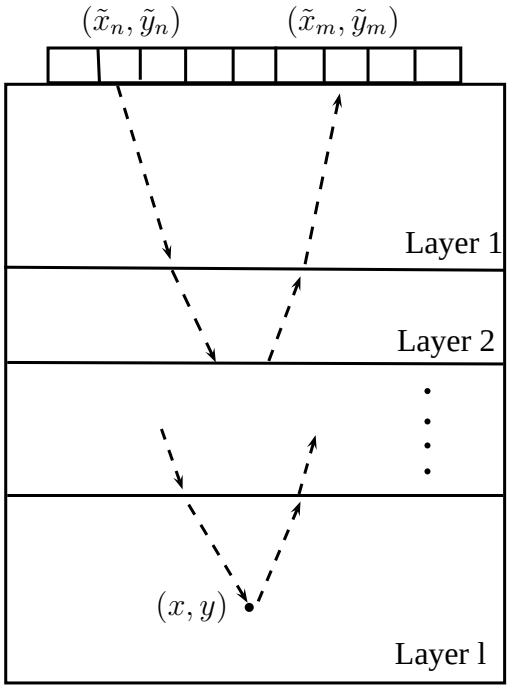

Figure 4.2: Reflection of a point reflector inside the lth layer of the test sample.

they are defined as

$$u_n^{(l)}(\omega; x, y) \triangleq \int_{y_{l-1}=C_{l-1}(x_{l-1})} \dots \int_{y_2=C_2(x_2)} \int_{y_1=C_1^{(n)}(x_1)} g_1(\omega; \tilde{x}_n, \tilde{y}_n, x_1, y_1)$$
$$g_2(\omega; x_1, y_1, x_2, y_2) \dots g_{(l)}(\omega; x_{l-1} y_{l-1}, x, y) dx_1 dx_2 dx_{l-1} \tag{4.1.22}$$
$$u_m^{(l)}(\omega; x, y) \triangleq \int_{y_{l-1}=C_{l-1}(x_{l-1})} \dots \int_{y_2=C_2(x_2)} \int_{y_1=C_1^{(m)}(x_1)} g_1(\omega; \tilde{x}_m, \tilde{y}_m, x_1, y_1)$$
$$g_2(\omega; x_1, y_1, x_2, y_2) \dots g_{(l)}(\omega; x_{l-1} y_{l-1}, x, y) dx_1 dx_2 dx_{l-1}. \tag{4.1.23}$$

Note that for the sake of simplicity in the multi-layer model, we assumed that the transmission coefficients are constant and the transducers are omni-directional. We can rewrite (4.1.20) as

$$P_{nm}^{(l)}(\omega; x, y) = \gamma(x, y)\ \phi(\omega) U_{nm}^{(l)}(\omega; x, y) \tag{4.1.24}$$

where $U_{nm}^{(l)}(\omega; x, y)$ is the (n, m)th element of the $k \times k$ matrix $\mathbf{U}^{(l)}(\omega; x, y)$, is defined as

$$\mathbf{U}^{(l)}(\omega; x, y) \triangleq \mathbf{u}^{(l)}(\omega; x, y)\ (\mathbf{u}^{(l)}(\omega; x, y))^T \tag{4.1.25}$$

$$\mathbf{u}^{(l)}(\omega; x, y) \triangleq [u_1^{(l)}(\omega; x, y)\ \ u_2^{(l)}(\omega; x, y)\ \ ...\ \ u_k^{(l)}(\omega; x, y)]^T. \tag{4.1.26}$$

Note that $P_{nm}^{(l)}(\omega; x, y)$ is the received signal corresponding to the reflection of only one reflector point in the l-th layer located at (x, y). However, the received signal is due to reflections from the superposition of all reflector points inside the l-th layer of the test sample. Therefore, the received signal corresponding to all point reflectors in the l-th layer can be written as

$$P_{nm}^{(l)}(\omega) = \phi(\omega) \sum_{i=1}^{n_l} U_{nm}^{(l)}(\omega; \hat{x}_i, \hat{y}_i)\ \gamma(\hat{x}_i, \hat{y}_i) \tag{4.1.27}$$

where n_l is the number of reflector points in the l-th layer and $(\hat{x}_i, \hat{y}_i)$ is the location of the ith reflector point inside the l-th layer. To consider all k^2 received signals in the presence of noise, we can collect all the received signals in a matrix form as

$$\mathbf{P}^{(l)}(\omega) = \phi(\omega) \sum_{i=1}^{r_l} \mathbf{U}^{(l)}(\omega; \hat{x}_i, \hat{y}_i)\ \gamma(\hat{x}_i, \hat{y}_i) + \boldsymbol{\nu} \tag{4.1.28}$$

where $\mathbf{P}^{(l)}(\omega)$ is a $k \times k$ matrix whose (n, m)th element is $P_{nm}^{(l)}(\omega)$and $\boldsymbol{\nu}$ is a $k \times k$ matrix whose (n, m)th element is the received noise at the mth transducer when the nth transducer is transmitting the probing signal.

4.2 Algorithms

In this section, we aim to image the second layer of the material under test using the data model, we developed in Subsection 4.1.1. To image the region of interest,

we need to assign a relative intensity to each pixel point in the image. For this purpose, the region of interest is covered with a sufficiently fine grid. Then, we apply some existing imaging algorithms including the conventional beamforming, MUSIC, and Capon for imaging the second layer of a multi-layer medium using our proposed array spatial signature. MUSIC and Capon algorithms originally have been developed for a homogeneous medium where the sound velocity is uniform in the medium. The conventional beamforming algorithm has been applied for imaging a multi-layer medium in synthetic apertures focusing test scenario using the concept of RMS velocity known as multi layer delay and sum MDAS method. However, in this section, we aim to image a multi-layer medium when using a uniform linear array of transducers.

4.2.1 Conventional Beamforming

In this subsection, we use the conventional beamforming technique to image the second layer of a two-layer medium. To do so, we need to estimate the backscattering strength of each point in the ROI [29]. Assuming the narrow-band model for the array measurements developed in the previous section, we use the conventional beamforming method to estimate the backscattering strength of a hypothetical point scatterer, located at (x, y) in the second layer of the test sample, as

$$I_{CB}(\omega; x, y) = \left|\text{tr}\{\mathbf{P}(\omega)\mathbf{U}^H(\omega; x, y)\phi^*(\omega)\}\right|^2 \tag{4.2.1}$$

where $I_{CB}(\omega; x, y)$ is the conventional beamforming-based estimate of the backscattering strength of a hypothetical point scatterer, located at (x, y) in the second layer, at frequency ω, $(\cdot)^H$ is the Hermitian operator, $(\cdot)^*$ is the conjugate operator, $\text{tr}\{\cdot\}$ is the trace of a matrix, and $\mathbf{U}(\omega; x, y)$ is defined in (4.1.15) as the array spatial signature matrix for a hypothetical point scatterer, located at (x, y). The idea behind the

conventional beamforming algorithm in (4.2.1) is to compensate the phase delay of the signal corresponding to the transmission path (the path between the transmitter and scatterer point) and the reception path (the path between the scatterer point and the receiver). Note that by using $\mathbf{U}(\omega; x, y)$ in (4.2.1), we are considering all possible wave propagation paths between the transmitters and the receivers using a distributed source modeling for the inter-layer interface.

4.2.2 Capon Algorithm

In this subsection, we use our new array spatial signature vector introduced in (4.1.16), in conjunction with the Capon algorithm for imaging the second layer of a two-layer material under test. The Capon method exploits the second order statistics of the received signals, i.e., it relies on the covariance matrix of the array received signals [29]. Using the narrow-band model for the array spatial signature in (4.1.17), we introduce the Capon-based estimate of the backscattering strength of a hypothetical point scatterer, located at (x, y), as

$$I_C(\omega; x, y) = \frac{1}{\mathbf{v}^H(\omega; x, y)\mathbf{R}^{-1}(\omega)\mathbf{v}(\omega; x, y)} \tag{4.2.2}$$

where $I_C(\omega; x, y)$ is the Capon-based estimate of the backscattering strength of a hypothetical point scatterer, located at (x, y) in the second layer, at frequency ω, $\mathbf{v}(\omega; x, y)$ is the array spatial signature vector, at frequency ω, corresponding to the receiving transducers defined in (4.1.17), and $\mathbf{R}(\omega)$ is the sample covariance matrix of the array signal measurements. In the absence of true covariance matrix, we use the sample covariance matrix defined as

$$\mathbf{R}(\omega) = \frac{1}{k} \sum_{n=1}^{k} \mathbf{p}_n^T(\omega)\ \mathbf{p}_n^*(\omega). \tag{4.2.3}$$

Here, $\mathbf{p}_n(\omega)$ is the n-th row of the received signal matrix $\mathbf{P}(\omega)$. Indeed, $\mathbf{p}_n(\omega)$ is the array received signal vector corresponding to the transmission of the n-th transducer. In fact, in (3.1.13), we consider each row of the full matrix data $\mathbf{P}(\omega)$, as one independent snapshot for determining the sample covariance matrix required for the Capon algorithm. Note that he number of snapshots is limited to the number of array elements. Also, we implicitly assume that the scatterers are sources that emit the sound wave at the same time instant [47]. Therefore, in (4.2.2), we use $\mathbf{v}(\omega; x, y)$ which is a vector containing the spatial signatures of the receiving transducers for a hypothetical point scatterer, located at (x, y) inside the second layer. Moreover, by using $\mathbf{v}(\omega; x, y)$ in (4.2.2), we are taking into account the affect of the sound wave refraction from all the points on the inter-layer interface between the two layers.

4.2.3 MUSIC Method

The MUSIC method is an eigen-decomposition approach for source localization [27]. Similar to the Capon algorithm, this method relies on the sample covariance matrix of the array signals measurement. Assuming the narrow-band model for the array spatial signature given in (4.1.17), we introduce the MUSIC-based estimate of the backscattering strength of a hypothetical point scatterer, located at (x, y), as

$$I_M(\omega; x, y) = \frac{1}{\mathbf{v}^H(\omega; x, y)\mathbf{E}_n(\omega)\mathbf{E}_n^H(\omega)\mathbf{v}(\omega; x, y)} \tag{4.2.4}$$

where $I_M(\omega; x, y)$ is the MUSIC-based estimate of the backscattering strength of a hypothetical point scatterer, located at (x, y), at frequency ω, $\mathbf{E}_n(\omega)$ is a $k \times (k - n_s)$ matrix collecting all the noise subspace eigenvectors of the sample covariance matrix $\mathbf{R}(\omega)$ which is defined in (3.1.13), and n_s is the signal subspace dimension. Note

that, similar to the Capon algorithm, we implicitly assume that the scatterers are sources that emit the sound wave at the same time instant [47]. Therefore, in (4.2.2), we use $\mathbf{v}(\omega; x, y)$ which is a vector containing the spatial signatures of the receiving transducers for a hypothetical point scatterer, located at (x, y) inside the second layer. Moreover, in order to apply the MUSIC algorithm, the dimension of the signal subspace n_s, is needed. In case of a spatially distributed scatterer, the signal subspace can occupy the whole observation space, rendering the noise subspace degenerate. Therefore, we use the notion of *effective signal subspace dimension* for n_s, and it is defined as the number of significant eigenvalues of the sample covariance matrix. Thus, we consider n_s as an integer parameter which has to be chosen by user, in order to increase the quality of the image.

4.2.4 Wide-band Consideration

In ultrasonic tests, the probing signal is wide-band. In the previous section, we presented our data model for a narrow-band probing signal. This data model can be used for a wide-band scenario as explained in the sequence. Using Fourier transform of the array signal measurements, we can decompose the wide-band array signals into narrow-band signals, and apply any of the three methods, proposed in the previous subsections, to estimate the backscattering strength of the points inside the second layer, at each frequency in the signal band-width. We can then, average the so-obtained narrow-band estimates, over different frequencies. Hence, we introduce the wide-band estimate of the backscattering strength of a point scatterer located at (x, y), using the conventional beamforming technique, the Capon algorithm, and the

MUSIC method, respectively as,

$$\mathcal{I}_{CB}(x,y) = \sum_{\omega_i \in \Omega} I_{CB}(\omega_i; x, y) \tag{4.2.5}$$

$$\mathcal{I}_{C}(x,y) = \sum_{\omega_i \in \Omega} I_{C}(\omega_i; x, y) \tag{4.2.6}$$

$$\mathcal{I}_{M}(x,y) = \sum_{\omega_i \in \Omega} I_{M}(\omega_i; x, y). \tag{4.2.7}$$

Here Ω is a set of all frequencies in the signal band-width, $\mathcal{I}_{CB}(x,y)$, $\mathcal{I}_{C}(x,y)$, and $\mathcal{I}_{M}(x,y)$ are estimates of the backscattering strength of a hypothetical point scatterer, located at (x,y), using all frequencies in the band-width, corresponding to the conventional beamforming technique, the Capon algorithm, and the MUSIC method, respectively. To obtain an image of the ROI, we introduce $\mathcal{I}_{CB}(x,y)$, $\mathcal{I}_{C}(x,y)$, and $\mathcal{I}_{M}(x,y)$ as the relative intensity of a point, located at (x,y) in the ROI, corresponding to the conventional beamforming-based, Capon-based, and MUSIC-based imaging techniques, respectively.

4.2.5 Multi-layer

In (4.1.22), the computational complexity for imaging of the l-th layer increases exponentially as the number of layers increases. To calculate the $u_n^{(l)}(\omega; x, y)$ for any point inside the l-th layer using $u_n^{(l-1)}(\omega; x_{(l-1)}, y_{(l-1)})$, we can use the following recursive equation:

$$u_n^{(l)}(\omega; x, y) \triangleq \int_{y_1 = C_{l-1}(x_{l-1})} u_n^{(l-1)}(\omega; x_{(l-1)}, y_{(l-1)}) g_{(l)}(\omega; x_{l-1} y_{l-1}, x, y) dx_{l-1} \tag{4.2.8}$$

Having $u_n^{(l-1)}(\omega; x_{(l-1)}, y_{(l-1)})$ for the points located on the interface of the $(l-1)$-th and the lth layers, during the processing for the imaging of the $(l-1)$th layer, we need to calculate the one dimensional integration in (4.2.8) for the points in the l-th

layer in order to image the l-th layer. Therefore, starting imaging process from the second layer, for the lower layers, the computational complexity remains the same.

4.3 Experimental Results

In this section, we aim to evaluate the performance of our data model in imaging the second layer of a two-layer medium. To do so, we conducted an immersion ultrasonic test where a metallic test sample and a uniform linear array of ultrasonic transducers were immersed in water. The sound wave propagates in water with speed $c_1 = 1500$ m/s, while the sound propagation speed in steel is $c_2 = 6300$ m/s. The test configuration is depicted in Fig. 4.3, where the test sample is a steel block with several side-drilled holes. The distance between the array probe and the test sample is $d_0 = 9.5$ mm. We used a uniform linear array of $k = 64$ ultrasonic transducers with an element pitch[1] of 0.60 mm. The transducers have a rectangular shape. The beam-pattern of the n-th transducer, located at $(\tilde{x}_n, \tilde{y}_n)$, at a hypothetical point located at (x_1, y_1) on the interface between two layers is given by

$$B_n(\omega; x_1, y_1) = \text{sinc}\left(\frac{l\ \omega\ |\tilde{x}_n - x_1|}{2\pi\ c_1\ d(\tilde{x}_n, \tilde{y}_n, x_1, y_1)}\right) \tag{4.3.1}$$

where l is the width of the transducers along the x-axis and is chosen as $l = 0.6$ mm. The ultrasonic array probe is parallel to the x-axis and the upper surface of the test sample. The first transducer is assumed to be located at $x = 0$ mm and $y = -9.5$ mm. Each transducer is stimulated with the same probing signal one after the other, while all of the transducers (including the one transmitting) receive the wave backscattered from the solid test sample. We allow enough time between firing of subsequence

[1]The element pitch is the distance between the center of two adjacent ultrasonic transducers.

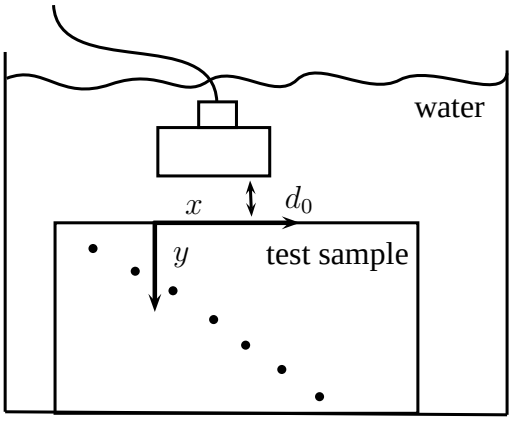

Figure 4.3: Immersion test configuration.

transducers, to avoid undesired interferences between the received signals. All the 4096 received signals are sampled, quantized, saved in a digital computer for post-processing. A time-domain sample received signal is shown in Fig. 4.4. The probing signal is a wide-band signal. The center frequency of the probing signal is 5 MHz. We have used Fourier transform to decompose the received signals into narrow-band components. We choose the efficient band-width to be 5MHz which is spread over 200 frequency bins. Then, we have used (4.2.5), (4.2.6), and (4.2.7) to image the ROI using the conventional beamforming technique, the MUSIC method, and the Capon algorithm, respectively. For all images, the ROI is the area between the lines $y = 5$ mm, $y = 40$ mm, $x = 0$ mm, and $x = 40$ mm, and includes three holes. All the images have been normalized to their maximum values (brightest pixel in the image).

To apply the conventional beamforming imaging technique of (4.2.5), we need to use (4.1.15) to calculate the array spatial signature matrix $\mathbf{U}(\omega; x, y)$ for all points in the ROI, and also to obtain the $\phi(\omega)$. To obtain $\phi(\omega)$, we extracted its time-domain representation, $\varphi(t)$, from the signal backscattered by the back-wall of the test block.

To do so, we compute the round travel time of the normal sound beam from the transducer array to the backwall of the test sample and back to the transducer array. Then, we have chosen 150 samples which are received after this time in the signal $P_{32,32}(t)$. This back-wall reflected signal is shown in Fig. 4.5. Then, $\phi(\omega)$ is produced using Fourier transform of $\varphi(t)$. To apply the Capon algorithm of (4.2.6) and the MUSIC method of (4.2.7), we use the receiving transducers array spatial signature $\mathbf{v}(\omega; x, y)$ in (4.1.17) for all points in the region of interest.

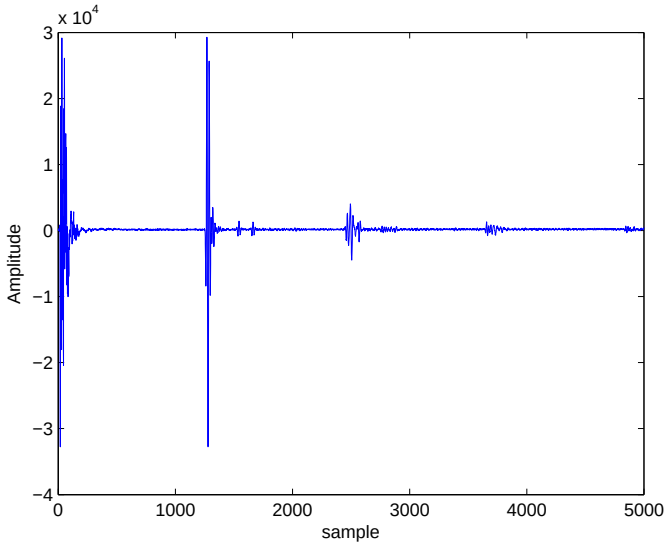

Figure 4.4: Sample received signal.

To show the accuracy of our proposed data model, we compare the performance of the three aforementioned imaging algorithms, when our proposed array signature is used in these three algorithms, with the case when the array spatial signature is modeled based on the root mean squared (RMS) velocity method of [32] and [33]. In the RMS velocity based method, the sound velocity is approximated using a weighted

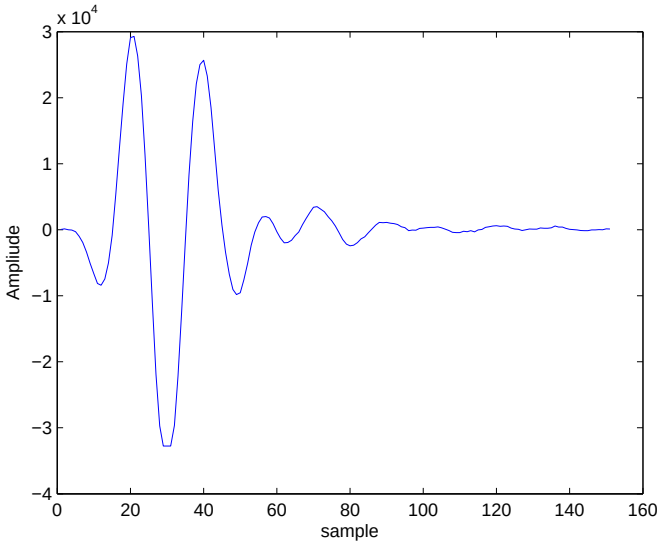

Figure 4.5: Back-wall reflection signal.

average of root mean squared of sound velocity in all the layers. The weights are calculated using the travel time of the normal sound beam in each layer [32]. The RMS velocity method has been used to modify the SAFT technique for immersion ultrasonic imaging in [35]. We now explain how we can apply this method in the three aforementioned algorithms, when an array of transducers is used. Using the so-called RMS velocity, the array spatial signature matrix for a point scatterer located at (x, y) in the second layer, is provided as

$$\mathbf{U}_R(\omega; x, y) \triangleq \mathbf{u}_R(\omega; x, y)\ \mathbf{u}_R^T(\omega; x, y) \tag{4.3.2}$$

where

$$u_R(\omega; x, y) \triangleq [a(\tilde{x}_1, \tilde{y}_1, x, y)\ e^{-j\omega\tau_R(\tilde{x}_1, \tilde{y}_1, x, y)}\ ...\ a(\tilde{x}_n, \tilde{y}_n, x, y)\ e^{-j\omega\tau_R(\tilde{x}_n, \tilde{y}_n, x, y)}]. \tag{4.3.3}$$

Here, the following definition is used

$$\tau_R(\tilde{x}_n, \tilde{y}_n, x, y) \triangleq \frac{d(\tilde{x}_n, \tilde{y}_n, x, y)}{c_R} \tag{4.3.4}$$

where c_R is the so-called RMS velocity which is obtained using the method of [32]. Therefore the narrow-band estimate of the scattering coefficient of a point scatterer located at (x, y) in the second layer, based on RMS velocity method, using the conventional beamforming technique, the Capon algorithm, and the MUSIC method can be written respectively as

$$I^R_{CB}(\omega; x, y) = \left|\mathrm{tr}\{\mathbf{P}(\omega)\mathbf{U}^H_R(\omega; x, y)\phi^*(\omega)\}\right|^2 \tag{4.3.5}$$

$$I^R_C(\omega; x, y) = \frac{1}{\mathbf{u}^H_R(\omega; x, y)\mathbf{R}^{-1}(\omega)\mathbf{u}_R(\omega; x, y)} \tag{4.3.6}$$

$$I^R_M(\omega; x, y) = \frac{1}{\mathbf{u}^H_R(\omega; x, y)\mathbf{E}_n(\omega)\mathbf{E}^H_n(\omega)\mathbf{u}_R(\omega; x, y)}\,. \tag{4.3.7}$$

Then, the RMS-velocity-based image corresponding to the conventional beamforming technique, the Capon algorithm, and the MUSIC method, are introduced respectively as

$$\mathcal{I}^R_{CB}(x, y) = \sum_{\omega_i \in \Omega} I^R_{CB}(\omega_i; x, y) \tag{4.3.8}$$

$$\mathcal{I}^R_C(x, y) = \sum_{\omega_i \in \Omega} I^R_C(\omega_i; x, y) \tag{4.3.9}$$

$$\mathcal{I}^R_M(x, y) = \sum_{\omega_i \in \Omega} I^R_M(\omega_i; x, y). \tag{4.3.10}$$

Figs. 4.6 show the image of the test sample obtained using the conventional beamforming technique of (4.2.5), and Fig. 4.8 presents the image when the conventional beamforming technique of (4.3.8) is used. We have also shown the corresponding images in three-dimensional plots in Figs. 4.7 and 4.9. Comparing Figs. 4.6 and 4.7 with Figs. 4.8 and 4.9, respectively, we observe that the conventional beamforming image of (4.2.5) has prominent peaks. Also, in the RMS velocity based image the peak corresponding to the middle hole is relatively smaller than the corresponding peak of the image obtained using (4.2.5). To compare our proposed model for array

spatial signature with the one using the RMS velocity method in terms of root mean squared error (RMSE), we provide the RMSE plot versus the SNR. To do so, we have added a zero-mean Gaussian noise with different powers, corresponding to different values of SNR, to the raw data. Note that here the SNR is defined as the power of the additive noise to the power of the backscattered signal at the receiving transducer. We reconstruct the image using the data contaminated with additive noise and calculate the RMSE of the location of the peak which corresponds to the hole located at the middle of the ROI. The RMSE is calculated based on the assumption that the true the location of the peak in the image is the one which is obtained from the original data (without additive noise). Fig. 4.18 shows the RMSEs for the hole location estimate obtained using the conventional beamforming technique of (4.2.5) and that obtained using the RMS velocity based method of (4.3.8). This figure clearly shows the superiority of the proposed array spatial signature model compared to the RMS velocity based method, when these models are usedin conventional beamforming algorithm.

Fig. 4.10 shows the image of the test sample obtained using the Capon algorithm of (4.2.6). Fig. 4.12 shows the image of the test sample obtained Capon algorithm of (4.3.9). We have also shown the corresponding images in three-dimensional plots in Figs. 4.11 and 4.13. As can be seen from these figures, the Capon-based image, which rely on the RMS velocity method, i.e., Figs. 4.12 and 4.13 have detected the three holes, however the brightness of the left and the right holes are significantly lower compared to the same brightness of the corresponding holes in Figs. 4.10 and 4.11 which are obtained using our proposed array spatial signature. Fig. 4.19 compares the RMSE of the location estimate for the hole, located in the middle of the ROI, using

the images obtained from (4.2.6) and (4.3.9). This figure clearly shows the superiority of the proposed array spatial signature model compared to the RMS velocity based method, when these models are used in the Capon based imaging approach. Fig. 4.14 shows the image of the test sample obtained using the MUSIC based imaging method of (4.2.7). Fig. 4.16 shows the image of the test sample obtained by using the MUSIC based imaging technique of (4.3.10). We have also shown the corresponding images in three-dimensional plots in Figs. 4.15 and 4.17. Fig. 4.20 compares the RMSE of the location of the hole, located in the middle of the ROI, for the two aforementioned MUSIC based methods. These images show that the performance of the MUSIC method is superior when this method relies on our proposed model for the array spatial signature as compared to the case when the RMS velocity method is used.

We have compared the performance of our proposed array spatial signature model in conjunction with three algorithms with the the corresponding cases, when the RMS velocity concept is used in these algorithms. Theses images clearly show that the performance of the three algorithms when they rely on our model for the array spatial signature is superior to the performance of these algorithms when they are using the RMS velocity method. The RMSE plot for all the three algorithms also confirm the accuracy of our proposed model for the array spatial signature.

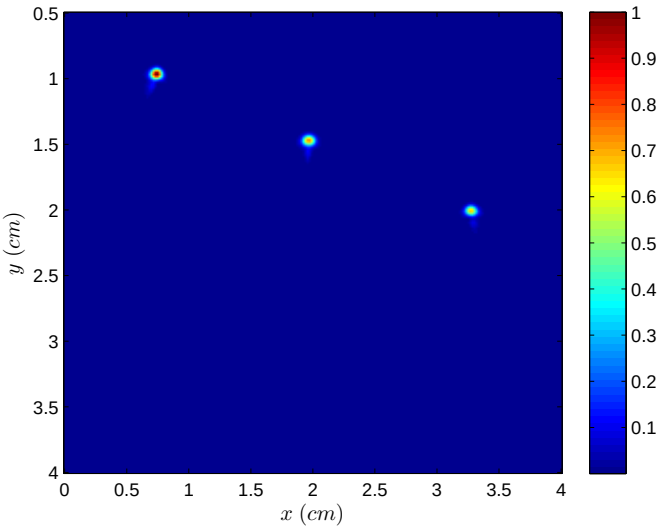

Figure 4.6: Conventional beamforming image of (4.2.1).

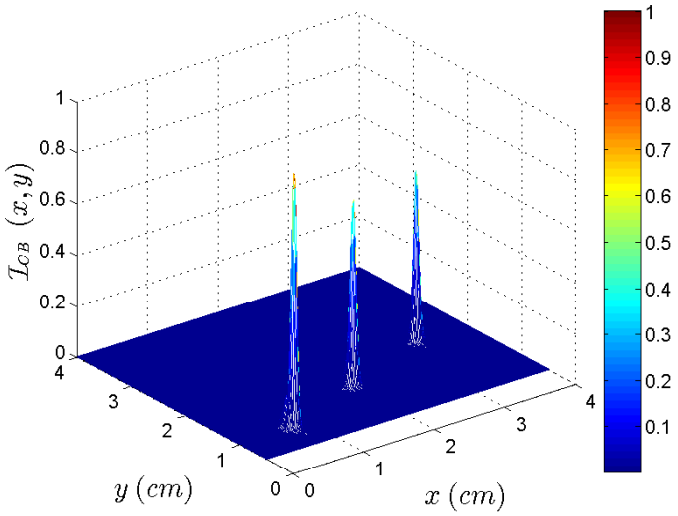

Figure 4.7: Three dimensional plot of (4.2.1).

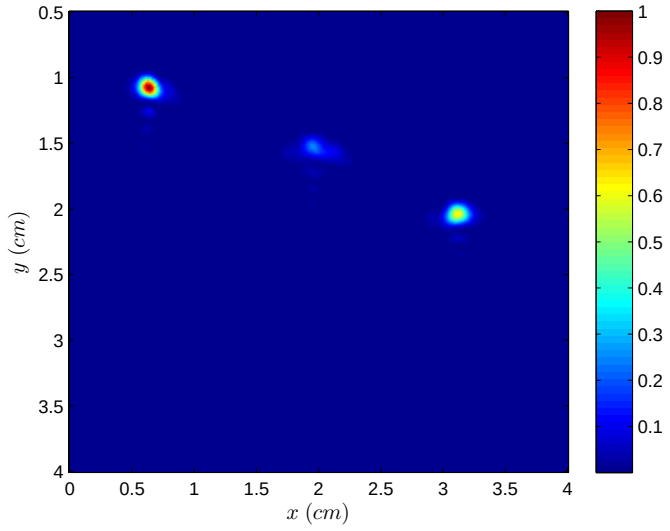

Figure 4.8: Conventional beamforming image based on RMS velocity concept.

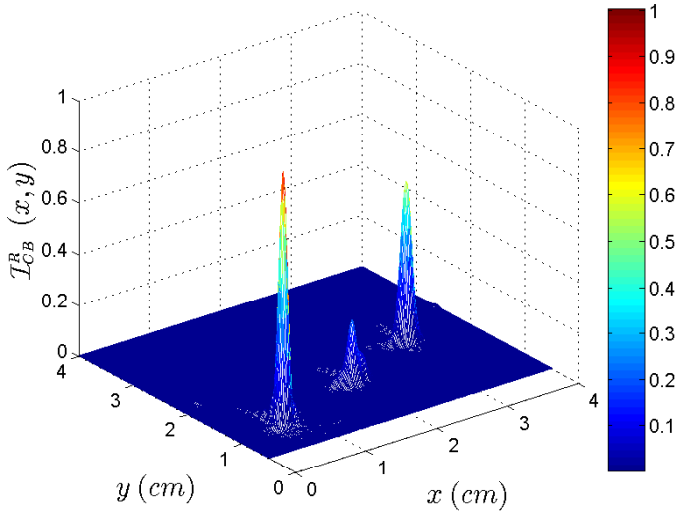

Figure 4.9: Three dimensional plot for conventional beamforming based on RMS velocity concept.

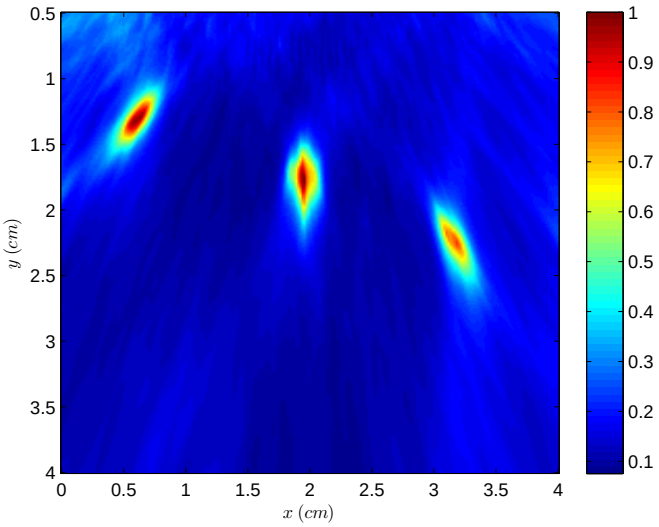

Figure 4.10: Capon image of (4.2.2).

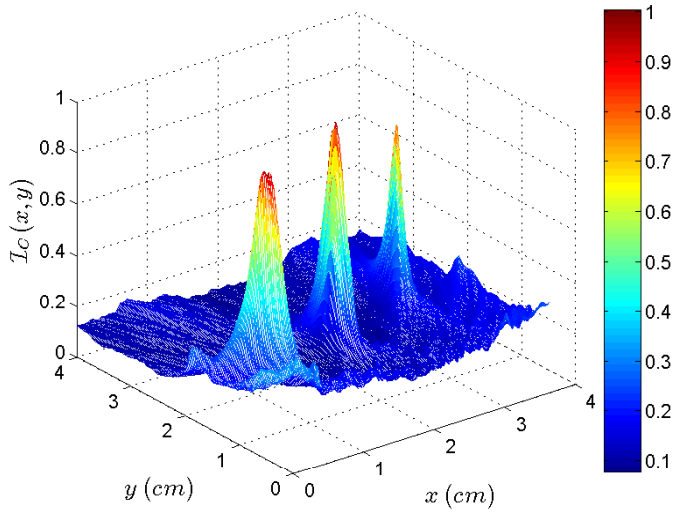

Figure 4.11: Three dimensional plot of (4.2.2).

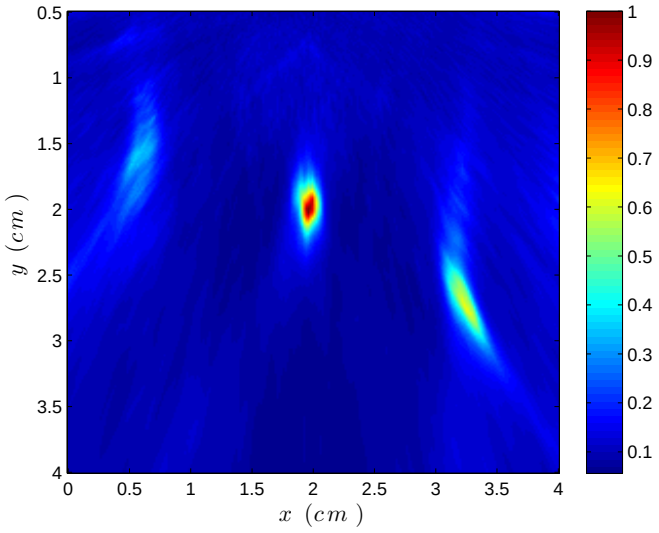

Figure 4.12: Capon image based on RMS velocity concept.

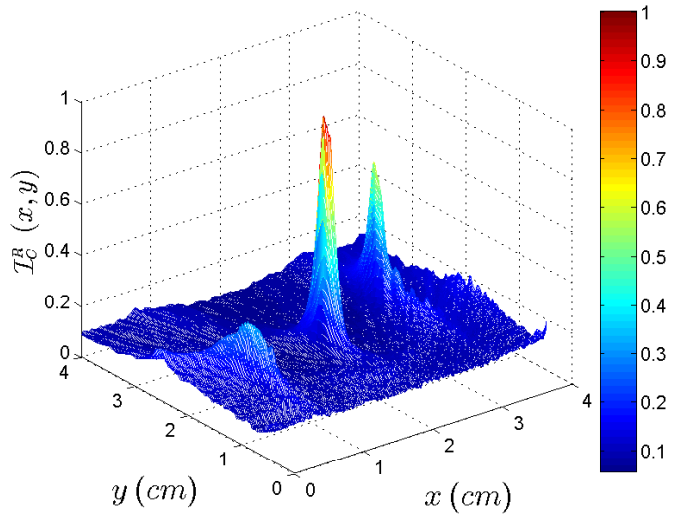

Figure 4.13: Three dimensional plot for the Capon technique based on RMS velocity concept.

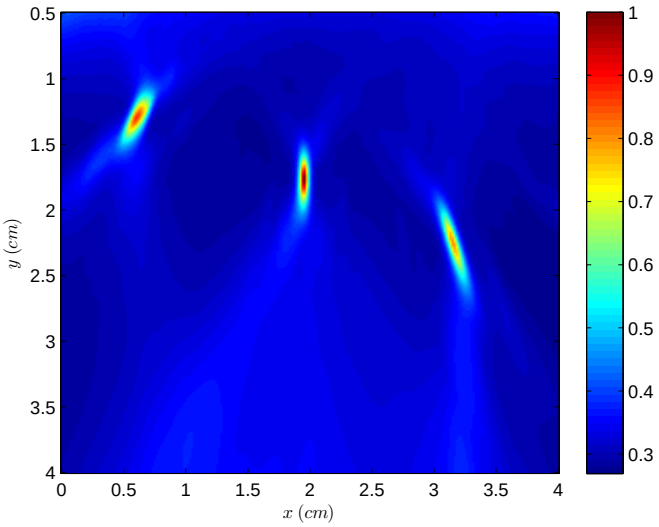

Figure 4.14: MUSIC image of (4.2.4).

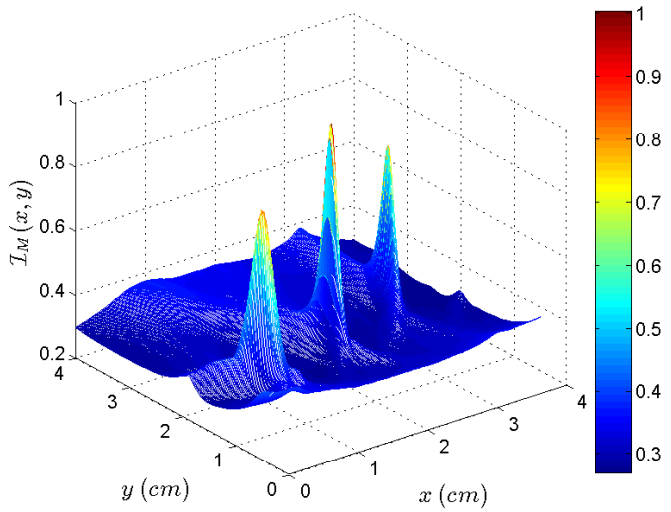

Figure 4.15: Three dimensional plot of (4.2.4).

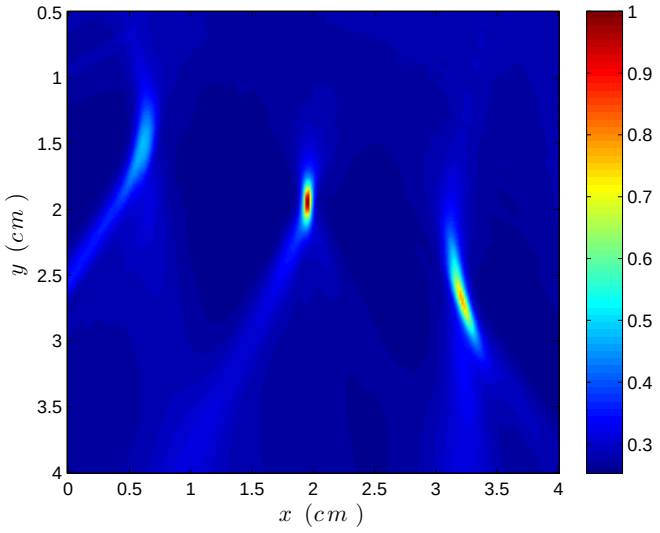

Figure 4.16: MUSIC image based on RMS velocity concept.

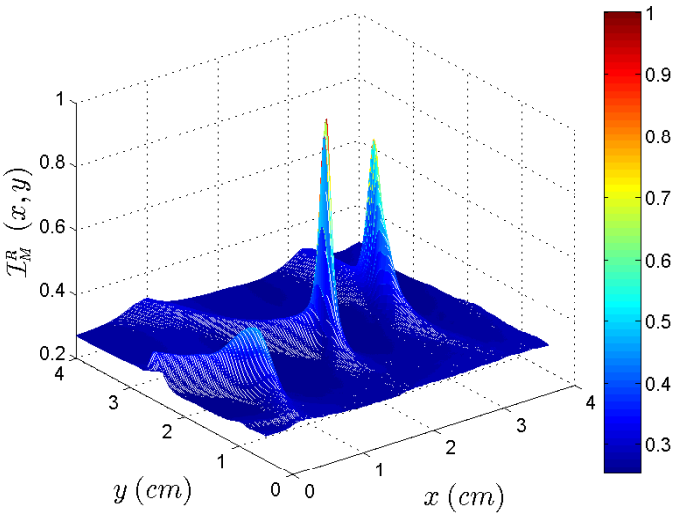

Figure 4.17: Three dimensional plot for the MUSIC technique based on RMS velocity concept.

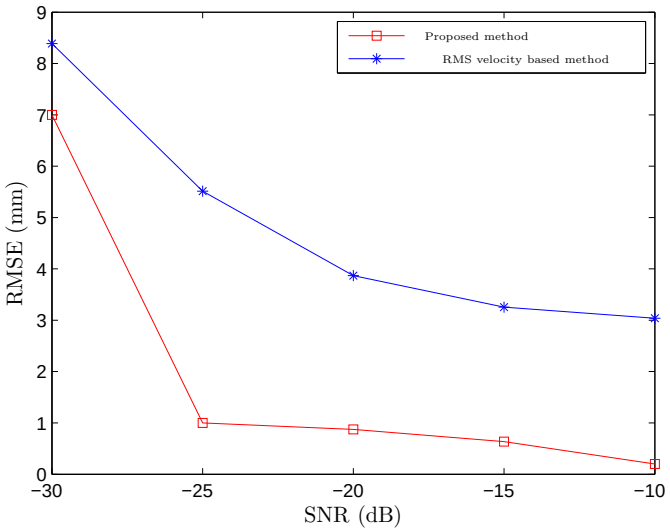

Figure 4.18: The RMSE for conventional beamforming method.

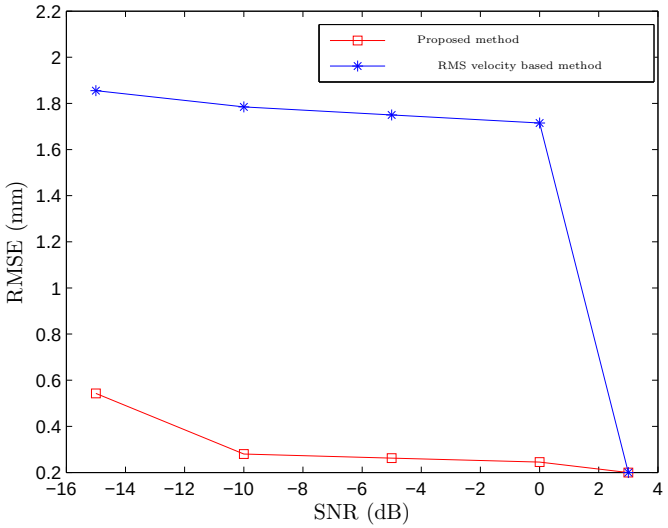

Figure 4.19: The RMSE for Capon method.

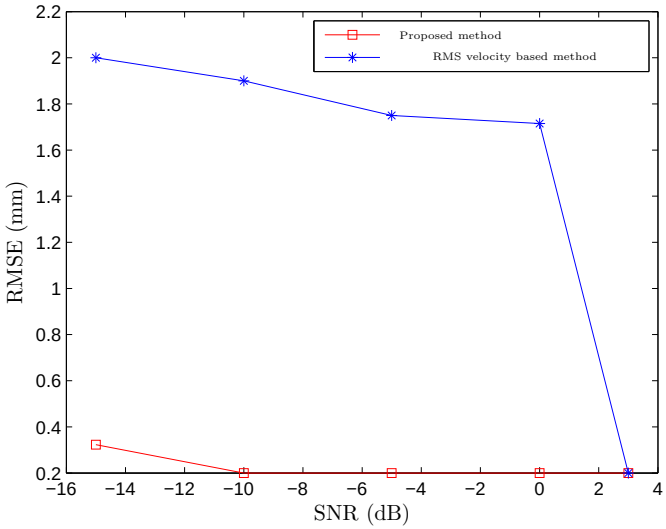

Figure 4.20: The RMSE for MUSIC method.

4.4 Conclusions

In this chapter, in order to image a two-layer medium, we modeled the interfaces between the two layers as a spatially distributed source, which consists of infinite number of point sources. Based on this type of modeling, we presented a new model for array spatial signature for all the points inside a two-layer medium, and used this new model in imaging techniques including the conventional beamforming technique, the MUSIC method, and the Capon algorithm, in order to image a two-layer medium. These algorithms traditionally are applied for a homogeneous medium where the sound velocity is constant in the material under test, however in a two-layer medium the sound velocity is different in each layer. For examining the accuracy of our proposed model with experimental data, we used the data for an immersion ultrasonic test of a steel block and imaged the steel block as the second layer of a two-layer medium. We also compared the accuracy of our model for array spatial signature

with that of the RMS velocity based method.

Our simulation results and experimental tests show that using our proposed model in conjunction with the conventional beamforming imaging technique, as well as along with the MUSIC and Capon imaging methods results in a superior performance compared to the case when the RMS velocity based method is used in these imaging techniques. However, The computational complexity and therefore the execution time is high for an online imaging process. In the next chapter, we propose a Fourier-based imaging algorithm which has a lower computational complexity and it can be used in an online imaging process.

Chapter 5

A Fourier-based imaging algorithm for Second layer of a two-layer medium

In the previous chapter, based on the Huygens principle, we have modeled the interfaces between layers of a two-layer medium as secondary spatially distributed sources consisting of infinite number of point sources. Then, we use this model to develop a new array spatial signature for all points inside a two-layer medium. This new array spatial signature can be used in imaging techniques including the conventional beamforming technique, the MUSIC method, and the Capon algorithm in order to image two-layer materials.

All three algorithms are able to image the region of interest precisely based on our proposed array spatial signature, however, the execution time is still high for online image processing. In this chapter, we also model the interface between two layers as spatially distributed source which refract the probing sound wave into the lower layers. However, herein the goal is to propose a Fourier-based imaging algorithm for the second layer of the material under test. In this algorithm, the execution time is

considerably reduced comparing to the aforementioned three algorithms.

5.1 Data Model

We consider a two-layer solid object which is under ultrasonic test using a one-dimensional uniform linear array of M ultrasonic transducers. We assume that each layer is a homogeneous medium with a constant sound velocity; however, the sound velocity in each layer is different from that in the other one. Each transducer transmits a sound wave and all the other transducers (including the one transmitting) receive the backscattered sound wave from the test sample. The M^2 time domain received signals is sampled in time and stored in a $N \times M \times M$ tensor where N is the number of time samples. The goal is to develop a data model for the backscattered signals with the aim to use it for imaging the second layer of the material under test. We assume that the upper surface of the test sample, the interface between the layers, and the back wall of the test sample are parallel planes (i.e., multi-layer material with parallel interfaces). The center of the two-dimensional Cartesian coordinate system is assumed to be in the middle of the second layer of the material under test, as shown in Fig. 5.1. The width of the first layer in y direction is d_1 and the width of the second layer in y direction is $2d_2$. We present our data model in a two-dimensional coordinate system, assuming that the ultrasonic transducers, the test sample, and the defects are infinitely long in the third dimension. This model can easily be extended for three-dimensional volumetric imaging scheme where a two-dimensional uniform array is employed. All the transducers in the array are assumed to be identical and the beam pattern gain of the n-th transducer located at $(u, -d_1 - d_2)$, at frequency

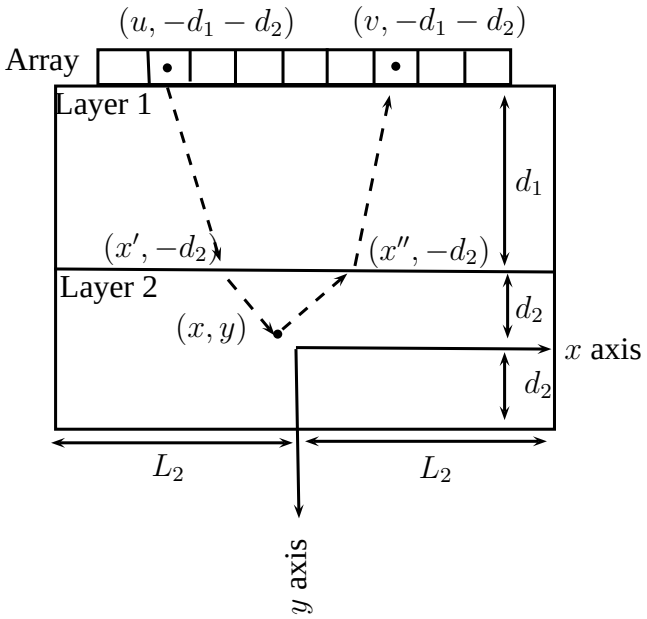

Figure 5.1: A hypothetical point scatterer inside second layer of a two-layer medium.

ω toward the point located at (x, y) is is denoted as $B(\omega; u, -d_1 - d_2; x, y)$.

We model the interface between the two layers as a spatially distributed source. Assuming a two-dimensional model, this interface can be modeled as a line consisting of infinite number of point sources [48]. At each point on the interface, the propagating sound wave is refracted into the second layer, therefore, each point on the interface acts as a point source for all the points inside the second layer. Let us assume that there is a point scatterer located at (x, y) inside the second layer of the test sample, and the transducer located at coordinate $(u, -d_1 - d_2)$ is firing the probing sound wave. This sound wave is refracted by all the points on the interface between the two layers into the second layer. Then, any point scatterer scatters the sound wave back towards the interface. This backscattered sound wave is refracted into the first layer

by all the points on the interface, and the transducer array measures the superposition of all these refracted signals. Therefore, at frequency ω, the backscattered signal received by the transducer located at coordinate $(v, -d_1 - d_2)$ due to the scattering of a point scatterer, located at (x, y) in the second layer is denoted by $p_{x,y}(\omega; u, v)$ and it can be written as [20]

$$p_{x,y}(\omega; u, v) = \phi(\omega) f_{12}\ f_{21} \iint_{-\infty}^{+\infty} B(\omega; u, -d_1 - d_2; x', -d_2) B(\omega; v, -d_1 - d_2; x'', -d_2,)$$

$$s(x, y)\ g_f(\omega; x' - u, d_1) g_s(\omega; x - x', y + d_2) g_s(\omega; x - x'', y + d_2) g_f(\omega; x'' - v, d_1) dx' dx''. \tag{5.1.1}$$

Here, $\phi(\omega)$ is the probing signal at frequency ω, f_{12} is the transmission coefficient from Layer 1 into Layer 2, f_{21} is the transmission coefficient from Layer 2 into Layer 1, $s(x, y)$ is the *real-valued* scattering coefficient of a hypothetical point scatterer located at (x, y) inside the second layer, $B(\omega; u, -d_1 - d_2; x', -d_2)$ is the beam pattern gain of the source transducer, located at $(u, -d_1 - d_2)$, towards a point located at $(x', -d_2)$ on the interface at frequency ω, and $B(\omega; v, -d_1 - d_2; x'', -d_2,)$ is the beam pattern gain of the receiving transducer, located at $(v, -d_1 - d_2)$, towards a point located at $(x'', -d_2)$ on the interface at frequency ω. Also, $g_f(\omega; x' - u, d_1)$ is the Green function corresponding to the propagation of sound wave in the first layer from the source transducer, located at $(u, -d_1 - d_2)$, to a point located at $(x', -d_2)$ on the interface at frequency ω, $g_s(\omega; x - x', y + d_2)$ is the Green function corresponding to the propagation of sound wave in the second layer from a point located at $(x', -d_2)$ on the interface to a hypothetical point scatterer located at (x, y) inside the second layer at frequency ω, $g_s(\omega; x - x'', y + d_2)$ is the Green function corresponding to the propagation of sound wave in the second layer from a hypothetical point scatterer located at (x, y) inside the second layer to a point located at $(x'', -d_2)$ on the interface at frequency

ω, and $g_f(\omega; x'' - v, d_1)$ is the Green function corresponding to the propagation of sound wave in the first layer from a point located at $(x', -d_2)$ on the interface to the receiving transducer located at $(v, -d_1 - d_2)$ at frequency ω. The Green functions in the first and second layers can be written respectively as [20]

$$g_f(\omega; x, y) = \frac{-j}{4\pi} \int_{-\infty}^{+\infty} \frac{\exp\left(-jk_x x - jy\sqrt{k_f^2 - k_x^2}\right)}{\sqrt{k_f^2 - k_x^2}} dk_x \tag{5.1.2}$$

$$g_s(\omega; x, y) = \frac{-j}{4\pi} \int_{-\infty}^{+\infty} \frac{\exp\left(-jk_x x - jy\sqrt{k_s^2 - k_x^2}\right)}{\sqrt{k_s^2 - k_x^2}} dk_x. \tag{5.1.3}$$

Here, $k_f \triangleq \omega/c_f$ and $k_s \triangleq \omega/c_s$ are the wave numbers in Layers 1 and 2, respectively, and c_f and c_s are the corresponding sound velocities in Layers 1 and 2.

Note that the exact value of the transmission coefficient f_{12} depends an the location of the refracting point on the interface and the location of the hypothetical point scatterer. Also, the transmission coefficient f_{21} depends on the location of the refracting point on the interface and the location of the receiving transducer [49]. The exact values of the transmission coefficients f_{12} and f_{21} can be calculated using Huygen's principle as in Chapter 4. However, the computational complexity of the proposed approach in Chapter 4, is high and increases the execution time of the imaging algorithms. To reduce the computational complexity and therefore the execution time, we assume that the transmission coefficients f_{12} and f_{21} are constant values across the interface between the two layers. With this assumption, we aim to propose an imaging algorithm for an online second layer ultrasonic test.

The backscattered signal $p_{x,y}(\omega; u, v)$ in (5.1.1) depends on the probing signal $\phi(\omega)$, and the transducers beam-pattern gains $B(\omega; u, -d_1 - d_2; x', -d_2)$ and $B(\omega; v, -d_1 -$

$d_2; x'', -d_2,)$. We assume that the probing signal is an impulse and that the transducers are omni-directional, i.e,

$$B(\omega; u, -d_1 - d_2; x', -d_2) = 1 \tag{5.1.4}$$

$$B(\omega; v, -d_1 - d_2; x'', -d_2,) = 1 \tag{5.1.5}$$

$$\varphi(t) = \delta(t) \tag{5.1.6}$$

where $\varphi(t)$ is the time domain representation of $\phi(\omega)$. Alternatively, in practice, these effects can be compensated in the preprocessing steps [20]. Therefore, (5.1.1) can be written as

$$p_{x,y}(\omega; u, v) = f_{12}\ f_{21} \iint_{-\infty}^{+\infty} s(x, y)\ g_f(\omega; x' - u, d_1)$$
$$g_s(\omega; x - x', y + d_2) g_s(\omega; x - x'', y + d_2) g_f(\omega; x'' - v, d_1) dx' dx''. \tag{5.1.7}$$

Note that $p_{x,y}(\omega; u, v)$ is the received signal due to the scattering of only one point scatterer inside the second layer. Therefore, the backscattered signal, received at the transducer located at $(v, -d_1 - d_2)$ due to the scattering of all potential point scatterers in the ROI, can be written as

$$p(\omega; u, v) = f_{12}\ f_{21} \iint_{-\infty}^{+\infty} \iint_{-\infty}^{+\infty} s(x, y) g_f(\omega; x' - u, d_1)$$
$$g_s(\omega; x - x', y + d_2) g_s(\omega; x - x'', y + d_2) g_f(\omega; x'' - v, d_1) dx' dx'' dx dy \tag{5.1.8}$$

Note that $s(x, y)$ may be non-zero only for those points in the ROI which reflect the sound wave.

5.2 Fourier Mapping

In this section, we use the data model in (5.1.8) to develop a relationship between the Fourier representation of the measured data $p(\omega; u, v)$ and the the Fourier representation of the image $s(x, y)$, for all the points in the ROI.

Using (5.1.2) and (5.1.3), we can write (5.1.8) as

$$
\begin{aligned}
p(\omega; u, v) = f_{12}\, f_{21} \int_{-\infty}^{+\infty}\!\!\int \int_{-\infty}^{+\infty}\!\!\int s(x, y) \frac{1}{(4\pi)^4} \\
\left(\int_{-\infty}^{+\infty} \frac{\exp\left(-jk_1(x' - u) - jd_1\sqrt{k_f^2 - k_1^2}\right)}{\sqrt{k_f^2 - k_1^2}} dk_1 \right) \times \\
\left(\int_{-\infty}^{+\infty} \frac{\exp\left(-jk_2(x - x') - j(y + d_2)\sqrt{k_s^2 - k_2^2}\right)}{\sqrt{k_s^2 - k_2^2}} dk_2 \right) \times \\
\left(\int_{-\infty}^{+\infty} \frac{\exp\left(-jk_3(x - x'') - j(y + d_2)\sqrt{k_s^2 - k_3^2}\right)}{\sqrt{k_s^2 - k_3^2}} dk_3 \right) \times \\
\left(\int_{-\infty}^{+\infty} \frac{\exp\left(-jk_4(x'' - v) - jd_1\sqrt{k_f^2 - k_4^2}\right)}{\sqrt{k_f^2 - k_4^2}} dk_4 \right) dx' dx'' dx dy. \qquad (5.2.1)
\end{aligned}
$$

We now rewrite (5.2.1) as

$$p(\omega;u,v)=\frac{f_{12}\ f_{21}}{(4\pi)^4}\iint_{-\infty}^{+\infty}\frac{\exp\left(jk_1u+jk_4v-jd_1\left(\sqrt{k_f^2-k_1^2}+\sqrt{k_f^2-k_4^2}\right)\right)}{\sqrt{k_f^2-k_1^2}\sqrt{k_f^2-k_4^2}}$$
$$\left[\iint_{-\infty}^{+\infty}\exp(-jx'k_1-jx''k_4)\left[\iint_{-\infty}^{+\infty}\exp(jx'k_2+jx''k_3)\right.\right.$$
$$\frac{\exp\left(-jd_2\left(\sqrt{k_s^2-k_2^2}+\sqrt{k_s^2-k_3^2}\right)\right)}{\sqrt{k_s^2-k_2^2}\sqrt{k_s^2-k_3^2}}\left[\iint_{-\infty}^{+\infty}s(x,y)\right.$$
$$\left.\left.\left.\exp\left(-jx(k_2+k_3)-jy\left(\sqrt{k_s^2-k_2^2}+\sqrt{k_s^2-k_3^2}\right)\right)dxdy\right]dk_2dk_3\right]dx'dx''\right]dk_1dk_4 \tag{5.2.2}$$

Let $S(k_x,k_y)$ denote the two-dimensional Fourier transform of $s(x,y)$, that is

$$S(k_x,k_y)\triangleq\iint_{-\infty}^{+\infty}s(x,y)\exp\left(-jxk_x-jyk_y\right)dxdy. \tag{5.2.3}$$

Using (5.2.3), we can write

$$\iint_{-\infty}^{+\infty}s(x,y)\exp\left(-jx(k_2+k_3)-jy(\sqrt{k_s^2-k_2^2}+\sqrt{k_s^2-k_3^2})\right)dxdy=$$
$$S\left(k_2+k_3,\sqrt{k_s^2-k_2^2}+\sqrt{k_s^2-k_3^2}\right). \tag{5.2.4}$$

Now, we use (5.2.4) to write (5.2.2) as

$$p(\omega;u,v)=\frac{f_{12}\ f_{21}}{(4\pi)^4}\iint_{-\infty}^{+\infty}\frac{\exp\left(jk_1u+jk_4v-jd_1\left(\sqrt{k_f^2-k_1^2}+\sqrt{k_f^2-k_4^2}\right)\right)}{\sqrt{k_f^2-k_1^2}\sqrt{k_f^2-k_4^2}}$$
$$\left[\iint_{-\infty}^{+\infty}\exp(-jx'k_1-jx''k_4)\left[\iint_{-\infty}^{+\infty}\exp(jx'k_2+jx''k_3)\right.\right.$$
$$\frac{\exp\left(-jd_2\left(\sqrt{k_s^2-k_2^2}+\sqrt{k_s^2-k_3^2}\right)\right)}{\sqrt{k_s^2-k_2^2}\sqrt{k_s^2-k_3^2}}\ S\left(k_2+k_3,\sqrt{k_s^2-k_2^2}+\sqrt{k_s^2-k_3^2}\right)$$
$$\left.\left.dk_2dk_3\right]dx'dx''\right]dk_1dk_4 \tag{5.2.5}$$

To simplify (5.2.5), we define $Z(w, k_2, k_3)$ as

$$Z(\omega; k_2, k_3) \triangleq \frac{\exp\left(-jd_2(\sqrt{k_s^2 - k_2^2} + \sqrt{k_s^2 - k_3^2})\right)}{\sqrt{k_s^2 - k_2^2}\sqrt{k_s^2 - k_3^2}} S\left(k_2 + k_3, \sqrt{k_s^2 - k_2^2} + \sqrt{k_s^2 - k_3^2}\right) \tag{5.2.6}$$

Therefore, we have the following relationships between $Z(w, k_2, k_3)$ and its two-dimensional inverse Fourier transform which is denoted as $z(w, x', x'')$:

$$z(\omega; x', x'') \triangleq \frac{1}{2\pi} \iint_{-\infty}^{+\infty} \exp(jx'k_2 + jx''k_3) Z(\omega; k_2, k_3) dk_2 dk_3 \tag{5.2.7}$$

$$Z(\omega; k_2, k_3) \triangleq \iint_{-\infty}^{+\infty} \exp(-jx'k_2 - jx''k_3) z(\omega, x', x'') dx' dx''. \tag{5.2.8}$$

Using (5.2.6), we can write (5.2.5) as

$$p(\omega; u, v) = \frac{f_{12}\ f_{21}}{(4\pi)^4} \iint_{-\infty}^{+\infty} \frac{\exp\left(jk_1u + jk_4v - jd_1\left(\sqrt{k_f^2 - k_1^2} + \sqrt{k_f^2 - k_4^2}\right)\right)}{\sqrt{k_f^2 - k_1^2}\sqrt{k_f^2 - k_4^2}}$$
$$\left[\iint_{-\infty}^{+\infty} \exp(-jx'k_1 - jx''k_4) \left[\iint_{-\infty}^{+\infty} \exp(jx'k_2 + jx''k_3) Z(\omega; k_2, k_3) dk_2 dk_3\right]\right.$$
$$\left. dx' dx''\right] dk_1 dk_4. \tag{5.2.9}$$

Then using (5.2.7), we can write (5.2.9) as

$$p(\omega; u, v) = \frac{f_{12}\ f_{21}}{2(4\pi)^3} \iint_{-\infty}^{+\infty} \frac{\exp\left(jk_1u + jk_4v - jd_1\left(\sqrt{k_f^2 - k_1^2} + \sqrt{k_f^2 - k_4^2}\right)\right)}{\sqrt{k_f^2 - k_1^2}\sqrt{k_f^2 - k_4^2}}$$
$$\left[\iint_{-\infty}^{+\infty} \exp(-jx'k_1 - jx''k_4) z(\omega; x', x'') dx' dx''\right]$$
$$dk_1 dk_4. \tag{5.2.10}$$

Based on the definition in (5.2.8), we can write

$$Z(\omega; k_1, k_4) = \frac{1}{2\pi} \iint_{-\infty}^{+\infty} \exp(-jx'k_1 - jx''k_4) z(\omega, x', x'') dx' dx''. \tag{5.2.11}$$

Therefore, using (5.2.11), we can write (5.2.10) as

$$p(\omega; u, v) = \frac{f_{12}\ f_{21}}{2(4\pi)^3} \iint_{-\infty}^{+\infty} \frac{\exp\left(jk_1u + jk_4v - jd_1\left(\sqrt{k_f^2 - k_1^2} + \sqrt{k_f^2 - k_4^2}\right)\right)}{\sqrt{k_f^2 - k_1^2}\sqrt{k_f^2 - k_4^2}}$$
$$Z(\omega; k_1, k_4) dk_1 dk_4. \tag{5.2.12}$$

Then, seeking the similarity with the definition of inverse Fourier transform, we write (5.2.12) as

$$p(\omega; u, v) = \frac{1}{2\pi} \iint_{-\infty}^{+\infty} \exp(jk_1u + jk_4v) \left(\frac{f_{12}\ f_{21}\ Z(\omega; k_1, k_4)\ \exp\left(-jd_1\left(\sqrt{k_f^2 - k_1^2} + \sqrt{k_f^2 - k_4^2}\right)\right)}{4(4\pi)^2\sqrt{k_f^2 - k_1^2}\sqrt{k_f^2 - k_4^2}} \right) dk_1 dk_4. \tag{5.2.13}$$

We now define $P(\omega; k_1, k_4)$ as the two-dimensional Fourier transform of $p(\omega; u, v)$ as

$$P(\omega; k_1, k_4) \triangleq \frac{1}{2\pi} \iint_{-\infty}^{+\infty} \exp(-jk_1u - jk_4v) p(\omega; u, v) dk_1 dk_4. \tag{5.2.14}$$

Using (5.2.13) and (5.2.14), we can write

$$P(\omega; k_1, k_4) = \frac{f_{12}\ f_{21}\ Z(\omega; k_1, k_4)\ \exp\left(-jd_1\left(\sqrt{k_f^2 - k_1^2} + \sqrt{k_f^2 - k_4^2}\right)\right)}{4(4\pi)^2\sqrt{k_f^2 - k_1^2}\sqrt{k_f^2 - k_4^2}}. \tag{5.2.15}$$

Therefore, $Z(\omega; k_1, k_4)$ can be written as

$$Z(\omega; k_1, k_4) = \frac{4(4\pi)^2\sqrt{k_f^2 - k_1^2}\sqrt{k_f^2 - k_4^2}\ P(\omega; k_1, k_4)}{f_{12}\ f_{21}\ \exp\left(-jd_1\left(\sqrt{k_f^2 - k_1^2} + \sqrt{k_f^2 - k_4^2}\right)\right)}. \tag{5.2.16}$$

Using (5.2.16) and (5.2.6), we can write

$$S\left(k_1+k_4, \sqrt{k_s^2-k_1^2}+\sqrt{k_s^2-k_4^2}\right) = H(\omega; k_1, k_4) \tag{5.2.17}$$

where

$$H(\omega; k_1, k_4) = \frac{P(\omega; k_1, k_4)\sqrt{k_f^2-k_1^2}\sqrt{k_f^2-k_4^2}\ \sqrt{k_s^2-k_1^2}\sqrt{k_s^2-k_4^2}}{\exp\left(-jd_2(\sqrt{k_s^2-k_1^2}+\sqrt{k_s^2-k_4^2})\right)\exp\left(-jd_1\left(\sqrt{k_f^2-k_1^2}+\sqrt{k_f^2-k_4^2}\right)\right)} \tag{5.2.18}$$

In the next section, we show how this data model in (5.2.17) and (5.2.18) can be used to obtain $s(x, y)$ from the $P(\omega; k_1, k_4)$. Note that, in this data model we have ignored noise.

5.3 Imaging Algorithm

In this section, we aim to present an algorithm for imaging the second layer of a two-layer medium using the data model we obtained in the previous section. To do so, we first compute the three-dimensional Fourier transform of the time-domain array received signals denoted by $\tilde{p}(t, u, v)$ to obtain $P(\omega; k_1, k_4)$, where k_1 and k_4 are the spatial frequency associated with the source transducers location, u, and the receiving transducers location, v, respectively.

In the second step, using the following equations

$$k_x = k_1 + k_4 \tag{5.3.1}$$

$$k_y = \sqrt{k_s^2-k_1^2}+\sqrt{k_s^2-k_4^2}, \tag{5.3.2}$$

we can write (5.2.17) as

$$S(k_x, k_y) = H(\omega; k_1, k_4), \tag{5.3.3}$$

which shows how we can obtain $S(k_x, k_y)$ from $H(\omega; k_1, k_4)$. The transformation in (5.3.3) shows how the three-dimensional data $H(\omega; k_1, k_4)$ can be transformed into the two-dimensional Fourier represent $S(k_x, k_y)$ of the image $s(x, y)$. To apply this transformation, we hold k_1 constant and for each constant k_1, we can estimate the $S(k_x, k_y)$. We denote the estimate of the $S(k_x, k_y)$ corresponding to the k_1, as $\hat{S}(k_x, k_y|k_1)$ and it can be written as

$$\hat{S}(k_x, k_y|k_1) = H(\omega; k_1, k_4)|_{\substack{k_4=k_x-k_1 \\ \omega=k_s c_s}} \tag{5.3.4}$$

where we have used the following

$$k_s = \frac{\pm\sqrt{\left(k_y^4 + 2\left(k_1^2 + k_4^2\right)k_y^2 + k_1^4 + k_4^4 - 2k_1^2k_4^2\right)}}{2k_y}. \tag{5.3.5}$$

Indeed, $\hat{S}(k_x, k_y|k_1)$ is an estimate of $S(k_x, k_y)$ corresponding to a given value of k_1. To eliminate the affect of noise on the image, we take average of $\hat{S}(k_x, k_y|k_1)$ over all the values of k_1 as

$$\tilde{S}(k_x, k_y) = \int_{-\infty}^{+\infty} \hat{S}(k_x, k_y|k_1)dk_1 \tag{5.3.6}$$

where $\tilde{S}(k_x, k_y)$ is the average of all estimate values of $S(k_x, k_y)$ over all the values of k_1. As we assumed that $s(x, y)$ is real, the $\tilde{S}(k_x, k_y)$ for the negative values of k_y can be written as

$$\hat{S}(k_x, -k_y) = \hat{S}^*(-k_x, k_y) \qquad k_y > 0 \tag{5.3.7}$$

where $*$ is the conjugate operator. Now, having $S(k_x, k_y)$ for all the values of k_x and k_y, we take two-dimensional inverse Fourier transform of $\hat{S}(k_x, k_y)$ to obtain $\hat{s}(x, y)$ which is introduced as the image of the ROI.

5.4 Simulation and Experimental Results

In this section, we evaluate the accuracy of our proposed data model and the presented imaging algorithm for the second layer of a two-layer medium. As mentioned earlier, one of the applications of two-layer imaging is immersion ultrasonic test. In an immersion ultrasonic test, the ultrasonic transducers and the test sample are immersed in a liquid such as water, thereby coupling the probing sound wave from a transducer to the material under test. We conducted an immersion ultrasonic test using a uniform linear array of ultrasonic transducers. The ultrasonic array is placed in water above a steel test sample. The ultrasonic array probe is parallel to the upper surface of the test sample. The center of the array is assumed to be located at $x = 0$ mm and $y = 27.5$ mm. The test configuration is depicted in Fig 5.1. The distance between the array probe and the test sample is $d_1 = 9.5$ mm which is filled by water. When one of the transducers fires a probing sound wave, the sound wave propagates in two homogeneous materials including water and steel. the goal is to image the steel test sample which acts as the second layer of a two-layer medium.

Each transducer has a rectangular shape, and is 0.6 mm wide (in x direction) and 10 mm long (in z direction). Therefore, the transducers are long enough (i.e., 10 mm $\gg$ 0.6 mm) to be considered as long linear sources which produce cylindrical sound waves. The distance between the center of any two adjacent transducers (element pitch) is 0.6 mm which provides an active aperture of 38.4 mm. The material under test is a steel block with five drilled-sided-holes. The test sample is a homogeneous medium with a width of 160 mm (in x direction) and a height of 36 mm (in y direction), and a length of 20 mm (in z direction). The holes are drilled all the way through the length of the test sample (in z direction). We assume that the holes are

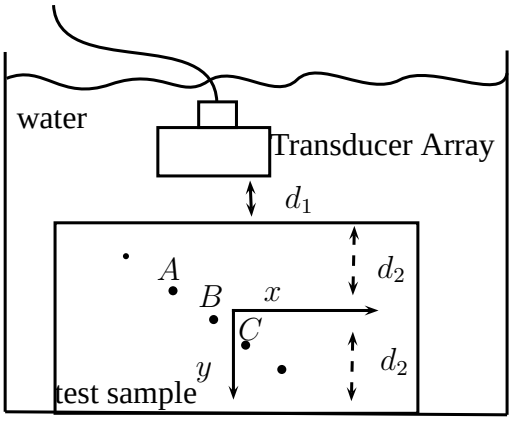

Figure 5.2: Test configuration.

long linear secondary sources which produce backscattered cylindrical sound waves. The holes are considered as defects to be localized using ultrasonic immersion test. The velocity of the longitudinal sound wave inside the test sample was measured to be approximately 6300 m/s. Also, the velocity of the sound wave in water is assumed to be 1480 m/s. The ultrasonic transducer array consists of $M = 64$ elements.

The ultrasonic transducers produce longitudinal sound wave, and we have ignored the production of shear wave in the mode conversion phenomenon. Each transducer fires a probing sound wave toward the test sample through the water, and other transducers receive the backscattered sound wave from the test sample. There is enough time delay between the firing of each transducer to avoid any undesired interference between firing subsequence transducers. The 4096 time-domain received signals are sampled with appropriate sampling frequency and stored in a $64 \times 64 \times 5000$ tensor for post-processing. The sampling frequency is $F_s = 100$ MHz and number of samples N is 5000. A typical time-domain sample of a received signal is shown in Fig. 5.3. To avoid multi-path interferences signals, we process only the first 2400 samples of all

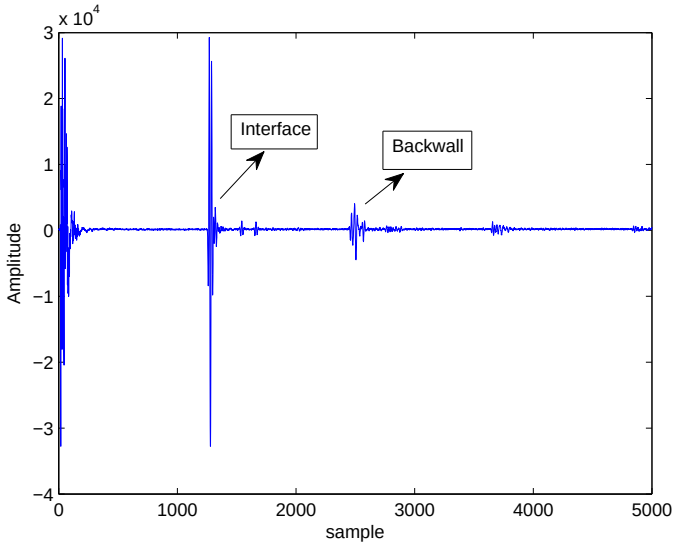

Figure 5.3: A typical time-domain sample of a received signal.

the received signals. Also, the first 1400 samples corresponding to the propagation of the sound wave in the first layer are replaced with zero, as depicted in Fig. 5.4. The probing signal is a wide-band signal with a center frequency of 5 MHz. The Fourier transform of the sample signal is depicted in Fig. 5.5. To suppress the noise, the high frequency components are replaced with zero, as depicted in Fig. 5.6. In the other words, we filter the signal using a low pass filter. In Fig. 5.7(a), we have shown the image of the material under test using our proposed imaging algorithm. The three-dimensional version of this image is shown in Fig. 5.7(c). The ROI is the area between the lines $x = -40$ mm, and $x = 40$ mm, and $y = -18$ mm, $y = 18$ mm corresponding to the steel test sample according to the coordinate system in Fig 5.2. All the images have been normalized to their maximum values (brightest pixel in the image). The three prominent peaks belong to Holes A, B, and C which are shown in Fig 5.2.

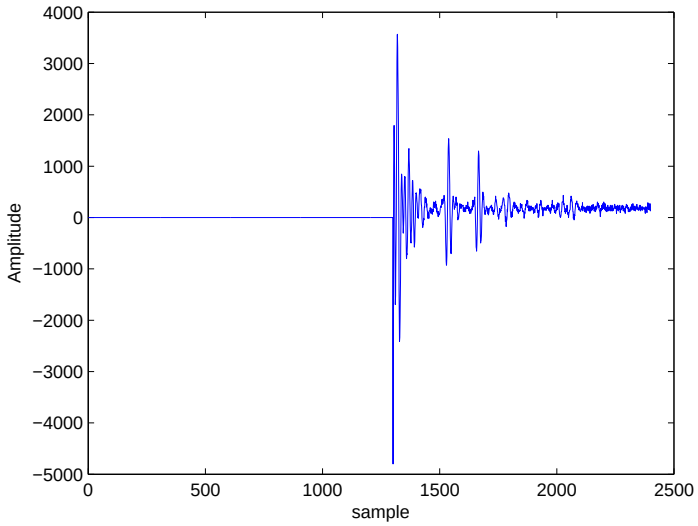

Figure 5.4: Time-gated sample signal used for the proposed algorithm.

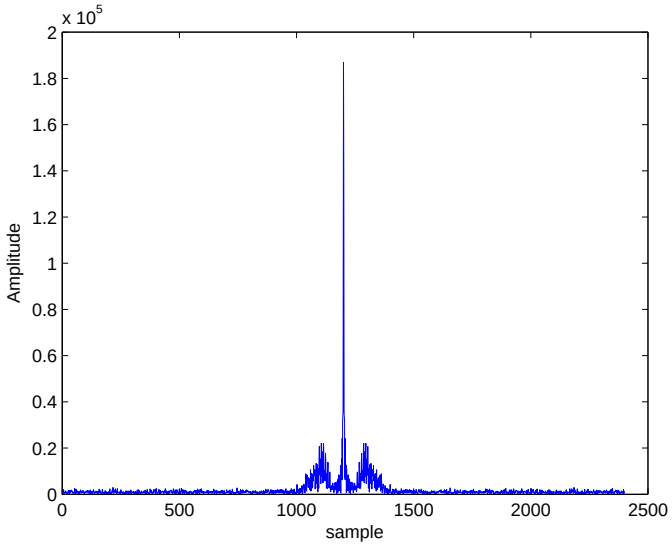

Figure 5.5: Fourier representation of the time-gated sample signal.

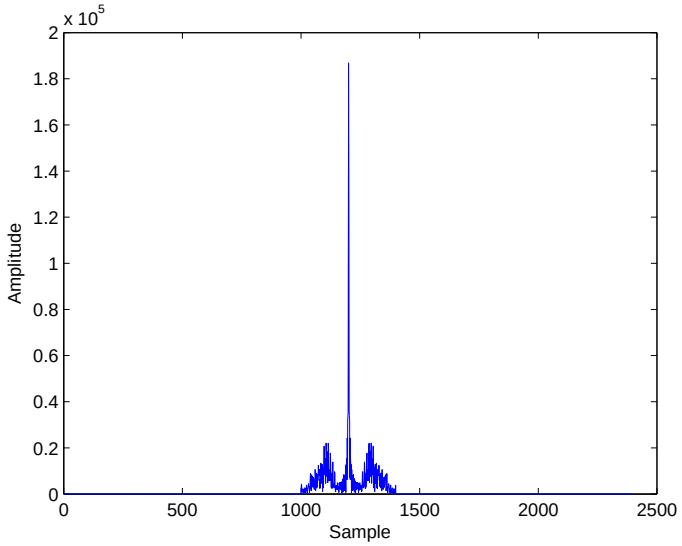

Figure 5.6: High-frequency-filtered sample signal.

We also image the steel block (the second layer of the two-layer medium of water and steel) using the single-layer wavenumber algorithm of [20]. To do so, we have chosen the part of signal corresponding to the propagation of the sound in the steel block using time gating. To this end, the time samples between 1400 and 2400 have been chosen. The sample time-gated signal is depicted in Fig. 5.8. Using the single layer wavenumber algorithm of [20], in Fig. 5.7(b), we have shown the image of the steel test sample. The three-dimensional version of this image is shown in Fig. 5.7(d). The peaks in Fig. 5.7(a) and Fig. 5.7(c) based on our proposed algorithms are more prominent in comparison to peaks in Fig. 5.7(b) and Fig. 5.7(d) based on single-layer wavenumber algorithm using time-gating. To better compare these two approaches, we have shown the images of Holes A, B, and C in Fig. 5.9 which clearly show that our proposed algorithm outperforms the single-layer wavenumber algorithm.

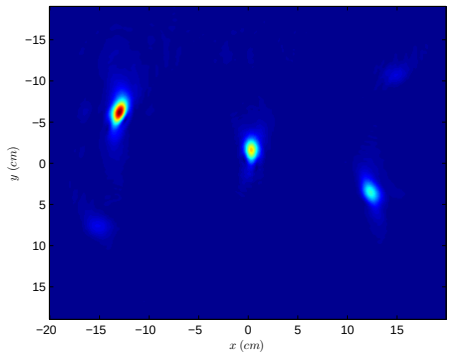

(a) Image of the ROI based on the proposed algorithm.

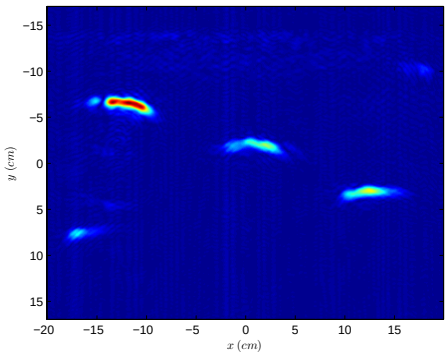

(b) Image of the ROI based on the single-layer wavenumber algorithm.

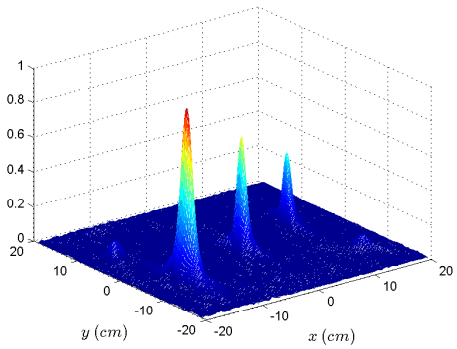

(c) Three-dimensional plot based on the proposed algorithm.

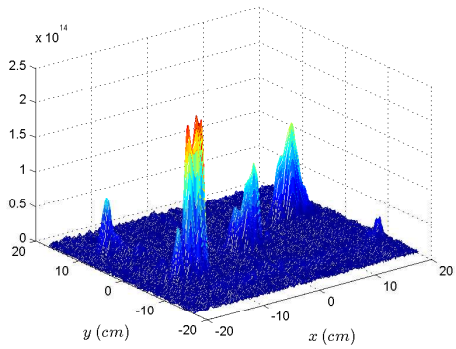

(d) Three-dimensional plot based on the single-layer wavenumber algorithm.

Figure 5.7: A comparison between our proposed algorithm and the single-layer wavenumber algorithm.

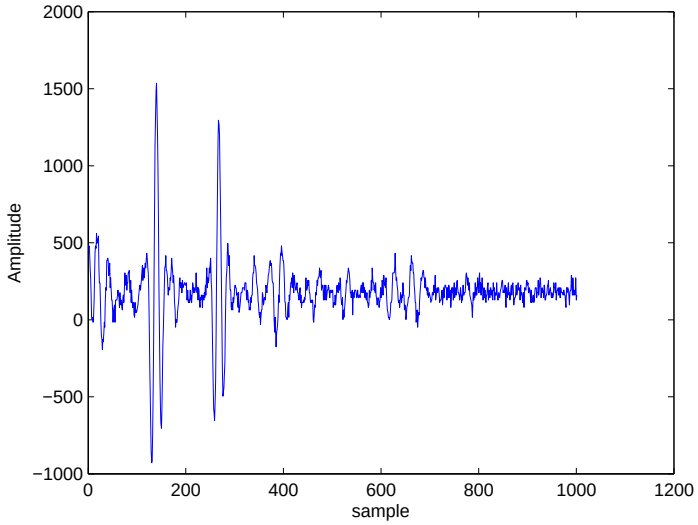

Figure 5.8: Sample signal used in the single-layer wavenumber algorithm.

The performance of the proposed algorithm in terms of the cut-off frequency in the low-passe filter (or equivalently the number frequency bins chosen from the Fourier representation of the signal) is investigated in Fig 5.10. We can see from these images that as we increase the number of frequency bins or the cut-off frequency, the peaks are more prominent.

To compare our proposed mothod with the one using the single-layer wavenumber algorithm in terms of root mean squared error (RMSE), we provide the RMSE plot versus the SNR. To do so, we have added a zero-mean Gaussian noise with different powers, corresponding to different values of SNR, to the raw data. Note that here the SNR is defined as the power of the additive noise to the power of the backscattered signal at the receiving transducers. We reconstruct the image using the data contaminated with additive noise and calculate the RMSE of the location of the peaks. The RMSE is calculated based on the assumption that the true location of the peak

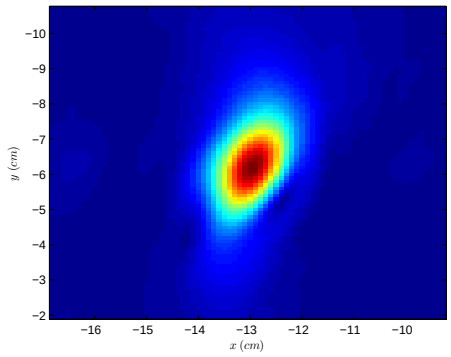

(a) Image of hole A based on the proposed algorithm.

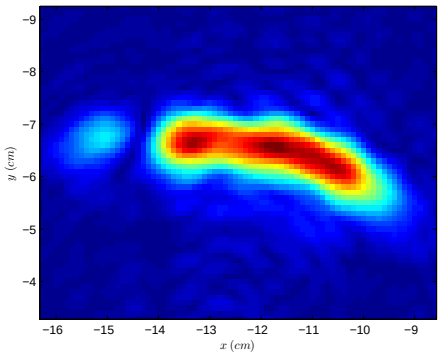

(b) Image of hole A based on the single-layer wavenumber algorithm.

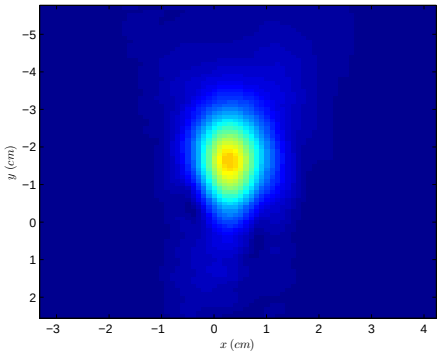

(c) Image of hole B based on the proposed algorithm.

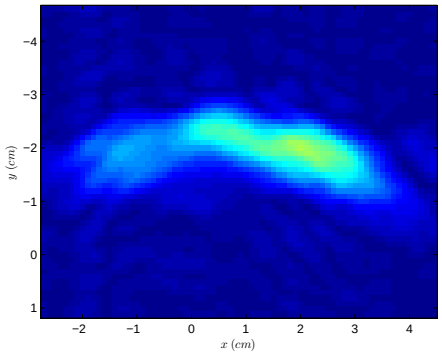

(d) Image of hole B based on the single-layer wavenumber algorithm.

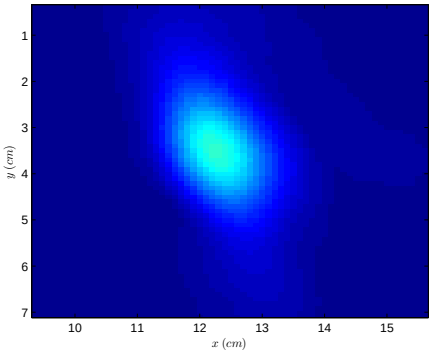

(e) Image of hole C based on the proposed algorithm.

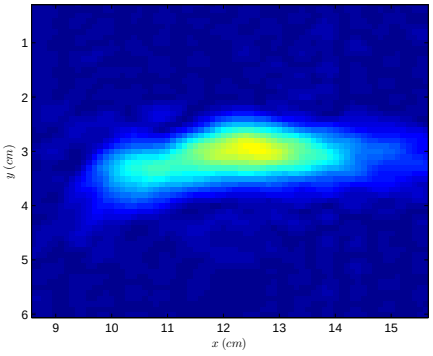

(f) Image of hole C based on the single-layer wavenumber algorithm.

Figure 5.9: Images of the Holes A, B, and C using our proposed algorithm and for the single-layer wavenumber algorithm.

in the image is the one which is obtained from the original data (without additive noise). Fig. 5.11 shows the RMSEs for the holes location estimate obtained using the proposed method and that obtained using the single-layer wavenumber algorithm of [20]. This figure clearly shows the superiority of the proposed method compared to the single-layer wavenumber algorithm.

We also compare the performance of the Fourier-based algorithm proposed in this chapter with the performance of the algorithms of Chapter 4 when they use our new array spatial signature. Fig. 5.12 shows the RMSEs for the holes location estimates obtained using the proposed algorithm in this chapter and those obtained by using our proposed array spatial signature in the different imaging algorithms including the conventional beamforming technique of (4.2.1), the MUSIC method of (4.2.4), and the Capon algorithm of (4.2.2). This figure shows that the RMSE of the conventional beamforming technique and the MUSIC method is better than the Fourier-based algorithm. The Capon algorithm also performs better in the low SNR regions. However, the execution time for the Fourier-based algorithm is the superiority of the proposed method compared to the algorithms of Chapter 4. For the algorithms of Chapter 4, we need to calculate two integration over the upper surface of the test sample for each point in the ROI. Also, note that for the conventional beamforming technique of (4.2.1), the MUSIC algorithm of (4.2.4), and the Capon method of (4.2.2), we need to calculate the scattering coefficient of each point in the ROI, and we have to repeat that for each frequency bin. However, in the Fourier-based algorithm, we do the Stolt mapping of (5.3.4). This mapping is computationally simple, thus justifying the low computational complexity of the Fourier-based algorithm.

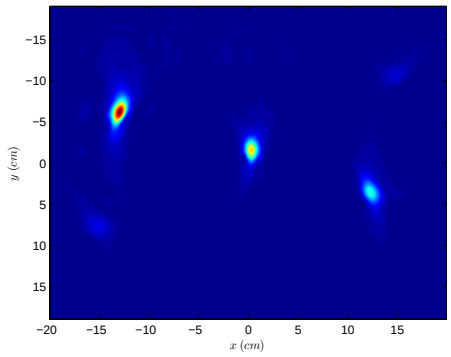

(a) Image of the ROI using 1320 frequency bins.

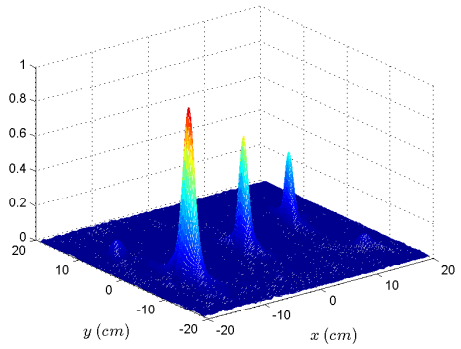

(b) Three-dimensional image of ROI using 1320 frequency bins.

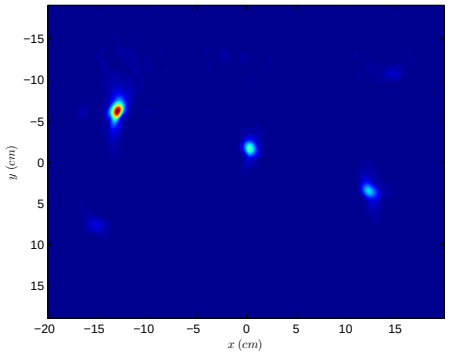

(c) Image of the ROI using 1350 frequency bins.

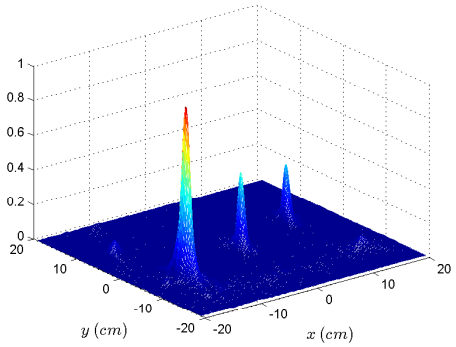

(d) Three-dimensional image of ROI using 1350 frequency bins.

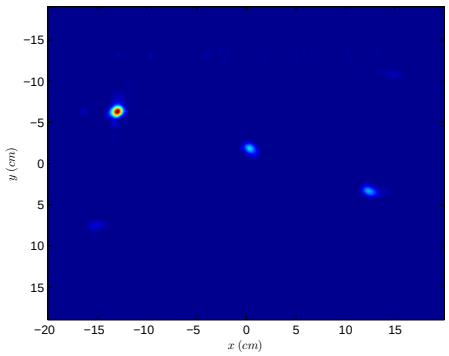

(e) Image of the ROI using 1400 frequency bins.

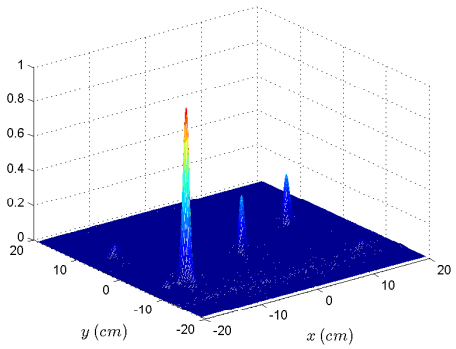

(f) Three-dimensional image of ROI using 1400 frequency bins.

Figure 5.10: Image of the ROI using our proposed algorithm for different number of frequency bins.

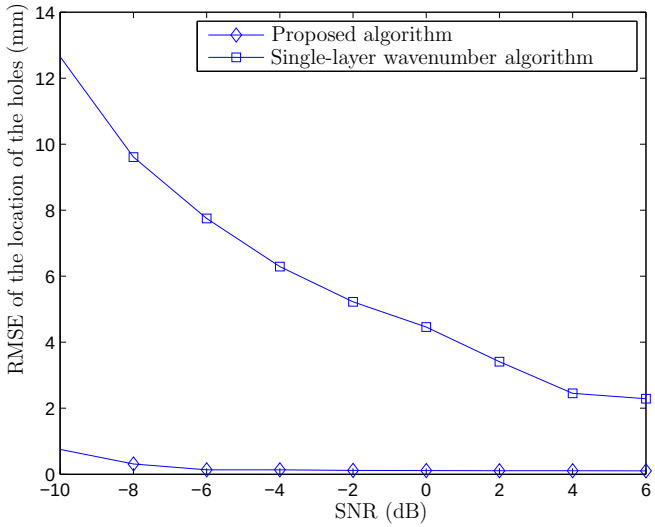

Figure 5.11: The RMSE curve versus SNR for the proposed algorithm and that for the single-layer wavenumber algorithm.

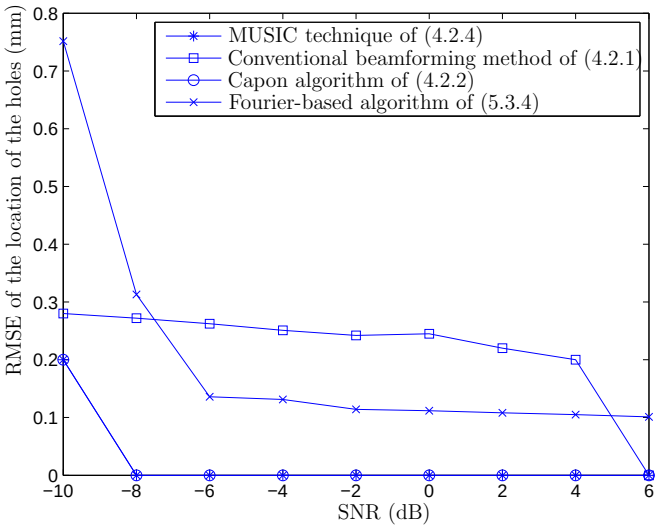

Figure 5.12: The RMSE curves versus SNR for the proposed algorithm and for the algorithms of Chapter 4.

5.5 Conclusions

In this chapter, we used an approximation of the proposed data model for backscattered received signal. Then, we proposed a Fourier-based imaging algorithm for the second layer of the material under test. In this algorithm, the execution time is considerably reduced compared to the aforementioned three algorithms in the previous chapter and it can be used in an online imaging process.

Chapter 6

Conclusions and Future Work

6.1 Conclusions

In this dissertation, we considered the problem of multi-layer ultrasonic imaging using an array of ultrasonic transducers. Ultrasonic imaging for a multi-layer medium is a common challenge in seismology, medical diagnoses, and non-destructive testing (NDT). One of the applications of multi-layer imaging is ultrasonic immersion test where the material under test and the transducer array are immersed in water. The main imaging challenge in immersion test (or any multi-layer medium) is that since the sound wave propagates with different speeds in different layers of a multi-layer medium, such a medium cannot be assumed homogenous. As a result, calculating the sound travel time for the received signal due to backscattering from such a non-homogenous medium is not as straightforward as in the case of homogenous materials. To tackle this problem, first we modeled the interfaces between the layers of a multi-layer medium as spatially distributed sources. Based on this model, we established three different approaches.

In the first approach, we considered the problem of immersion ultrasonic test. In such

a test scenario, the upper surface of the test sample has two effects, i) it produces a strong interference signal in the backscattered received signal, and ii) its shape determines the array spatial signature of every point inside the material under test, thereby causing difficulties in the flaw detection and imaging. Hence, in immersion NDT, the knowledge of the shape of the upper surface of the test sample is required to achieve a precise localization of a crack inside the test sample. In this approach, we proposed a distributed reflector modeling approach to characterize the interface between water and a solid test sample as well as any crack inside the solid test sample. This approach relies on the so-called incoherently distributed reflector modeling, where a distributed reflector can be modeled as infinitely many point sources located close to each other. Using such a modeling, we developed a covariance fitting based approach to estimate the parameters of the shape of the interface between the two media and those of the shape of a crack inside the test material. Our numerical experiments show that our proposed approach yields a lower root mean squared error for the parameter estimates, compared to a state-of-the-art method, called root mean squared velocity technique. However the proposed approach is a parametric localization method which needs the repetition of the ultrasonic test.

In the second approach we present a new model for the array spatial signature which is applicable for frequency-domain algorithms for imaging a two-layer medium when there is no need to repeat the ultrasonic test. To do so, we modeled the interface between the two layers as a spatially distributed source which consists of an infinite number of point sources. Then, based on Huygens principle, we developed a new array spatial signature for any point inside the second layer of a two-layer medium. This new array spatial signature can be used for multi-layer ultrasonic imaging in

frequency-domain imaging techniques including the conventional beamforming technique, the MUSIC method, and the Capon algorithm which are traditionally proposed for a homogeneous medium where the sound velocity is constant in the material under test. Numerical simulations as well as experimental data show the accuracy of the proposed model.

In the third approach, to reduce the execution time of the imaging process, we developed a Fourier-based imaging algorithm to estimate the scattering coefficient of all the points inside the second layer of a two-layer medium in order to obtain an image of the ROI. First, we use an approximation of the proposed data model for the array backscattered signals due to the scattering of the point scatterers inside the second layer of the material under test. Seeking the similarity with the definition of Fourier transform, we propose a Fourier-based imaging algorithm, for imaging the second layer of the material under test. In this proposed algorithm, the execution time is considerably reduced compared to the three aforementioned algorithm and it can be used in an online imaging process.

6.2 Future Work

There are two interesting topics to consider as possible future work.

- Application of the Weyl decomposition for multi-layer imaging is one possible topic which can be investigated. In most literature, sound waves are assumed to be plane waves at the interface between the layers of a multi-layer medium. However in many applications of ultrasonic testing, the sensors are located at a finite distance from the targets. Therefore, one has to consider the problem of

spherical or cylindrical wave reflection and refraction. To tackle the problem of wave refraction at the interface between two layers with two different velocities, one approach is to use Weyl decomposition [45]. The main idea in Weyl approach is to represent the spherical wave as a superposition of plane waves whose reflection and refraction at the interface between the two can be explained by Snell's law. This decomposition is done by using the spatial Fourier transform. Also, each of the plane waves, in the Weyl integral, is required to be multiplied by the transmission coefficient when traveling from one layer to another. based on this approach, one can obtain a new model for array spatial signature and use that in different imaging algorithms.

- Another interesting topic is to modify the wavenumber algorithm for imaging a cylindrical pipe structure under immersion ultrasonic test. Pipeline imaging has many applications in industry including inspection of water pipelines, gas pipelines, and power plants [23]. Traditionally, radiography has been used for pipeline imaging by putting a film in placed inside the pipe. Since the inner side of the pipe is not accessible in many applications, the radiography is not implementable and the ultrasonic imaging technique is used lieu of radiography. Due to uneven surface of pipes, immersion test is preferred for pipe inspection. Therefore multi-layer imaging techniques are needed for imaging a pipe under immersion test. Wavenumber algorithm is an efficient approach in terms of execution time, however, this method has restrictions in terms of the geometry of the material under test and the test setup. These assumptions are tied with the definition of Fourier transform. Therefore, to extend the proposed algorithm for ultrasonic pipe imaging, we need to modify the presented data model.

Appendix A

Derivations

A.1 Deriving (3.1.13) and (3.1.16)

Here, we show the derivation of the covariance matrix of $\mathbf{p}^{(i)}(\omega)$, i.e., $\mathbf{R}(\omega)$ as shown in (3.1.13). To do so, we can write

$$\begin{aligned}
&\mathbf{R}(\omega) = E\{\mathbf{p}^{(i)}(\omega)(\mathbf{p}^{(i)}(\omega))^H\} = \\
&E\left\{\left(\int\limits_{y=C(x)} \phi(\omega)\ \mathbf{v}(\omega;x,y)\ s_i(x,y)\ dx + \boldsymbol{\nu}^{(i)}(\omega)\right)\right. \\
&\left.\left(\int\limits_{y=C(x)} \phi(\omega)\ \mathbf{v}(\omega;x,y)\ s_i(x,y)\ dx + \boldsymbol{\nu}^{(i)}(\omega)\right)^H\right\}. \qquad \text{(A.1.1)}
\end{aligned}$$

We can now expand (A.1.1) as

$$\begin{aligned}\mathbf{R}(\omega) = &\iint\limits_{\substack{y=C(x)\\y'=C(x')}} |\phi(\omega)|^2 \mathbf{v}(\omega;x,y)\ \mathbf{v}^H(\omega;x',y')\ E(s_i(x,y)\ s_i^*(x',y'))\ dx\ dx' \\ &+\iint\limits_{\substack{y=C(x)\\y'=C(x')}} |\phi(\omega)|^2 \mathbf{v}(\omega;x,y)\ \mathbf{v}^H(\omega;x',y')\ E(s_i(x,y)\ \boldsymbol{\nu}^{(i),H}(\omega))\ dx\ dx' \\ &+\iint\limits_{\substack{y=C(x)\\y'=C(x')}} |\phi(\omega)|^2 \mathbf{v}(\omega;x,y)\ \mathbf{v}^H(\omega;x',y')\ E(\boldsymbol{\nu}_i(\omega)\ s_i^*(x',y'))\ dx\ dx' \\ &+E(\boldsymbol{\nu}_i(\omega)\ \boldsymbol{\nu}^{(i),H}(\omega)) \end{aligned} \tag{A.1.2}$$

Using the assumption that the noise and the reflection coefficients of the reflector points are independent and that the noise is zero-mean, i.e.,

$$E(s_i(x,y)\ \boldsymbol{\nu}^{(i),H}(\omega)) = \mathbf{0} \tag{A.1.3}$$

$$E(\boldsymbol{\nu}^{(i)}(\omega)\ s_i^*(x',y')) = \mathbf{0}, \tag{A.1.4}$$

we can write (A.1.2) as

$$\mathbf{R}(\omega) = \iint\limits_{\substack{y=C(x)\\y'=C(x')}} \phi(\omega)\phi^*(\omega)\mathbf{v}(\omega;x,y)\ \mathbf{v}^H(\omega;x',y')\ \varrho(x,y,x',y')\ dx\ dx' + \sigma_\nu^2\mathbf{I} \tag{A.1.5}$$

where σ_ν^2 is the variance of the received noise and

$$\varrho(x,y,x',y') \triangleq E(s_i(x,y)\ s_i^*(x',y')). \tag{A.1.6}$$

As we model the upper surface as an ID reflector, signals arriving from different points of this surface are uncorrelated. Therefore, we can write

$$\varrho(x,y,x',y') = \rho(x,y)\ \delta(x-x')\ \delta(y-y') \tag{A.1.7}$$

where $\rho(x,y)$ is the reflection density of a point reflector located at (x,y) on the upper surface and it is defined only for the surface $y = C(x)$. Using (A.1.7), the covariance matrix $\mathbf{R}(\omega)$ in (3.1.13) can be expressed as

$$\mathbf{R}(\omega) = \int\limits_{y=C(x)} \mathbf{V}(\omega; x, y)\ \rho(x,y)\ dx + \sigma_\nu^2 \mathbf{I} \tag{A.1.8}$$

where

$$\mathbf{V}(\omega; x, y) \triangleq\ |\phi(\omega)|^2\ \mathbf{v}(\omega; x, y)\ \mathbf{v}^H(\omega; x, y). \tag{A.1.9}$$

A.2 Deriving (3.2.10)

The covariance matrix of $\tilde{\mathbf{p}}^{(i)}(\omega)$ can be written as

$$\tilde{\mathbf{R}}(\omega) = E\{\tilde{\mathbf{p}}^{(i)}(\omega)(\tilde{\mathbf{p}}^{(i)}(\omega))^H\} =$$

$$E\left\{\left(\boldsymbol{\nu}^{(i)}(\omega) + \iiint\limits_{\substack{y_1=C(x_1)\\ y_2=C(x_2)\\ y_3=C(x_3)}} \phi(\omega)\mathbf{u}(\omega; x_1, y_1, x_2, y_2, x_3, y_3)\gamma_i(x_1, y_1, x_2, y_2, x_3, y_3)dx_1dx_2dx_3\right)\right.$$

$$\left.\left(\boldsymbol{\nu}^{(i)}(\omega) + \iiint\limits_{\substack{y_1=C(x_1)\\ y_2=C(x_2)\\ y_3=C(x_3)}} \phi(\omega)\mathbf{u}(\omega; x_1, y_1, x_2, y_2, x_3, y_3)\gamma_i(x_1, y_1, x_2, y_2, x_3, y_3)dx_1dx_2dx_3\right)^H\right\}. \tag{A.2.1}$$

We can expand (A.2.1) as

$$\tilde{\mathbf{R}}(\omega) =$$

$$\iiint\limits_{\substack{y_1=C(x_1)\\ y_2=C(x_2)\\ y_3=C(x_3)}} \iiint\limits_{\substack{y_1'=C(x_1')\\ y_2'=C(x_2')\\ y_3'=C(x_3')}} |\phi(\omega)|^2 \mathbf{u}(\omega; x_1, y_1, x_2, y_2, x_3, y_3)\mathbf{u}^H(\omega; x_1', y_1', x_2', y_2', x_3', y_3')$$

$$E(\gamma_i(x_1, y_1, x_2, y_2, x_3, y_3)\boldsymbol{\nu}^{(i),H}(\omega))dx_1'dx_2'dx_3'dx_1dx_2dx_3$$

$$+ \iiint\limits_{\substack{y_1=C(x_1)\\ y_2=C(x_2)\\ y_3=C(x_3)}} \iiint\limits_{\substack{y_1'=C(x_1')\\ y_2'=C(x_2')\\ y_3'=C(x_3')}} |\phi(\omega)|^2 \mathbf{u}(\omega; x_1, y_1, x_2, y_2, x_3, y_3)\mathbf{u}^H(\omega; x_1', y_1', x_2', y_2', x_3', y_3')$$

$$E(\boldsymbol{\nu}^{(i)}(\omega)\gamma_i^*(x_1, y_1, x_2, y_2, x_3, y_3))dx_1'dx_2'dx_3'dx_1dx_2dx_3$$

$$+ \iiint\limits_{\substack{y_1=C(x_1)\\ y_2=C(x_2)\\ y_3=C(x_3)}} \iiint\limits_{\substack{y_1'=C(x_1')\\ y_2'=C(x_2')\\ y_3'=C(x_3')}} |\phi(\omega)|^2 \mathbf{u}(\omega; x_1, y_1, x_2, y_2, x_3, y_3)\mathbf{u}^H(\omega; x_1', y_1', x_2', y_2', x_3', y_3')$$

$$E(\gamma_i(x_1, y_1, x_2, y_2, x_3, y_3)\gamma_i^*(x_1, y_1, x_2, y_2, x_3, y_3))dx_1'dx_2'dx_3'dx_1dx_2dx_3$$

$$+ E(\boldsymbol{\nu}^{(i)}(\omega)\ \boldsymbol{\nu}^{(i),H}(\omega)). \tag{A.2.2}$$

Using the assumption that the noise and the reflection/refraction coefficients of the reflecting/refracting points are statistically independent, we can use

$$E(\gamma_i(x_1, y_1, x_2, y_2, x_3, y_3)\boldsymbol{\nu}^{(i),H}(\omega)) = \mathbf{0} \tag{A.2.3}$$

$$E(\boldsymbol{\nu}^{(i)}(\omega)\gamma_i^*(x_1, y_1, x_2, y_2, x_3, y_3)) = \mathbf{0}, \tag{A.2.4}$$

to write (A.2.2) as

$$\tilde{\mathbf{R}}(\omega) = E\{\tilde{\mathbf{p}}^{(i)}(\omega)(\tilde{\mathbf{p}}^{(i)}(\omega))^H\} = \sigma^2\mathbf{I} + \tag{A.2.5}$$

$$\iiint\limits_{\substack{y_1=C(x_1)\\ y_2=C(x_2)\\ y_3=C(x_3)}} \iiint\limits_{\substack{y_1'=C(x_1')\\ y_2'=C(x_2')\\ y_3'=C(x_3')}} |\phi(\omega)|^2 \mathbf{u}(\omega; x_1, y_1, x_2, y_2, x_3, y_3)\mathbf{u}^H(\omega; x_1', y_1', x_2', y_2', x_3', y_3')$$

$$E(\gamma_i(x_1, y_1, x_2, y_2, x_3, y_3)\gamma_i^*(x_1, y_1, x_2, y_2, x_3, y_3))dx_1'dx_2'dx_3'dx_1dx_2dx_3.$$

Bibliography

[1] L. Godara, "Applications of antenna arrays to mobile communications. I. performance improvement, feasibility, and system considerations," *Proc. IEEE.*, vol. 85, pp. 1031–1060, Jul 1997.

[2] L. Godara, "Application of antenna arrays to mobile communications. II. beamforming and direction-of-arrival considerations," *Proc. IEEE.*, vol. 85, pp. 1195–1245, Aug. 1997.

[3] J. Li and P. Stoica, *Robust Adaptive Beamforming*. New Jersey: John Wiley and Sons, 2006.

[4] S. Shahbazpanahi, A. Gershman, Z.-Q. Luo, and K. M. Wong, "Robust adaptive beamforming for general-rank signal models," *IEEE Trans. Signal Process.*, vol. 51, pp. 2257–2269, Sep. 2003.

[5] S. Valaee, B. Champagne, and P. Kabal, "Parametric localization of distributed sources," *IEEE Trans. Signal Process.*, vol. 43, pp. 2144–2153, Sep. 1995.

[6] S. ShahbazPanahi, S. Valaee, and M. Bastani, "Distributed source localization using ESPRIT algorithm," *IEEE Trans. Signal Process.*, vol. 49, pp. 2169–2178, Oct. 2001.

[7] S. ShahbazPanahi, S. Valaee, and A. Gershman, "A covariance fitting approach to parametric localization of multiple incoherently distributed sources," *IEEE Trans. Signal Process.*, vol. 52, pp. 592–600, Mar. 2004.

[8] J. Li and P. Stoica, *MIMO Radar Signal Processing.* New Jersey: Wiley-IEEE Press, Oct 2008.

[9] P. Naidu, *Sensor Array Signal Processing.* Boca Raton: Taylor and Francis Group, Oct 2009.

[10] A. Nehorai, K.-C. Ho., and B. T. G. Tan, "Minimum-noise-variance beamformer with an electromagnetic vector sensor," *IEEE Trans. Signal Process.*, vol. 47, pp. 601–618, March 1999.

[11] K.-C. Ho, T. Tan, and A. Nehorai, "Estimating directions of arrival of completely and incompletely polarized signals with electromagnetic vector sensors," *IEEE Trans. Signal Process.*, vol. 47, pp. 2845–2852, Oct 1999.

[12] C. Ko, J. Zhang, and A. Nehorai, "Separation and tracking of multiple broadband sources with one electromagnetic vector sensor," *IEEE Trans. Aerospace and Electronic Systems.*, vol. 38, pp. 1109–1116, march 2002.

[13] S. Valaee and P. Kabal, "Wideband array processing using a two-sided correlation transformation," *IEEE Trans. Signal Process.*, vol. 43, pp. 160–172, Jan 1995.

[14] H. Wang and M. Kaveh, "Coherent signal-subspace processing for the detection and estimation of angles of arrival of multiple wide-band sources," *IEEE Trans. Acoustics, Speech and Signal Process.*, vol. 33, pp. 823–831, April 1985.

[15] J. F. Yang and M. Kaveh, "Coherent signal-subspace transformation beam former," *i IEE Proc. Radar and Signal Process.*, vol. 137, pp. 267–275, April 1990.

[16] M. Sullivan, *Practical Array Processing.* New York: McGraw-Hill, 2009.

[17] B. W. Drinkwater and P. D. Wilcox, "Ultrasonic arrays for non-destructive evaluation: A review," *Nondestr. Test Eval. Int.*, vol. 39, pp. 525 – 541, Oct. 2006.

[18] C. Holmes, B. W. Drinkwater, and P. D. Wilcox, "Post-processing of the full matrix of ultrasonic transmitreceive array data for non-destructive evaluation," *Nondestr. Test Eval. Int.*, vol. 38, pp. 701 – 711, Dec. 2005.

[19] P. Wilcox, C. Holmes, and B. Drinkwater, "Advanced reflector characterization with ultrasonic phased arrays in NDE applications," *IEEE Trans. Ultrasonics, Ferroelectrics., and Freq. Contr.*, vol. 54, pp. 1541–1550, Aug. 2007.

[20] A. Hunter, B. Drinkwater, and P. Wilcox, "The wavenumber algorithm for full-matrix imaging using an ultrasonic array," *IEEE Trans. Ultrasonics, Ferroelectrics., and Freq. Contr.*, vol. 55, pp. 2450–2462, Nov. 2008.

[21] F. Lingvall and T. Olofsson, "On time-domain model-based ultrasonic array imaging," *IEEE Trans. Ultrasonics, Ferroelectrics., and Freq. Contr.*, vol. 54, pp. 1623–1633, Aug 2007.

[22] T. Stepinski, "An implementation of synthetic aperture focusing technique in frequency domain," *IEEE Trans. Ultrasonics, Ferroelectrics., and Freq. Contr.*, vol. 54, pp. 1399–1408, Jul. 2007.

[23] M. Skjelvareid, Y. Birkelund, and Y. Larsen, "Synthetic aperture focusing of outwardly directed cylindrical ultrasound scans," *IEEE Trans. Ultrasonics, Ferroelectrics., and Freq. Contr.*, vol. 59, pp. 2460–2469, Nov. 2012.

[24] M. Skjelvareid, T. Birkelund, and Y. Larsen, "Internal pipeline inspection using virtual source synthetic aperture ultrasound imaging," *Nondestr. Test Eval. Int.*, vol. 54, pp. 151 – 158, Mar. 2013.

[25] T. Olofsson, "Phase shift migration for imaging layered objects and objects immersed in water," *IEEE Trans. Ultrasonics, Ferroelectrics., and Freq. Contr.*, vol. 57, pp. 2522–2530, Nov. 2010.

[26] M. Skjelvareid, T. Olofsson, Y. Birkelund, and Y. Larsen, "Synthetic aperture focusing of ultrasonic data from multilayered media using an omega-k algorithm," *IEEE Trans. Ultrasonics, Ferroelectrics., and Freq. Contr.*, vol. 58, pp. 1037–1048, May. 2011.

[27] R. Schmidt, "Multiple emitter location and signal parameter estimation," *IEEE Trans. Antennas and Propagation.*, vol. 34, pp. 276–280, 1986.

[28] P. Stoica, Z. Wang, and J. Li, "Robust capon beamforming," *IEEE. Signal Process. Lett.*, vol. 10, pp. 172–175, Jun. 2003.

[29] D. H. Johnson and D. E. Dugeon, *Array Signal Processing: Concepts and Techniques.* Prentice Hall, 1993.

[30] F. Foroozan and S. Shahbazpanahi, "Music-based array imaging in multi-modal ultrasonic non-destructive testing," in *Sensor Array and Multichannel Signal Process. Workshop. Hoboken. NJ.*, pp. 529–532, Jun. 2012.

[31] S. Doctor, T. Hall, and L. Reid, "Saft the evolution of a signal processing technology for ultrasonic testing," *Nondestr. Test Eval. Int.*, vol. 19, pp. 163 – 167, Jun. 1986.

[32] W. Schneider, "The common depth point stack," *Proc. IEEE*, vol. 72, pp. 1238–1254, Oct. 1984.

[33] P. Schultz, "Seismic velocity estimation," *Proc. IEEE*, vol. 72, pp. 1330–1339, Oct. 1984.

[34] M. Haun, D. Jones, and W. O'Brien, "Adaptive focusing through layered media using the geophysical time migration concept," in *IEEE Proc. Ultrasonics Symp. Munich, Germany.*, pp. 1635–1638 vol.2, Feb 2002.

[35] M. Skjelvareid and Y. Birkelund, "Ultrasound imaging using multilayer synthethic aperture focusing," *in proc. ASME. Bellevue. Washington.*, pp. 1–9, Jul. 2010.

[36] J. Gazdag and P. Sguazzero, "Migration of seismic data by phase shift plus interpolation," *Geophysics*, vol. 49, pp. 124–131, Feb. 1984.

[37] T.-P. Jantti, "The influence of extended sources on the theoretical performance of the MUSIC and ESPRIT methods: narrow-band sources," in *IEEE Int. Conf. Acoust. Speech. Signal Process.*, vol. 2, pp. 429–432, Mar. 1992.

[38] Y. Meng, P. Stoica, and K. Wong, "Estimation of the directions of arrival of spatially dispersed signals in array processing," *IEEE Proc. Radar. Sonar. Navigation.*, vol. 143, pp. 1–9, Feb. 1996.

[39] A. Hassanien, S. ShahbazPanahi, and A. Gershman, "A generalized Capon estimator for localization of multiple spread sources," *IEEE Trans. Signal Process.*, vol. 52, Jan. 2004.

[40] M. Bengtsson and B. Ottersten, "Low-complexity estimators for distributed sources," *IEEE Trans. Signal Process.*, vol. 48, pp. 2185–2194, Aug. 2000.

[41] Y. Wang and A. Zoubir, "Some new techniques of localization of spatially distributed sources," in *Asilomar Conf. Signals Systems Computers.*, pp. 1807–1811, Nov. 2007.

[42] Q. Li and H. Chen, "A lower dimensional MLE algorithm for distributed source parameter estimation," in *Int. Congr. Image Signal Process.*, pp. 1–4, Oct. 2009.

[43] T. Gehrke, F. Cheikhrouhou, and H. Overhoff, "Derivation of the impulse response of ultrasonic transducers by experimental system identification," in *IEEE Int. Ultrasonics Symp., Rotterdam*, vol. 1, pp. 349–352, Sep. 2005.

[44] A. Coppe, R. Haftka, N.-H. Kim, and C. Bes, "A statistical model for estimating probability of crack detection," in *International Conference on Prognostics and Health Management,*, pp. 1–5, 2008.

[45] L. M. Brekhovskikh and O. A. Godin, *Acoustics of layered media II.* Springer, 1959.

[46] J. W. Goodman, *Introduction to Fourier Optics.* McGraw-Hill, 1996.

[47] D. H. Johnson and D. E. Dugeon, *Sensor Array Signal Processing.* CRC Press, 2000.

[48] N. Moallemi and S. ShahbazPanahi, "A distributed reflector localization approach to ultrasonic array imaging for non-destructive testing application," *IEEE Trans. Signal Process.*, vol. 62, pp. 3863–3873, Aug. 2014.

[49] J. W. Goodman, *Introduction to Fourier Optics.* McGraw-Hill, 1996.